Domain Motions and Complex Formation in Catalysis by NADPH-Cytochrome P450 Reductase

Samuel Lewis Freeman MChem

A thesis submitted for the degree of
Doctor of Philosophy

Department of Chemistry
University of Leicester
United Kingdom
2017

Statement

Unless otherwise acknowledged, the experimental work described in this thesis was carried out by the author in the Department of Chemistry at the University of Leicester, UK or the Institut-Laue Langevin, Grenoble, France between September 2014 and September 2017. The work has not been submitted, and is not presently being submitted for any other degree at this or any other university.

Signed:

Date:

Department of Chemistry
University of Leicester
Leicester
LE1 7RH
UK

Domain Motions and Complex Formation in Catalysis by NADPH-Cytochrome P450 Reductase

Samuel Lewis Freeman MChem

Abstract

NADPH-cytochrome P450 reductase (CPR) is a multi-domain diflavin redox enzyme which is a key component of the P450 mono-oxygenase drug-metabolising system. This study was aimed to achieve an understanding of domain motions of human CPR which are believed to be intrinsic to its function and steps in its catalytic cycle. The protein and various mutants were prepared highly pure and catalytically active. Reduction of the oxidised form of the enzyme to its various possible redox states was accomplished using a variety of reducing agents. The redox states were characterised spectroscopically and stopped-flow techniques were used to further characterise the kinetics of the protein and mutants thereof under different conditions. Using small-angle X-ray scattering (SAXS) some evidence had been presented for a conformational equilibrium involving large-scale domain motions in this enzyme. The proposed equilibrium is studied using small-angle neutron scattering (SANS), under conditions where we are able to control the redox state of the enzyme precisely. It is shown that different redox states and buffer conditions have a profound effect on the conformational state of the enzyme and these findings are linked to kinetics studies. Different ways to model the data based on multi-state systems are presented. It is demonstrated that by altering the position of the conformational equilibrium by mutagenesis, the presence of a greater proportion of the extended form leads to an enhanced ability to transfer electrons to cytochrome *c* on the millisecond timescale. The position of the conformational equilibrium can therefore be defined for individual steps in the catalytic cycle. For the first time, the nature of the complex in solution between CPR and an electron transfer partner, cytochrome *c*, is described by means of deuteration and contrast matching in SANS. Finally, a time resolved structural study employing stopped-flow and SAXS measurements was designed and performed in an attempt to interpret the changes that CPR undergoes as a function of time.

Acknowledgements

I gratefully acknowledge my supervisors Profs. Gordon C. K. Roberts and Emma L. Raven at Leicester and Dr. Anne Martel at the ILL. The quality of work presented in this thesis and published elsewhere would not have been possible without their time, careful and thorough advice, and guidance.

In addition, I would like to thank all those who have offered a guiding hand in the laboratory, namely Drs. Hanna Kwon and Jaswir Basran in Leicester and Drs. Juliette Devos and Martin Pedersen at the EPN campus in Grenoble. Without their help I could have never developed the skills and been as productive as I was, being the last bastion of CPR research in Leicester.

Finally, the support of my family and friends made the whole process smooth and thoroughly enjoyable throughout my entire university career. A special thanks to my father for joining me on those long drives back and forth between Leicester and Grenoble, and to my mother for endless encouragement.

Contents

List of Figures

List of Tables

List of Abbreviations

Chemicals and solutions

BES - N,N-Bis(2-hydroxyethyl)-2-aminoethanesulfonic acid

CO - Carbon monoxide

IPTG - Isopropyl β-D-1-thiogalactopyranoside

LB - Lysogeny broth (growth medium)

SDS - Sodium dodecyl sulfate

TB - Terrific broth (growth medium)

Tris - tris(hydroxymethyl)aminomethane

Enzymes and Co-enzymes

CYP/P450 - Cytochrome P450

cspA - Cold-shock protein A

Cyt *c* - Cytochrome *c*

FAD - Flavin adenine dinucleotide

FMN - Flavin mononucleotide

NADP(H) - (Reduced) nicotinamide adenine dinucleotide phosphate

NAD(H) - (Reduced) nicotinamide adenine dinucleotide

Techniques

Cryo-EM - Cryo-electron microscopy

FPLC - Fast protein liquid chromatography

FRET - Förster resonance energy transfer *or* fluorescence resonance energy transfer

MADLDI-TOF - Matrix assisted laser desorption ionisation-time of flight

NMR - Nuclear magnetic resonance

PMF - Peptide mass fingerprinting

SAS - Small-angle scattering

SANS - Small-angle neutron scattering

SAXS - Small-angle X-ray scattering

SDS-PAGE - Sodium dodecyl sulphate polyacrylamide gel electrophoresis

UV-visible - Ultraviolet-visible

WAXS - Wide-angle X-ray scattering

XFEL - X-ray free-electron laser

Amino Acids

G - Glycine -Gly, **P** - Proline -Pro

A - Alanine - Ala, **V** - Valine - Val

L - Leucine - Leu, **I** - Isoleucine - Ile

M - Methionine - Met, **C** - Cysteine - Cys

F - Phenylalanine - Phe, **Y** - Tyrosine - Tyr

W - Tryptophan - Trp, **H** - Histidine - His

K - Lysine - Lys, **R** - Arginine - Arg

Q - Glutamine - Gln, **N** - Asparagine - Asn

E - Glutamic Acid - Glu, **D** - Aspartic Acid - Asp

S - Serine - Ser, **T** - Threonine- Thr

Miscellaneous

A.U. - Absorbance units

DNA - Deoxyribonucleic acid

ET - Electron transfer

O.D. - Optical density

PDB - Protein data bank

PNACL - Protein and Nucleic Acid Chemistry Laboratory (University of Leicester)

RPM - Revolutions per minute

Part I

Introduction

Chapter 1

The Cytochrome P450 Mono-oxygenase System

This chapter introduces the biological background of the cytochrome P450 system in general, followed by a more detailed look at the specific protein in the system that forms the basis of this work. The P450 system is a very important and well studied aspect of biochemistry but nonetheless there are significant gaps in current knowledge; this is a result of cytochrome P450 itself being the centre of most studies with the related enzymes on the periphery receiving less attention. A substantial literature review is presented where the most important recent work is highlighted.

1.1 The Cytochrome P450 Mono-oxygenase System

The cytochrome P450 mono-oxygenase system is essential for a range of biochemical reactions and is found throughout all domains of life. The diversity of metabolic functions of the ubiquitous cytochrome P450 enzymes (CYPs or P450s) in eukaryotes includes hormone metabolism and biosynthesis, xenobiotic catabolism and fatty acid hydroxylation [3]. In humans there are 57 different P450s many of which are responsible for essential steps in the metabolism of around 95% of prescription drugs as well as a very large proportion of other exogenous compounds and toxins which alone necessitates a thorough understanding of this system and its components. Approximately 23 of the P450 genes in humans are responsible for drug and steroid metabolism whilst around 7 are for steroid biosynthesis. Developments in recent decades regarding the importance of knowing the bioavailability, metabolism and toxicity problems as early as possible in the drug development process has further highlighted the need to understand P450s and its associated system as a whole. It is thought that these enzymes became essential in the biosphere due to the need to metabolise toxic chemicals present in the environment as organisms became more

complex [4] and molecular oxygen more readily available.

The initial discovery of P450s was made in 1958 in rat liver microsomes [5]. P450s feature a heme cofactor as the catalytic centre and are therefore referred to as heme proteins. The proteins were found to exhibit very specific and unusual spectral properties which are reflected in their name. The proteins are cellular (cyto), coloured (chrome), are a natural colour or pigment (P) and absorb at 450 nm when in a complex with CO (450) [6]. As enzymes that carry out oxidation reactions the P450s require a supply of electrons so that they may carry out the reactions in their catalytic cycle, this is shown in Figure 1.1. Of particular note in the catalytic cycle is the delivery of electrons in two individual steps, rather than both at the same time as one would expect from the physiological two-electron donor nicotinamide adenine dinucleotide phosphate (NADPH).

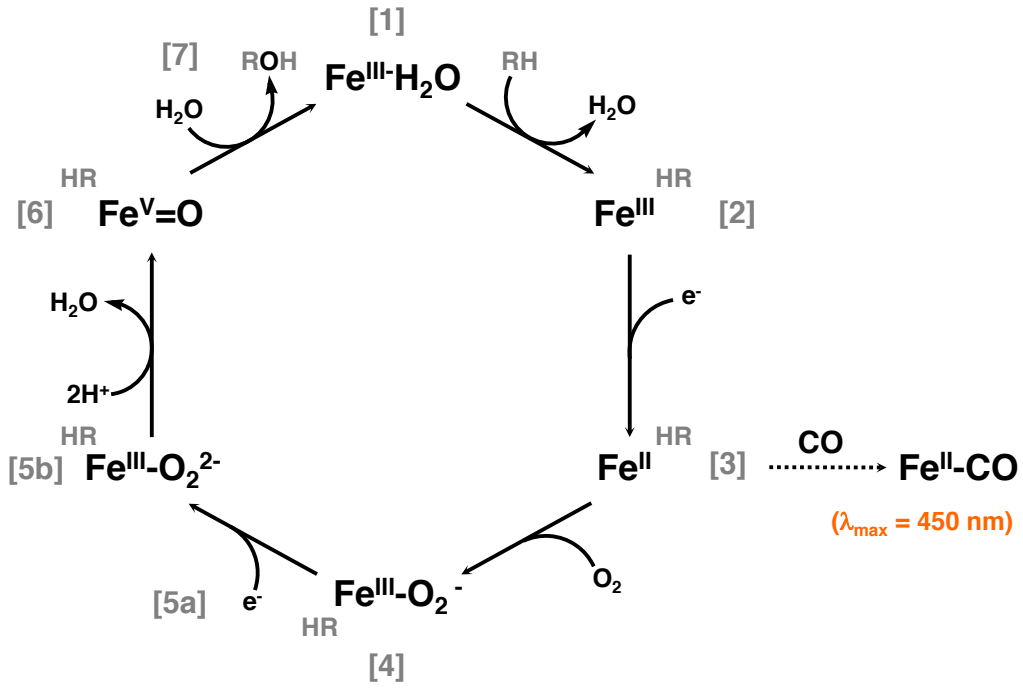

Figure 1.1: Schematic of the cytochrome P450 catalytic cycle [7]. The steps labelled with numbers are as follows: (**1**) The enzyme in the resting state as low-spin ferric. (**2**) The enzyme in high-spin configuration with perturbed water coordination. (**3**) Delivery of the first electron leading to reduction to a ferrous state, binding of CO at this stage leads to the appearance of the signature 450 nm absorbance peak. (**4**) Binding of oxygen leading to an oxy-P450 complex. (**5a**) Further reduction from a second electron transfer and formation of a peroxo-ferric intermediate. (**5b**) The formation of hydroperoxo-ferric intermediate. (**6**) Compound I and water formed as a result of protonation of the distal oxygen and hydrolysis of the O-O bond. (**7**) The final product formation through oxygen transfer from heme to substrate, regenerating the ferric heme.

The overall reaction catalysed by P450s is

$$\mathrm{RH} + \mathrm{O_2} + 2\,\mathrm{H^+} + 2\,\mathrm{e^-} \longrightarrow \mathrm{ROH} + \mathrm{H_2O}$$

where RH is the substrate and ROH is the oxidised product. The atoms of the single oxygen molecule are distributed between the substrate and water in the products of the mono-oxygenation reaction. All of the reactions catalysed by P450s are essentially oxygen insertion but there is some variety in the final outcome of the reaction. In addition to hydroxylation of unactivated carbon centres P450s are capable of epoxidation of olefins, the addition of oxygen to heteroatoms such as sulfur, the dealkylation of amines and the formation and breaking of carbon-carbon bonds. some of these reactions are of particular interest in human health and disease such as the *O*-demethylation that occurs in the conversion of codeine into morphine.

The biochemistry of P450 catalysed reactions will not be described in further detail but a discussion of the two major classes of P450 mono-oxygenase systems is important. There are two major types of P450 mono-oxygenase systems that have striking differences, these are known as class I and class II.

Class I P450 systems are found in the inner mitochondrial membranes of eukaryotes, and in most bacteria. In this system the electrons are transferred from NADPH to P450s via two intermediate proteins; a flavin adenine dinucleaotide (FAD) containing ferredoxin reductase and ferredoxin (an iron-sulfur protein).

Class II P450 systems are found on the outer face of the endoplasmic reticulum of eukaryotes. In this case the electron donation to P450s is provided by a single electron transfer partner known as NADPH-cytochrome P450 reductase (CPR). CPR receives two electrons from the obligatory two-electron donor NADPH or NADH via a hydride transfer before passing them in individual steps in the catalytic cycle to P450s [8]. A general schematic for the organisation of class II P450 systems in the membrane is shown in Figure 1.2.

CPR is indicated in yellow with the two primary functional domains indicated as FAD (flavin adenine dinucleaotide) and FMN (flavin mononucleotide). As is clear in the diagram, both proteins are membrane bound and feature a hydrophobic transmembrane anchor domain which stabilises the protein at the membrane surface and is understood to facilitate protein-protein interactions. The P450 is the terminal oxidase in the electron transfer chain where activation of molecular oxygen takes place. The proteins shown are usually expressed individually but self-sufficient hybrid mono-oxygenase systems such as P450 BM3 (P450 102A1) of *Bacillus megaterium* have evolved through the fusion of P450 and CPR genes [9].

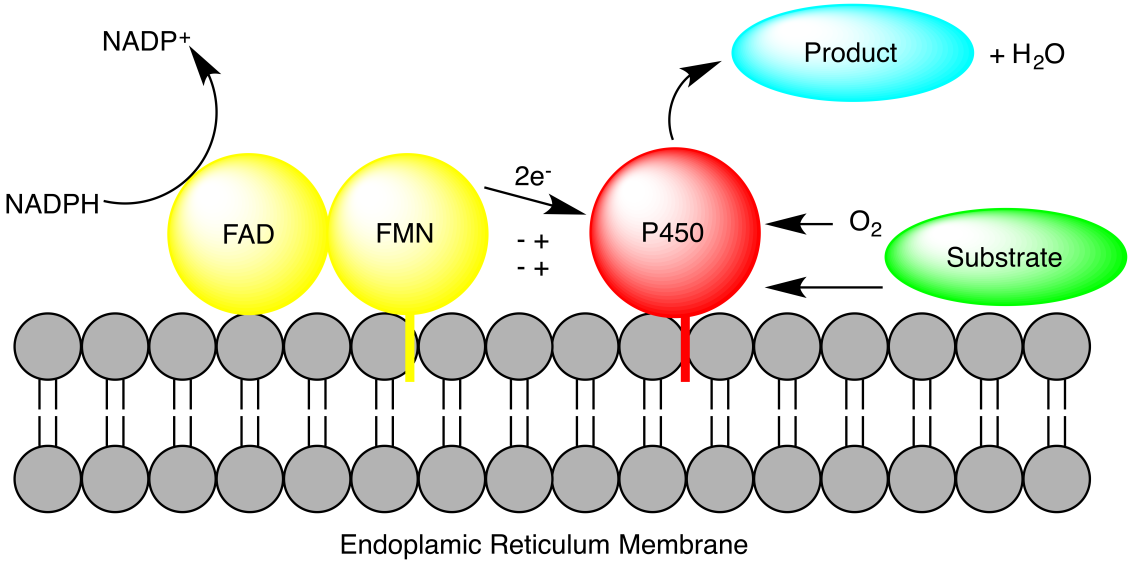

Figure 1.2: Schematic of the cytochrome P450 mono-oxygenase system. Indicated in yellow are the two primary functional domains of CPR and in red is the central P450 enzyme. Reactions are indicated by arrows.

1.2 Human NADPH-Cytochrome P450 reductase

1.2.1 Function

As mentioned in the preceding section, the primary function CPR is the membrane-bound electron transfer partner of P450 enzymes, after which it is named. However, it also has several other physiological partners including heme oxygenase [10], cytochrome b_5 [11] and squalene mono-oxygenase [12]. There are a number of non-physiological acceptors which CPR can also reduce such as cytochrome c (cyt c); this has been heavily used for characterisation of the enzyme [13, 14] and such use will be described in later chapters. CPR is active both in the membrane and when in the form of a soluble construct in which the membrane anchoring region is no longer present; though it should be noted that activity towards P450s specifically is diminished in solution, suggesting that the presence of the membrane is critical for facilitating the formation of active complexes of P450 and CPR [9, 3].

1.2.2 Structure

CPR is a membrane bound, 77 kDa protein found primarily on the surface of the endoplasmic reticulum. CPR can be isolated from the membrane of the endoplasmic reticulum by limited proteolysis with steapsin or trypsin. This releases a 72 kDa C-terminal hydrophilic soluble enzyme that is incapable of reducing P450s but is able to oxidise NADPH and pass electrons onto other soluble acceptors, such as cyt c.

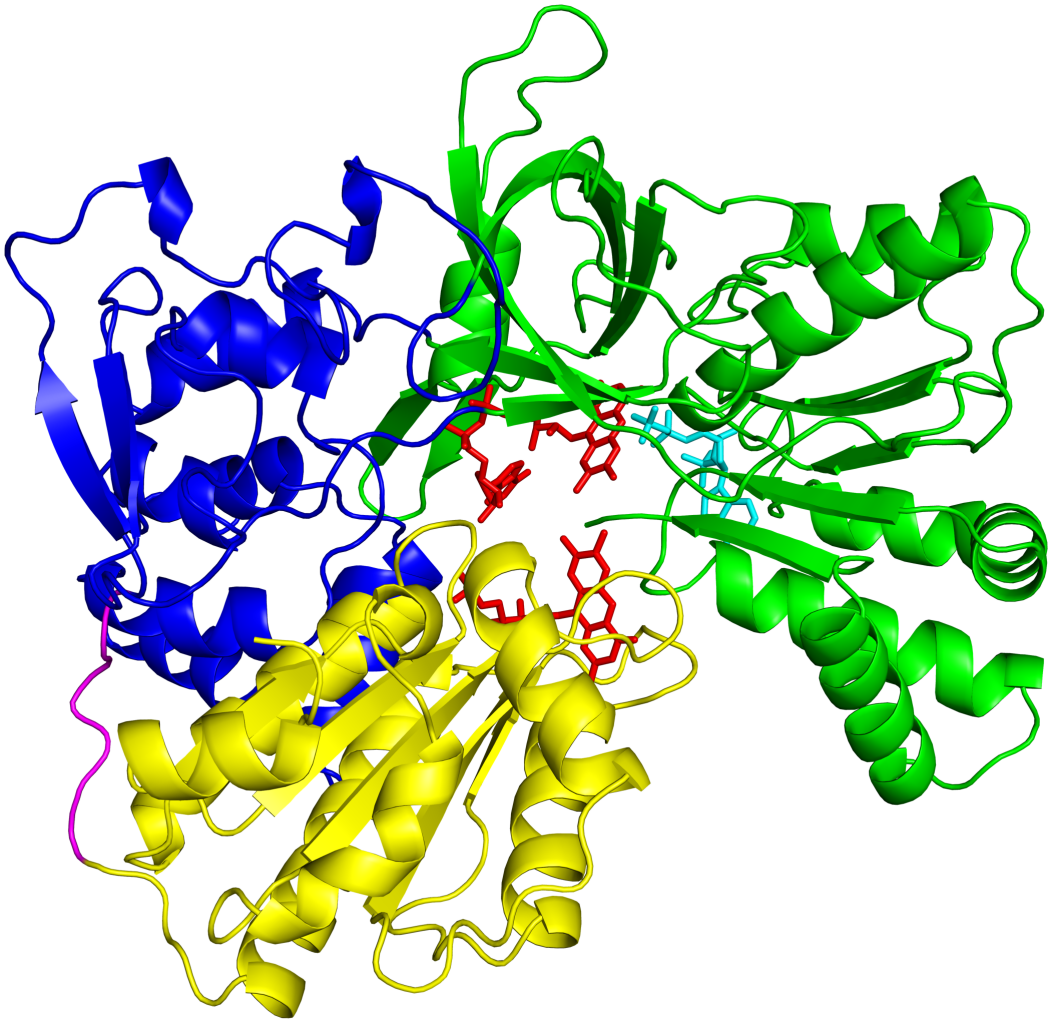

Figure 1.3: Crystal structure of CPR. The FMN-binding domain (**yellow**), FAD-binding domain (**green**) and the linker domain (**dark blue**) and flexible hinge region (**magenta**) are shown in a cartoon representation. The corresponding flavin cofactors (**red**) and NADPH (**light blue**) are shown as lines.

CPR consists of four domains, the structure and organisation of which were first fully characterised by X-ray crystallography of the rat enzyme in 1997 by Wang *et al.* [15]. The crystal structures that have been obtained to date are of a soluble truncated form of the enzyme in which the N-terminal transmembrane anchoring domain is not expressed. Figure 1.3 shows a more recent structure (PDB ID: 3QE2) obtained from the human enzyme [2]; the domains revealed in the structure are: an FAD- and NADPH- binding domain (green), an FMN-binding domain (yellow), and a linker domain (blue). Additionally, the cofactors are shown as line structures: FAD and FMN (red, in their respective binding domains) and NADPH (cyan). Of particular note in Figure 1.3 is the loop (magenta) connecting the FMN-binding domain to the linker region. This highly flexible loop was not clearly resolved in

either the rat or human X-ray crystal structures of the enzyme; in this figure it was filled in using the minimal electron density that was present.

Perhaps the most striking feature of CPR is the presence of the diflavin redox centre which has been the focus of many studies and is responsible for the catalytic activity of the enzyme [16, 17, 18, 19, 20]. CPR is in fact a member of a family of diflavin reductases that have been of significant biological interest and a number of reviews now exist that discuss their importance [21, 22, 19]. The structure of CPR reveals that the tightly bound flavin cofactors are very close to one another, with only around 4 Å edge-to-edge distance between their respective isoalloxazine rings. This distance would permit very rapid electron transfer between the two flavins but the conformation would be very restricting for access of electron transfer partners to the catalytic centre. It is widely accepted that the flexible hinge and linker domain are responsible for the repositioning and stabilising of the FMN domain in order to facilitate intermolecular electron transfer. In addition to the crystal structures of CPR the, structure of the isolated FMN domain has been determined by NMR and X-ray crystallography [23].

The catalytic domains of CPR share a great deal of structural homology with bacterial flavodoxins (FMN binding domain) [24] and ferredoxin reductase (FAD/NADPH binding domain) [25] – hinting at the evolutionary predecessors of CPR. Two other human diflavin proteins have been identified and studied to a substantial degree which feature homologs of CPR, these are nitric oxide synthase (NOS) [26] and methionine synthase reductase [27]. Figure 1.4 illustrates the structural similarity between CPR, another diflavin reductase and the evolutionary predecessors.

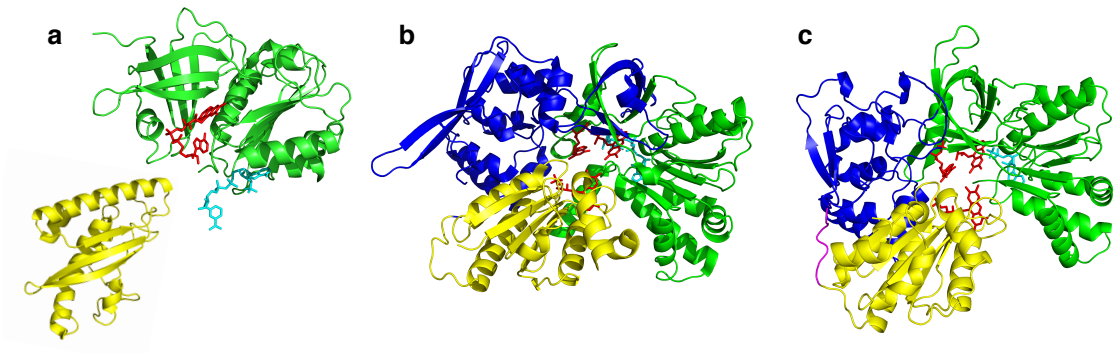

Figure 1.4: Crystallographic structures of diflavin reductases and of their ancestor proteins. The domains of each structure are coloured as in Figure 1.3 so that the corresponding domain in each protein can be identified. (**a**) Structures of a flavodoxin (PDB ID: 3KPA) and a ferredoxin reductase (PDB ID: 2VNH). (**b**) The structure of rat NOS (PDB ID: 1TLL). (**c**) The structure of human CPR (PDB ID: 3QE2).

1.2.3 The Electron Transfer Mechanism of CPR

As mentioned in the previous section, perhaps the most significant feature of CPR for its catalytic function is the presence of two flavin molecules as tightly bound cofactors. These molecules are characterised by their ability to engage in 1- and 2-electron redox chemistry and remain relatively stable as radicals. In CPR they are the essential intermediate between NADPH and the heme iron centre of P450s.

Studies to determine the kinetic properties as well as the pathway of electrons through CPR have been carried out extensively using assays, pre-steady state and stopped-flow kinetics, and potentiometry [3, 28, 29, 30]. Earlier studies were able to establish that the general electron pathway is NADPH to FAD then distribution between FAD/FMN and finally to the P450's heme iron [31, 32, 18, 33, 34]. It is the reduction potentials of the flavins that have been determined to primarily govern the electron flow in CPR [22, 35]. The midpoint potentials of the flavin cofactors were determined by anaerobic redox titrations of the isolated domains and the whole enzyme. The redox potentials of the isolated domains and of the whole protein were found to be very similar. The precise values determined by Munro *et al.* were:

- FAD domain E_1 [oxidized/semiquinone] = -286 ± 6 mV,
  E_2 [semiquinone/reduced] = -371 ± 7 mV
- FMN domain E_1 = -43 ± 7 mV, E_2 = -280 ± 8 mV

and the soluble diflavin reductase

- E_1 [FMN] = -66 ± 8 mV, E_2 [FMN] = -269 ± 10 mV;
  E_1 [FAD] = -283 ± 5 mV, E_2 [FAD] = -382 ± 8 mV.

These values clearly allow for the established electron pathway from NADPH hydride transfer to FAD to FMN to P450 but does not help to elucidate the precise mechanism of electron transfer between the flavins. Figure 1.5 shows the chemical structures of the possible oxidation states of the flavin molecule. The flavin co-factors can exist as the oxidised form, the one-electron reduced semiquinone, and two-electron fully reduced hydroquinone forms. Both of these forms can exist free in solution as either the neutral or anionic forms. Importantly, in the physiological pH range between 6.5 and 8.5 both semiquinones are found in the neutral blue form. The fully reduced forms are referred to as $FMNH_2$ and $FADH_2$. The oxidation and protonation states of CPR can easily be distinguished in the laboratory due to the distinct visible absorption spectrum of each species [18, 16]. These spectra have been invaluable for a range of studies carried out on the the catalytic mechanism of CPR since its initial discovery. Oxidised flavins have a broad absorption maxima at 450 and 380 nm, with the value at 450 nm commonly being used for the

determination of protein concentration in solution according to the flavin content (assuming a stoichiometric quantity of flavin). The combination of absorption at these wavelength is responsible for the distinctive yellow colour of the protein. The spectra of neutral blue semiquinones feature a broad absorbance between 500 and 700 nm. Though both of the flavins are able to form semiquinones it should be noted that while the FMNH• is air stable the FADH• is not. This is most likely to be a a result of the stabilising effect of a hydrogen bond between N5 of the FMN and the main carbonyl group of a conserved glycine reside in a nearby loop (Gly141 in rat CPR) [36].

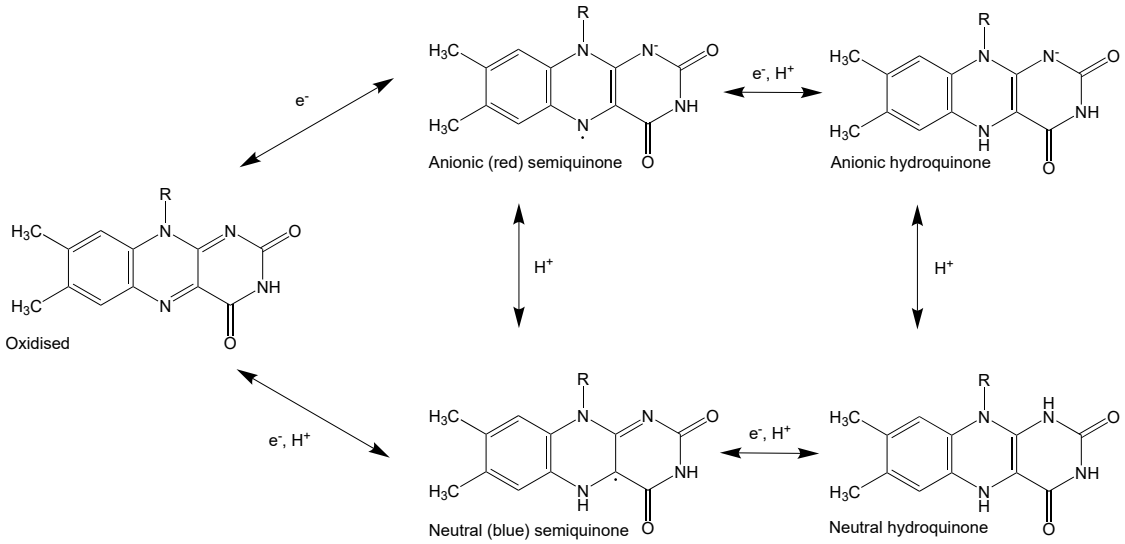

Figure 1.5: Chemical structure of the isoalloxazine ring of flavin in all redox states. The oxidised molecule absorbs in the visible spectrum to appear yellow whilst the hydroquinones appear a very pale grey/yellow. The two semiquinone configurations appear coloured as labelled.

Early studies had concluded that the physiological reduction of CPR begins with the complete reduction of the FAD to the hydroquinone form ($NADP^+-FADH_2-FMN$) by means of a hydride transfer from enzyme bound NADPH cofactor. This is followed by transfer of electrons one at a time to the FMN yielding the FMN hydroquinone species ($FMNH_2$). The electrons are finally passed sequentially to P450s at individual steps in the catalytic cycle. This separation of the two electrons is a crucial function of CPR and is almost certainly the evolutionary reason for the presence of two flavin molecules. The system is not entirely this simple, since it is strongly suspected that the redox states of the flavins exist in equilibrium. For example, the two electron reduced species ($NADP^+-FADH_2-FMN$) almost certainly exists in a mixture of predominantly $FAD-FMNH_2$ and FADH•−FMNH• based on spectroscopic findings [35, 32]. Brenner *et al.* were able to propose proportions of the enzyme in each of the states which was found to vary with the pH of the buffer solution, where at low pH values the $NADP^+-FADH_2-FMN$ is favoured and at

high pH more of the FADH•−FMNH• is present [37].

It has been proposed that during catalysis the flavins exist in electron configurations of 1-3-2-1 or 2-4-3-2; where the numbers represent the number of additional electrons beyond the oxidised form [30, 38, 22]. The 1-3-2-1 configuration was expected to be the more physiologically relevant because the reduction potentials of the flavins allow these states to be reached more easily with NADPH, and the air-stability of the semiquinone form. CPR has been shown to be stable in air as a 1-electron reduced species (FMNH•) and often purifies from *Escherichia coli* (*E. coli*) in this form. More recent research has also proposed a 0-2-1-0 configuration which assumes that the cycle always begins and ends with fully oxidised flavins [22, 39]. Although the 4-electron reduced species has been shown to form, it is not generally considered physiologically relevant as it requires incubation with a significant molar excess of NADPH for several hours in order to form; or alternatively the use of a much stronger non-physiological reducing agent [22].

In comparison to P450s, there is a significantly less complete understanding of the catalytic cycle of CPR. This is partly due to fewer comprehensive studies but also due to the difficulty of following the multitude of possible redox states, electron transfers and conformations that are likely to exist throughout the cycle. A recently proposed catalytic cycle, along with predicted conformations of CPR is shown in Figure 1.6 [40]. Data presented in the same study suggested that domain reorganisation of CPR can be triggered by the delivery of electrons.

1.2.4 Domain Motions

The concept of an energy landscape in folded proteins necessitates that proteins exist as an equilibrium population of conformational states [43, 44]. Interconversions between these states are known to be of fundamental importance to the biological function of the enzyme but remain incompletely understood [45, 46]. The internal motions of proteins can range from bond vibrations, through localised loop movements to large-scale domain motions [47, 48, 27, 49, 50, 51]. The time scale can also range greatly from femtoseconds for the smallest motions to microseconds and even seconds for larger-scale motions. A small selection from throughout the ranges has already been studied, including local loop motions and larger scale domain movements [52]. The importance of the latter is particularly clear in proteins involved in electron transfer (ET) pathways, systems that feature domain motions intrinsic to their function.

ET proteins, such as CPR, are typically associated in large and dynamic complexes and a single protein often contains multiple redox centres. In such systems, domain motion is required to provide access for the protein and cofactors. It has

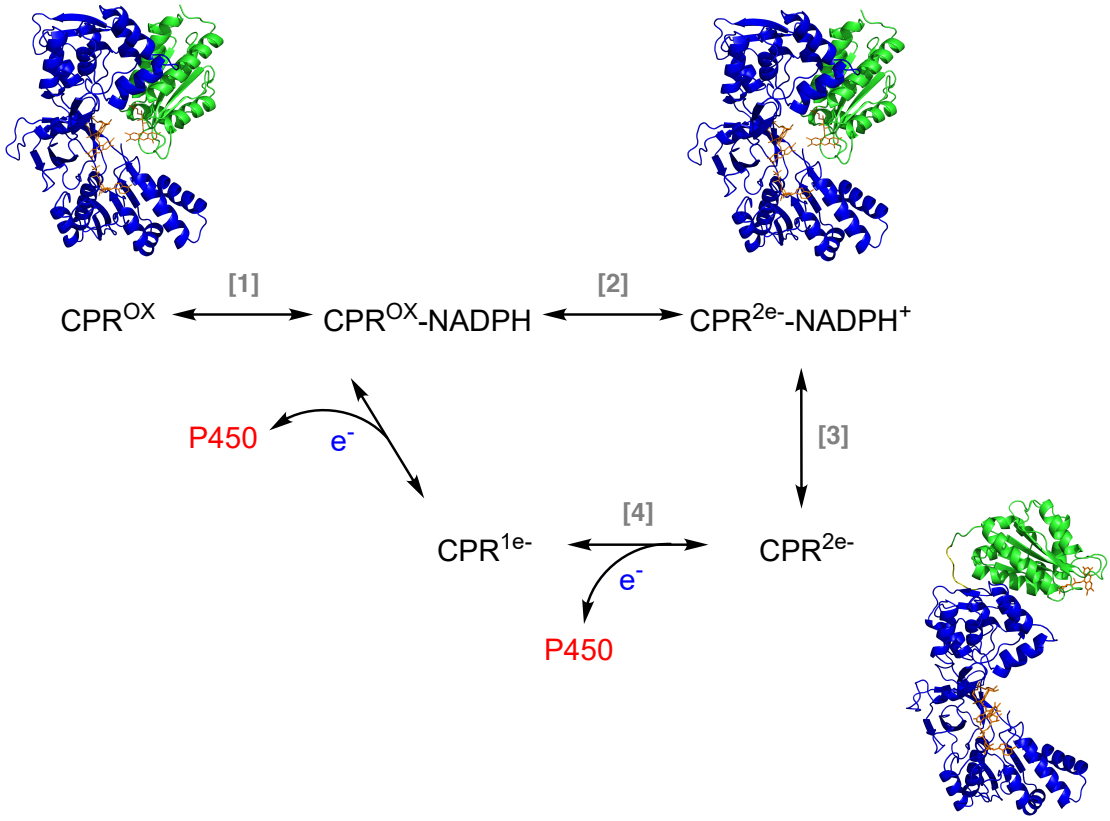

Figure 1.6: Proposed catalytic cycle of CPR. Models of the predicted conformational state of the molecule are detailed in the relevant steps. (**1**) NADPH binds to the oxidised form of the enzyme which is predominantly in the closed conformation. (**2**) The flavins are reduced via a hydride transfer after movement of Trp677 to allow access to the isoalloxazine ring for the nicotinamide ring and the electrons are distributed accordingly between the two (interflavin electron transfer). $NADP^+$ remains bound and CPR maintains a more compact conformation. (**3**) $NADP^+$ is released and CPR proceeds to adopt a more extended conformation and at this stage the NADPH binding site becomes sterically hindered by a loop movement at Asp632. (**4**) CPR proceeds to interact with electron transfer partners whilst in an extended conformation and undergo intermolecular electron transfer before returning to the oxidised state in step 1. Figure adopted from Huang et al. [40], where the FAD-binding and linker domain are coloured blue and the FMN-binding domain is in green, with additional information from Hubbard et al. [41] and Xia et al.[42]

been implied that large scale domain motions could be responsible for limiting the rate of such reactions to the millisecond timescale which is many orders of magnitude slower than the intrinsic electron transfer rate [53, 54, 55, 56]. The importance of large scale intra- and inter-molecular protein dynamics in regulating biological electron transfer is beginning to be recognised but a detailed characterisation is an unresolved problem. The issue is exaggerated by the experimental difficulties that arise as a result of most of the systems involving membrane bound proteins.

An important family of ET proteins which depends on domain movement in this way is that of the diflavin reductases, which includes CPR, mammalian nitric oxide synthase (NOS), the cancer-related novel reductase and methionine synthase reductase, as well as the bacterial proteins sulfite reductase and P450 BM3. These enzymes (or their reductase components) have domains in common: an FMN-binding domain, related to flavodoxins, an FAD- and NADPH-binding domain, related to ferredoxin/flavodoxin reductases, and a 'linker' domain, which may serve to position the other two domains. The FMN domain is connected to the linker and FAD domains through a highly flexible 'hinge'. In all the members of this family the ET pathway involves the sequence NADPH $\rightarrow$ FAD $\rightarrow$ FMN $\rightarrow$ acceptor, and motion of the FMN-binding domain has been inferred to allow it to accept electrons from the FAD and deliver them to the acceptor. The crystal structures of various CPR molecules including from rat [15], human [2] and yeast [57] reveal a distance of around 4 Å between the two flavin cofactors. This would very easily permit intramolecular electron transfer between the two but access to the catalytic centre for other molecules would be severely hindered.

Studies into the rate of interflavin electron transfer have revealed rates in the region of 30-60 s^{-1} [58, 59]. This is significantly lower than that of the intrinsic electron transfer rate which is predicted to be in the region of 10^{10} s^{-1} based on the separation distance between the two cofactors in the crystal structure. It is believed that the process may be conformationally gated; crystal structures exist showing CPR both in a more compact and a more extended shape which provides further evidence that the large scale motions in the predicted relative orientations of the domains are possible [60, 42].

It has previously been established that CPR accepts two electrons from the obligatory physiological donor NADPH which are then distributed between the two flavins, resulting in a mixture of FAD/$FMNH_2$ and FAD•/FMN• [39, 20, 28, 58, 33]. With the $NADP^+$ still bound the conformation is has been proposed to be more compact in order to provide the correct arrangement for interflavin electron transfer. Upon dissociation of $NADP^+$ it has been postulated that the structure will adopt a more extended form where access to the FMN is available to P450s or another relevant electron acceptor. These changes and their predicted occurance during the catalytic cycle are detailed in Figure 1.6.

Recent Studies on CPR

A number of recent studies which have attempted to elucidate the nature and causes of the domain motion that CPR undergoes when carrying out its function will now be discussed. The most direct evidence for domain motions comes from crystal structures of mutants that crystallise in more open conformations, as mentioned

briefly above. These crystal structures featured CPR with a distance between the cofactors ranging from 30 to 60 Å. However, the limitation of this evidence is that the way the molecule crystallises is not necessarily indicative of how it behaves in its native environment when anchored to a membrane. These mutants also suffered from orders of magnitude lower catalytic rate for the reduction of cytochrome *c* and P450, or in some cases, lost the activity altogether [60]; this highlights the importance of a dynamic system and how the enzyme must have the flexibility to return to the closed conformation in order to undergo interflavin electron transfer during catalysis.

Although less ideal than studies in the membrane it is accepted that solution studies are able to give a more accurate interpretation of the conformational behaviour of the molecule than in crystalline form. The first two major studies in solution used electron double resonance methods in the case of Hay *et al.* [61] and a combination of nuclear magnetic resonance (NMR) and small-angle X-ray scattering (SAXS) in the case of Ellis *et al.* [62]. Both of these studies revealed that the oxidised form of human CPR exists in solution as a mixture of two or more conformations. At least one of the conformations was consistent with the published crystal structure of the wild-type as a 'closed' conformation and the other being an 'open' conformation which could be compared to those crystal structures previously mentioned previously in Hamdane *et al.* or theoretical models. Both studies also observed a shift in the conformational equilibrium upon reduction of the flavin cofactors by NADPH. In cases where the nucleotide was still found CPR favoured a somewhat less open conformation. A further study by Huang *et al.* [40] attempted to present a more complete understanding of the conformational equilibrium by using a greater range of reducing agents and redox states. Importantly a small investigation using small-angle neutron scattering (SANS) was carried out in an effort to circumvent the photoreductive effect of X-rays on the redox state of the flavins which would likely lead to an ambiguous result when studying the oxidised form. This investigation resulted in the proposal of a catalytic cycle annotated with possible conformational states in each step (Figure 1.6).

A study carried out in 2011 by Xia *et al.* [42] was able to demonstrate the importance of domain motion to catalysis in a more direct way by engineering a disulfide cross-link between a residue in the FMN domain and another in the FAD domain. The cross-link severely reduced the flexibility of the molecule by locking the two domains together and severely reducing the rate of interflavin electron transfer and electron transfer to partner enzymes (over 90% reduction). Subsequent reduction of the disulfide cross-links restored the catalytic activity to normal values. This investigation also presented crystal structures of the cross-linked enzyme lacking bound $NADP^+$; it is interesting to note that the flavin cofactors were in close proximity

but rotated with respect to each other compared to the wildtype which is likely a reason for the lower interflavin electron transfer.

Two studies [63, 14] focussing on the use of fluorescence resonance energy transfer (FRET) and stopped flow methods have correlated the open and closed states of CPR with steps in the catalytic cycle. This work further supported the idea of NADPH binding and reduction of the flavins producing a less extended conformation and the subsequent release of $NADP^+$ resulting in a greater proportion of molecules in the open conformation. At present there is a substantial degree of inconsistency amongst research into this area especially concerning the conformation that CPR adopts in the fully oxidised state.

Finally, limited efforts have been made to study the behaviour of CPR (and P450s) in the membrane by using nanodisc technology [64, 65, 66, 67]. Nanodiscs are small disc-shaped pieces of membrane that are kept in shape and stable thanks to a scaffold protein around the edge. Membrane proteins can then be integrated into the nanodiscs, potentially with precise control over stoichiometry, and then measured. A study that used *Sorghum bicolor* CPR integrated into nanodiscs which were then subsequently deposited on to a surface and measured with neutron reflectivity yielded limited low resolution data of changes taking place [68]. However, this demonstrated that the integration of CPRs into such membranes was viable and that the use of neutrons can render the membrane experimentally invisible to allow the nanodisc to behave as a stealth carrier either in solution or when deposited [69, 70]. A detailed description of the application of neutron scattering to the study of biological systems is provided in Chapter 2.

In summary, current research generally agrees that the molecule adopts a more compact conformation in the oxidised form and upon binding of NADP(H) to enable intramolecular electron transfer but reduction of the flavins and release of $NADP^+$ pushes the conformational equilibrium to a more open state to facilitate electron transfer to P450s. It is highly probable that such changes also occur in other members of the diflavin reductase family but there is currently little evidence for this. Details of the mechanism of domain motion as well as a precise quantification of the extent of movement has also not yet been determined, it is unknown whether the motions are stochastic or if they are strictly controlled and consistent throughout the functional cycle of the enzyme.

1.2.5 The Kinetics of CPR's Reductase Activity

A detailed understanding of the kinetics of CPR's catalytic activity is highly complementary to any structural study since both factors are clearly related, with domain rearrangement of CPR expected to play a significant regulatory role. The funda-

mental enzymatic properties of CPR have been established long ago, as discussed in Section 1.2.3., but few attempts have been made to link this to domain motions. The structural changes that the molecule undergoes facilitate and limit the catalytic activity and therefore affect the kinetic rate of the protein. Structural changes and kinetic changes should therefore be intrinsically linked and a 2014 study by Haque *et al.* highlights this [71]. This study utilised the power of stopped flow to carry out measurements of reactions in the millisecond timescale by rapidly mixing pre-reduced CPR (amongst other diflavin reductases) with cytochrome *c* and observing the formation of the reduced species of the cytochrome over time. From the spectral changes there are two very distinct steps which appeared, initially a very rapid 'burst phase' where presumably the pre-reduced CPR is able to react with the cytochrome *c* before the rate slows down to a much slower state for a longer period of time, at which point the catalytic activity is most likely limited by domain movements and interflavin electron transfer steps. This serves to highlight how domain motions are an important control for catalytic rate and serve throughout the catalytic cycle of the enzyme.

1.2.6 CPR Complex Formation

The formation of catalytically active complexes is essential for the function of CPR but there is currently very little data that enables the characterisation of such complexes. This difficulty mostly arises as a result of the challenges of crystallising flexible membrane proteins and the reluctance of CPR to interact with P450s in solution. To date there has been only one study yielding atomic resolution of a complex between CPR and an electron transfer partner; in this case heme oxygenase [72]. In this study by Sugishima *et al.* a soluble mutant form of CPR was used which was previously crystallised by Hamdane et al. [60] (a four-residue deletion mutant referred to as ΔTGEE) and was found to adopt a more open conformation in crystal form. The average resolution for this complex structure was 4.3 Å which was almost certainly limited by the poorly resolved FMN domain of CPR which suggested that its orientation varied from molecule to molecule much more than any other part of the complex. This further supports the idea that movement of the FMN domain relative to other parts of the enzyme is essential for complex formation and therefore catalytic function. A more significant discussion of complex formation between CPR and an electron transfer is given in Chapter 5.

This study is primarily aimed to gain a further understanding of the domain motions that CPR undergoes both as a function of redox state and buffer conditions as well as upon formation of a complex with an electron transfer partner. These changes are studied over various timescales. A more detailed summary of the aims

is given at the end of the following chapter, which will serve as an introduction to the primary technique used throughout this study.

Chapter 2

Small-Angle Scattering

As the principal analytical technique that appears throughout this work, this chapter will be dedicated to introducing the concept of radiation scattering and in particular the unique applications of small-angle scattering (SAS) to studying biological systems. Both small-angle X-ray scattering (SAXS) and small-angle neutron scattering (SANS) will be described. Beginning with an introduction to the sources of radiation and the instruments that harness their power, the chapter will progress into a discussion of the fundamental mathematical theory and finish with routine ways in which the data can be analysed in order to demonstrate the results which can be obtained.

Both X-ray and neutron scattering experiments are conceptually the same and can be explained through the same mathematical formalism and therefore, where possible, it can be assumed that any description applies to both unless otherwise stated. X-rays and neutrons are scattered by the atoms in a sample; the primary difference being that X-rays interact with the electron density and neutrons with the nuclei of atoms. This means that unique experiments can be carried out depending on the type of radiation used, the nature of the sample and the different sources available. Scattered radiation can either be coherent in nature, where the waves are in-phase and produce a higher amplitude wave through constructive interference, or incoherent which is unwanted destructive interference and typically subtracted from the experimental data. In structural studies elastic scattering (i.e. where no change in energy of the scattered radiation takes place) is typically measured. It is becoming increasingly common to carry out inelastic or so-called quasi-elastic scattering experiments in order to study the dynamics of biological systems [73, 74], but at present this is a very niche technique for this purpose so further descriptions will be omitted from this chapter.

This chapter is followed immediately by the aims of this thesis including the key biological questions, showing how the techniques introduced here will be critical for obtaining the necessary results.

2.1 Sources

2.1.1 X-rays

The most common large-scale source of high-flux experimental X-rays is the radiation synchrotron; these facilities are found across the globe. They are cyclic particle accelerators which accelerate electrons to such an energy that they emit light at the X-ray wavelength upon a change of direction. The basic operating principle is that electrons are produced in bunches by an electron gun in a linear particle accelerator (also known as a linac) which works in a manner similar to a cathode ray tube. These bunches of electrons are then accelerated in a small booster synchrotron which fills the so-called storage ring; a long tube maintained at a very low pressure the path of which describes a polygon. The electrons can then circle for hours close to the speed of light in the storage ring where at each corner of the polygon they pass through magnets which change the direction of the electrons (effectively steering them) and cause the emission of X-ray light. The light is then directed towards and utilised on instruments at experimental stations known as beamlines after specific shaping (e.g. wavelength selection, collimation and focussing). The energy lost from the electrons during emission is replenished through the use of radio frequency (RF) cavities around the storage ring which produce an electromagnetic field.

The first type of commonly found magnet is the bending magnet which is located at intervals around the storage ring in order to maintain the correct direction of the electron beam and upon doing so cause X-ray light to be emitted tangentially to the plane of the incident electron beam. This emitted light tends to cover a broad spectrum of wavelengths and is not very focussed or brilliant. Undulators, also known as insertion devices, are the other common magnet type which function by causing the electron beam to adopt a wavy or undulating trajectory. At each undulation the beam emits light which overlaps and interferes with each consecutive emission and produces a very focussed and brilliant beam. These magnets are typically found at beamlines where a more intense source of X-rays are required for the experiments, for example time-resolved studies.

There now exist several examples of modern high-brilliance 3rd generation (greater than 10^{18} photons $s^{-1}\,mm^{-2}\,mrad^{-2}$) synchrotron light sources including the Advanced Photon Source (APS, Chicago, USA) and the European Synchrotron Radiation Facility (ESRF, Grenoble, France). This level of brilliance is many orders of magnitude greater than conventional X-ray tubes, is more highly collimated, more tunable and is pulsed. Moreover, the time-structure of the beam, in pulses, can be exploited for specific time-resolved studies. These facilities are constantly being improved and upgraded to provide even more brilliant X-ray beams, but will soon meet strong competition from X-ray free-electron laser sources (XFEL) [75, 76, 77, 78].

XFEL sources are able to produce X-ray pulses with laser properties and much higher brilliance than conventional synchrotrons with the potential to mitigate the radiation damage often experienced before sufficient data is collected.

2.1.2 Neutrons

Neutron sources are much less common than those for X-rays, primarily due to the higher costs of materials, lower demand and longer measurement times. At large scale facilities neutrons are produced in one of two ways, either through nuclear fission in a reactor or through spallation.

High-power reactor-based neutron sources are based on the nuclear fission chain reaction of a fissile element, typically ^{235}U. These sources can be either continuous like the Institut Laue-Langevin (ILL, Grenoble, France) or mechanically pulsed like at IBR2 (Dubna, Russia). An example of the nuclear reaction of ^{235}U is

$$ {}^{1}_{0}\mathrm{n} + {}^{235}_{92}\mathrm{U} \longrightarrow [{}^{236}_{92}\mathrm{U}] \xrightarrow{85\%} {}^{139}_{56}\mathrm{Ba} + {}^{94}_{36}\mathrm{Kr} + 3\,{}^{1}_{0}\mathrm{n} $$

where n is a neutron and the products are an example of one possible outcome; of note is the 3 neutrons which promote the sustained chain reaction. The remaining 15% of neutron absorption results in radiative capture

$$ {}^{1}_{0}\mathrm{n} + {}^{235}_{92}\mathrm{U} \longrightarrow [{}^{236}_{92}\mathrm{U}] \xrightarrow{15\%} {}^{236}_{92}\mathrm{U} + \gamma $$

where the products are the compound nucleus $^{236}_{92}$U and gamma radiation as a result of the absorbed neutron decaying to its ground state. The neutron beams are then guided the the beamlines and then shaped, using collimators, wavelength selectors and different sized slits before being used to probe samples. Since neutrons are neutral particles they cannot be steered or accellerated so there is no way of directing or storing them and then will eventually be affected by gravity when travelling over long distances. A great deal of neutron flux is lost during the initial stages of production and guiding.

Spallation sources, on the other hand, work by targeting high energy protons from a proton accelerator at a heavy metal target (such as tantalum, liquid mercury or tungsten) to produce excited nuclear states. These then decay through spallation emitting neutrons, γ-rays and neutrinos without initiating a chain reaction. Examples include the continuous source at SINQ (Villigen, Switzerland) and more common pulsed sources at ISIS (Oxford, UK) and SNS (Oak Ridge, USA). A new spallation source which will provide the highest flux in the world is currently in development in Sweden and is known as the European Spallation Source (ESS).

2.2 Instrumentation

Since the theory behind SAXS and SANS is so similar it's no surprise that the respective instrumentation also shares a great deal of similarity. In this section the SANS diffractometer D22 at the ILL will be used as a model for describing the basic operating principle of a SANS instrument and BM29 at the ESRF will be used as an example of a basic SAXS instrument in order to compare and contrast the two. These beamlines are very typical in their layout and details of a more unusual SAXS beamline will be presented later in the relevant experimental chapter.

ILL D22

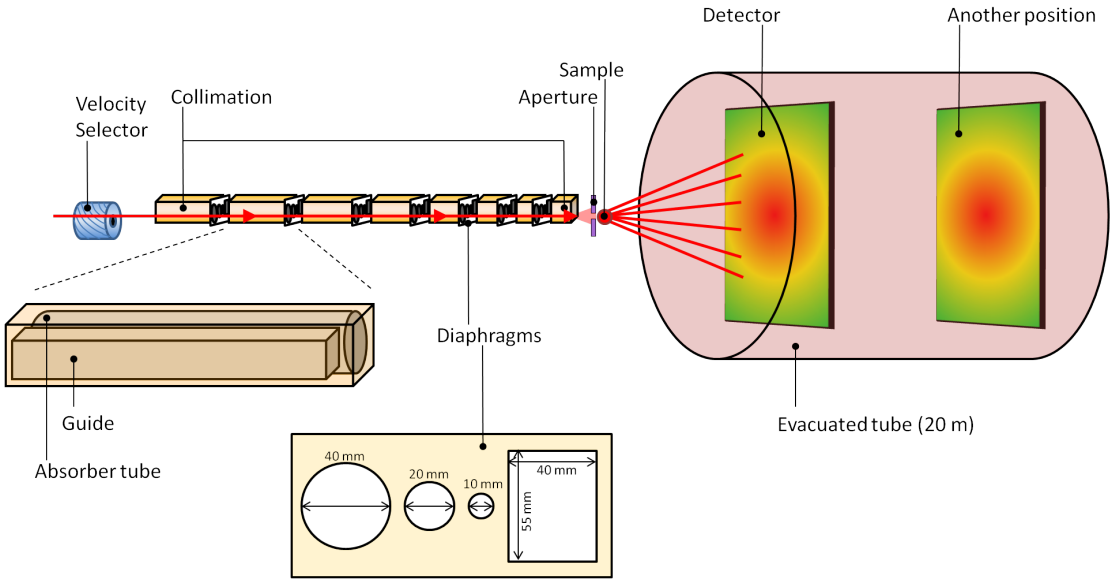

Figure 2.1: Schematic of the ILL D22 SANS Diffractometer. Indicated by a red line is the neutron beam and a more detailed structure of the diaphragms and collimation assembly are shown in the lower middle and left of the figure.

The SANS diffractometer at D22 [79] beamline at the ILL is a state-of-the art example of its kind with the highest flux at the sample in the wavelength range of 0.4 to more than 4 nm. This is mostly thanks to the brilliant cold-neutron source that the instrument is fed by from the ILL's reactor, a sophisticated velocity selector with a short rotor length and high transmission, a large beam cross-section and a shortest sample-to-detector distance of 1.4 m. In addition to this, D22 features the world's largest ^{3}He multidetector with an active area of 1 m^2. The detector is situated in a 20 m long evacuated tube providing sample-to-detector distances ranging from 1.4 to 17.6 m thus covering a total Q-range (the dynamic range of the instrument indicating the largest and smallest particles that can be measured) of 0.0004 to 0.85 Å^{-1}.

Figure 2.1 shows a schematic diagram of the general layout of D22. After passing through the mechanical velocity selector (minimum wavelength of 4.5 at Å 28,300 rpm) the beam is collimated though an absorber tube which ensures that the entire neutron beam is travelling parallel to a specified direction until it reaches the sample. An appropriate level of collimation is selected according to the sample, by varying the collimation length from 1.2 to 17.6 m, which itself can be in a various environments from simple quartz cuvettes in a temperature controlled holder through to a capillary with flowing samples from a liquid chromatography system [80].

Perhaps the most significant superficial differences between a SAXS and a SANS instrument are in the detectors, which in the case of SAXS is typically a photon counter or charge coupled device (CCD) and for neutrons is a ^{3}He detector; though new technologies are being developed in response to a global shortage of ^{3}He supply. Due to the different wavelengths and physical properties of neutrons the instruments tend to be much larger to allow the use of long sample-to-detector distances and evacuated detector tubes.

ESRF BM29

BM29 is a bending magnet SAXS beamline at the ESRF which is dedicated to the measurement of biological macromolecules in solution. In the case of BM29 the maximum detector distance is 2.867 m yieding a Q-range of 0.0025 to 0.5 Å^{-1}.

Figure 2.2 shows a schematic of the beamline. A non-standard addition to this SAXS beamline is the *in situ* FPLC system which has the significant value of ensuring sample monodispersity, an absolute requirement for *ab initio* shape reconstructions of the particle. The helium filled flight tube in between the sample and the detector helps to reduce the amount of attenuation of X-rays by air scattering since the beamline does not have an evacuated metal flight tube as SANS instruments

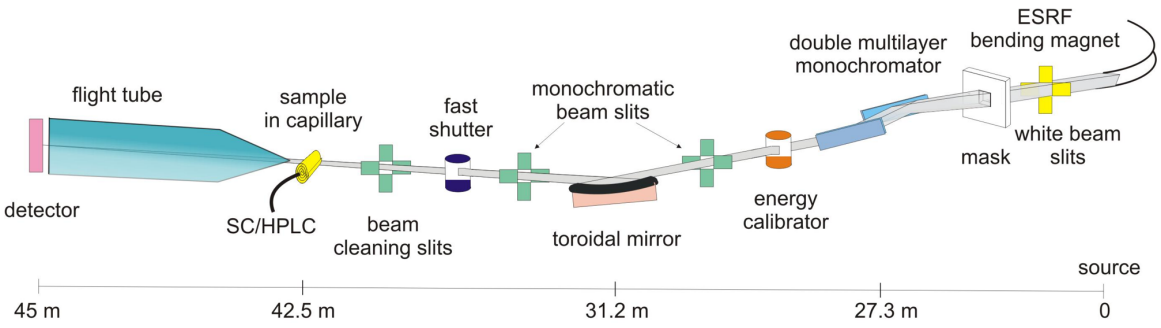

Figure 2.2: Schematic of the ESRF BM29 SAXS beamline. Where SC/HPLS is a sample changer/high performance liquid chromatography sample environment [81].

typically do; this reduces cost but limits maximum sample-to-detector distances yielding lower Q-ranges. Typically longer Q-ranges on SANS instruments means that larger structures can be measured with neutrons which are less readily attenuated by gas molecules, meaning that a reasonably well evacuated detector tube is enough for sample-to-detector distances of tens of meters. The typical specifications of both D22 and BM29 are summarised in Table 2.1.

A great advantage of X-rays over neutrons is the very short data acquisition times thanks to the higher flux of the source which is many orders of magnitude greater than any neutron source. This enables a greater range of samples and conditions to be measured within the allocated experimental time - this is particularly important in high demand user facilities. X-ray beamlines also produce data with a much better signal-to-noise ratio than neutrons, thanks to both the higher flux, narrower beam and less scattering from the buffer. The broad beam in neutron facilities is necessary to obtain a high enough flux and to not waste neutrons but leads to broadening of the signal. In order to offset the large incoherent scattering from the buffer in neutron solution experiments one can increase the contrast between the sample and solvent by using D_2O rather than H_2O which allows the signal to be subtracted more easily. More importantly, the contrast of the sample can be tuned to distinguish components of a complex particle which is generally accepted to be the most common reason for using neutrons rather than X-rays in SAS experiments, described in more detail in Sections 2.4.2 and 2.4.4. A final and very important comparison between the two is the effect of X-ray radiation exposure on the sample; this has been part of and the subject of a large number of studies especially in biological and soft matter fields where the samples are often more susceptible to these effects which can easily skew the results of an experiment [82, 83, 84, 85, 86]. Neutrons are a very soft form of non-ionising radiation which have little to no effect on most samples. Typically the worst effect is activation via neutron capture of certain molecules such as salt in a buffer solution but this is rare. X-rays on the other hand are a form of strongly ionising radiation that most commonly form radicals in from the solvent which leads to radiation damage of a sample which could render it unusable after even very short exposures. Certain types of photosentitive biological molecules such as those with metal centres are especially sensitive to direct radiation damage [87].

Instrument	Monochromator	Collimator	Flight Tube	Detector	Q-Range	Flux	Beam Cross Section
D22	Velocity selector	Absorber tube	Vacuum (detector inside)	^{3}He tubes	0.0004 to 0.85 $Å^{-1}$	10^8 neutrons s^{-1}	55000 x 40000 µm
BM29	Double multilayer	Toroidal mirror	Helium (detector outside)	CCD	0.0025 to 0.5 $Å^{-1}$	10^{12} photons s^{-1}	700 x 700 µm

Table 2.1: Typical specifications of two example SAS instruments using neutrons (D22) and X-rays (BM29)

2.3 Basic Scattering Theory

2.3.1 Elastic Scattering

For the purposes of this description both X-ray photons and neutrons are considered to be radiation waves which have the associated quantum mechanical properties. Scattering techniques using neutrons and X-rays have been used for decades to provide information on the spatial arrangement of atoms and molecules. Most high resolution structures throughout history have been determined using X-ray diffraction via Bragg's law

$$\lambda = 2d \sin \theta/2 \tag{2.1}$$

where λ is the wavelength and θ is the angle [88]. However, this law does not apply to non crystalline materials since d, the distance between crystallographic planes is indeterminate in a solution. The lower level of order present has lead to use of the term scattering, rather than diffraction, for solution experiments.

When radiation passes by a nucleus or its electron density one of several events may occur. It can pass without any interaction, be absorbed, or undergo scattering which can be either coherent or incoherent. Elastic scattering is caused by the interference of waves emitted by individual scatterers within the scattering volume, where they, such as a homogeneous mix of protein molecules, have correlated positions in space. The direction of the incident wave vector is changed but kinetic energy is conserved. In elastic scattering experiments the incoherent scattering from the sample is interpreted as background noise and is subtracted from the final dataset.

According the the Born approximation, this scattering process is described by a Fourier transformation which gives a reciprocity between the dimensions of the scatterer, meaning that the larger the real size, the smaller the reciprocal size. Therefore small dimensions, such as individual nuclei will scatter at large angles or scattering vectors (in reciprocal space, known as Q-values) and very large dimensions, such as a whole protein will scatter at small Q-values.

The scattering process involves a translation from the real space of the coordinates to the reciprocal space of the scattering vector, Q

$$Q = 4\pi \sin \theta/\lambda \tag{2.2}$$

This yields a scattering curve of scattered intensity (I) as a function of the scattering vector, known as $I(Q)$. According to

$$I(Q) = P(Q)S(Q) \tag{2.3}$$

whereby $I(Q)$ is intrinsically related to the form factor ($P(Q)$), the amplitude

of a wave scattered by an isolated atom, and the structure factor ($S(Q)$) being the intensity of scattered radiation per scattering unit. These terms will not be described in further detail but in essence the form factor describes the scattering within particles and the structure factor describes the scattering that arises from the mutual interactions of particles.

2.3.2 Resolution and Contrast

It is important to note that perhaps the greatest limitation of SAS is that the resolution/information content in a scattering pattern is a result of randomly positioned particles in solution. Therefore one can only increase the nominal resolution of the scattering pattern, not of the individual scatterer. It is technically possible to measure solutions at higher resolution (theoretically as high as 2 Å), usually though wide-angle X-ray scattering (WAXS) where information at large Q-values is obtained, but even with WAXS it is not possible to uniquely reconstruct individual structural models.

A final important concept that will be briefly introduced here is that of contrast. As was mentioned at the beginning of this section, X-rays interact with the electron density of a sample and for neutrons it is the nuclei. The contrast is defined as the difference in scattering power between the scattering particle and the surrounding solution. In the case of X-rays the electron density of the solution can be modified through the addition of of small molecules such as salts or sugars but typically there is sufficient contrast already between a protein or DNA and H_2O that no further steps are necessary. For example the electron density of the average protein is 4.20×10^2 e nm^{-3} and pure H_2O is 3.34×10^2 e nm^{-3}, giving a contrast of 0.85×10^2 e nm^{-3}.

In the case of neutrons a large contrast can easily be obtained by using a D_2O based buffer solution and a hydrogenated scatterer. The limited flux at the sample in neutron experiments mean that enhancing the contrast is necessary to obtain a signal of sufficient statistical quality. The coherent scattering length of hydrogen is -3.74×10^{-12} cm whereas for deuterium it is 6.67×10^{-14} cm, therefore the contrast can be changed significantly by exchanging the deuterium content in the aqueous solution or the dissolved macromolecule. There are other important ways in which this phenomenon can be exploited which will be described in the next section where the specific application of SANS in biology will be discussed.

2.4 SANS in Biology

2.4.1 Applications

The unique data that can be obtained from SANS of biological macromolecules in solution is well established but not widely used due to the specialist large scale facilities that are needed in order to produce neutrons. As discussed previously, access to smaller Q-values is necessary for studying large dimensions of scatterers in solution and therefore small-angle neutron scattering is perfectly suited to studying the shapes and sizes of biological macromolecules.

For the most part, the use and analysis of SAXS data from biological systems is conceptually the same as for neutrons. However there is a unique feature of neutrons which is the ability to distinguish between isotopes of hydrogen (protium and deuterium) and therefore elucidate additional structural information.

Recent decades have seen a large increase in the popularity of studying biological systems using SAS such that a generalised roadmap is now generally accepted for how such investigations should be carried out [89, 90]. The typical main points in the procedure are as follows:

- Preliminary characterisation - purity, concentration, monodispersity, matched solvent
- Small-angle scattering
- Data validation - Initial inspection, radiation damage, concentration effects, standards
- Modelling - high-resolution validation, multi-domain modelling, subunit modelling, flexibility
- Additional information - atomic models, distance restraints, symmetry, disorder

2.4.2 Scattering Length Density

The scattering length density (SLD) is a measure of the scattering power of a material. In a neutron scattering experiment the scattering lengths of individual atoms are based on the physical density of the nuclei, whereas for X-rays the scattering power is equivalent to the number of electrons. These values for neutrons are difficult to predict theoretically and are therefore determined experimentally. Figure 2.3 gives a visual representation of the scattering lengths of a few different atoms for both X-ray and neutrons. The difference between hydrogen and its isotope deuterium are particularly clear in the case of neutrons.

The SLD of a molecule can be calculated from the individual scattering length of the atoms in the molecule, specifically

$$SLD = \frac{\sum_{i=1}^{N} b_i}{V_m} \tag{2.4}$$

where the sum of the scattering lengths b_i from N atoms is divided by V_m, the molecular volume, its self determined by

$$V_m = \frac{M}{\rho N_A} \tag{2.5}$$

where M is the molecular weight, ρ is the bulk density of the molecule and N_A is the Avogadro constant.

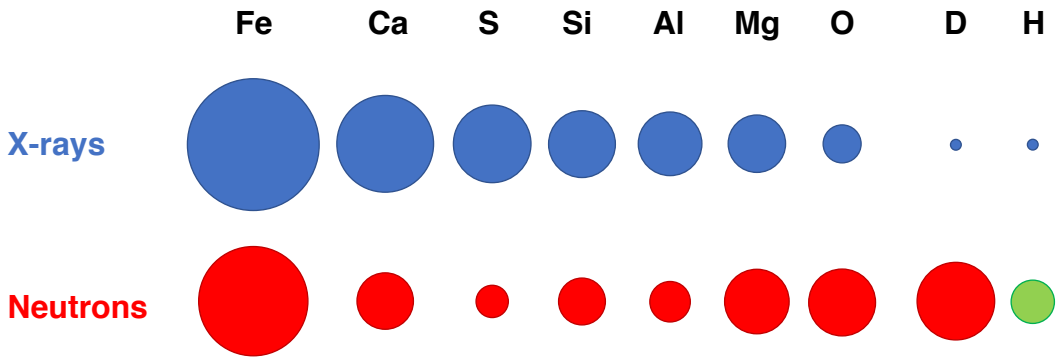

Figure 2.3: Comparison of relative scattering lengths for X-rays and neutrons of a few elements. The significant difference between the neutron scattering length of deuterium and hydrogen (**green**) is highlighted.

2.4.3 Molecular Weight Determination

The molecular weight of scatterers can be determined from SAS data and a number of important publications have shown how it can be calculated, even without knowledge of absolute intensity and contrast factors [91, 92, 93]. This is a very valuable tool for validation of the scattering curve and the sample. In the case of SANS the most commonly used formula for the determination of the molecular weight of biological macromolecules in solution is

$$I(0) = M \times c \times \frac{(SLD_M - SLD_S)^2}{\rho^2 \times N_A} \tag{2.6}$$

where $I(0)$ is the scattering intensity extrapolated to 0-angle and c is the concentration of the scatterer. In SANS it is especially important to consider the SLDs of the molecule and buffer, denoted by SLD_M and SLD_S respectively, for example

when taking measurements at different H_2O:D_2O ratios in the buffer. The margins of error (10 - 20% on the molecular weight) for these calculations are typically very low if the scatterer is very homogeneous in size and is mainly a result of error in concentration determination (typically 10% for spectroscopic methods).

A number of other methods to determine molecular weight have been developed over the years using Porod volume, dummy atom models and protein standards. These methods will be described in more detail later.

2.4.4 Contrast Variation

From Equation 2.6 one can see that the scattering intensity is directly related to the square of the contrast, which is defined as the difference in SLD between the scatterer and the solvent. Typically a hydrogenated protein will be measured in a 100% D_2O based solvent in order to provide maximum scattering signal. The large difference in scattering length between hydrogen and deuterium can be exploited through a technique called contrast variation. By adjusting the H_2O:D_2O ratio of the buffer its SLD can be adjusted to match that of one of the scatterers. In the case of multiprotein complexes selective deuterium labelling of a protein component of the complex allows the selective alteration of that component's SLD [94]. Under certain conditions, determined experimentally, the scattering density of the solvent will match that of one component, rendering it experimentally invisible. Contrast variation can therefore specifically highlight one or another member of the complex. Figure 2.4 offers a visual representation of solvent variation in the study of a biological macromolecules in a complex.

In this instance at 0% D_2O the protein and the DNA members both have specific contrast to the solvent SLD so the resulting curve will represent the full complex. Once the D_2O content reaches 42% the contribution of the protein to the coherent

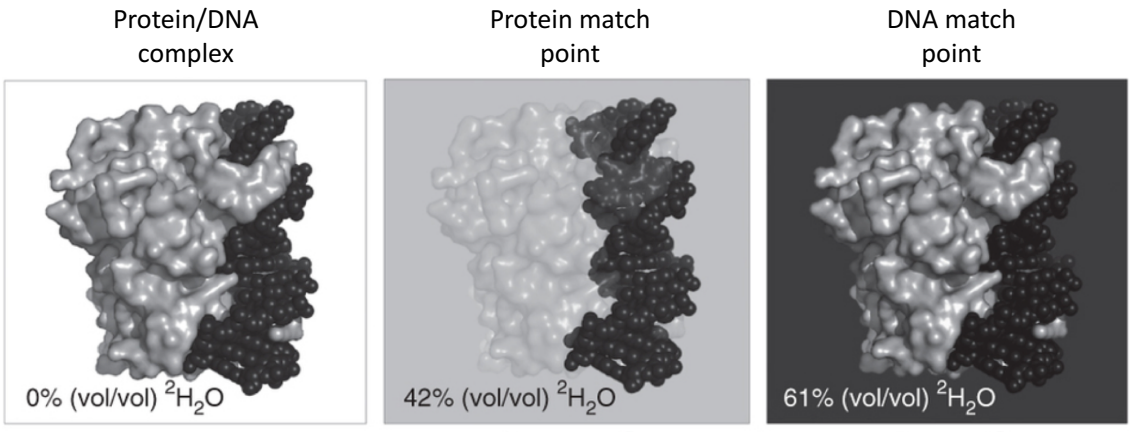

Figure 2.4: Diagram to demonstrate the experimental effects of buffer contrast variation of a protein-DNA complex in solution [1].

scattering is almost zero, therefore matching it out, so that the resulting curve represents only the complexed DNA. Increasing the D_2O content of the buffer to 61% renders the complexed DNA matched out and experimentally invisible allowing the protein alone to be measured [95]. As a result the position and structure of each member of the complex is available. By contrast, in SAXS these molecules composed of similarly light atoms would have approximately the same SLD and only the structure of the full complex would be measured.

2.5 SAS Data Analysis

Here an overview of some of the information that can be obtained from SAS data is provided. The concepts presented here apply generally to both SAXS and SANS. After collection, SAS data are reduced (radial averaging), merged (curves collected at multiple detector distances) and subtracted (buffer/background subtraction); these stages of data treatment will be discussed in more detail in the methods sections. Following this, the most common procedure is to produce a series of standard plots of the reciprocal space data which yield a number of important results straight away. This allows a very rapid determination of the quality of the data as well as a number of basic parameters from the scattering particles in the solution. The data are then typically converted into real-space for additional analysis and modelling.

2.5.1 The Guinier Plot

The Guinier plot is a representation of the low-Q region of the scattering curve [96]. This plot allows the determination of the radius of gyration (R_g) by plotting $\ln[I(Q)]$ *vs* Q^2 using the Guinier approximation. The expansion of the equation is

$$I(Q) = I_0 \exp\left(\frac{-Q^2 R_g^2}{3}\right) \tag{2.7}$$

$$\ln[I(Q)] = \ln[I_0] - \frac{Q^2 R_g^2}{3} \tag{2.8}$$

Mathematically, the radius of gyration is the distribution of parts of an object around an axis or centre of mass but in this case it is being used as the effective size of the scattering particle which is independent of the absolute intensity at zero angle, I_0 and of any specific model. There are several factors that are know to give unwanted influence on the radius of gyration, namely polydispersity, instrumental smearing and inter-particle effects. This parameter provides a basic check on the monodispersity and validation of the expected size of the sample. However, this parameter can also be independently obtained by using the concept of the pair-distance

distribution function (PDDF) also known as the distance distribution function or $P(r)$, discussed in Section 2.5.4. $P(r)$ is determined using data that has been converted to real space, as opposed to the reciprocal space of R_g and is often considered to be more reliable.

Importantly, this equation allows the determination of the forward scattering intensity (I(0)) which is an extrapolation of the linear Guinier plot to the vertical axis which will yield a theoretical scattering intensity at 0-angle; an important factor in Equation 2.6 for molecular weight determination.

2.5.2 The Porod Plot

The Porod region corresponds to a probed range smaller than the scattering objects so that the scattering radiation is probing the local structure of the particle. The Porod plot, $\log(I)$ *vs* $\log(Q)$, yields information about the so-called *'fractal dimension'* of the scattering objects [96]. At high-Q one can approximate with

$$I(Q) = \frac{A}{Q^n} + B \tag{2.9}$$

or

$$\log[I(Q) - B] = \log(A) - n\log(Q) \tag{2.10}$$

A Porod slope $n = 1$ is obtained for scattering from rigid rods; a slope $n = 4$ represents a smooth surface for the scattering particle; whereas a slope n between 3 and 4 characterises rough interfaces of fractal dimensions D with $n = 6 - D$. this is called a surface fractal.

In principle, the plot is able to inform on the general 3D shape of the average scattering particle in the solution as well as on the flexibility.

Power law	Characteristic shape
Q^{-4}	Spherical (very globular)
Q^{-3}	Thin circular disk
Q^{-2}	Gaussian chain (random coil)
Q^{-1}	Thin rod

Table 2.2: The power laws and associated characteristic shapes as defined in Porod's law.

2.5.3 The Kratky Plot

Kratky plots emphasise deviation from the high-Q behaviour of the scattering intensity I(Q). The asymptotic behaviour of the decay of the scattering intensity in the Porod region can be used to describe the shape of the sample, according to Porod's law (table 2.1) [96]

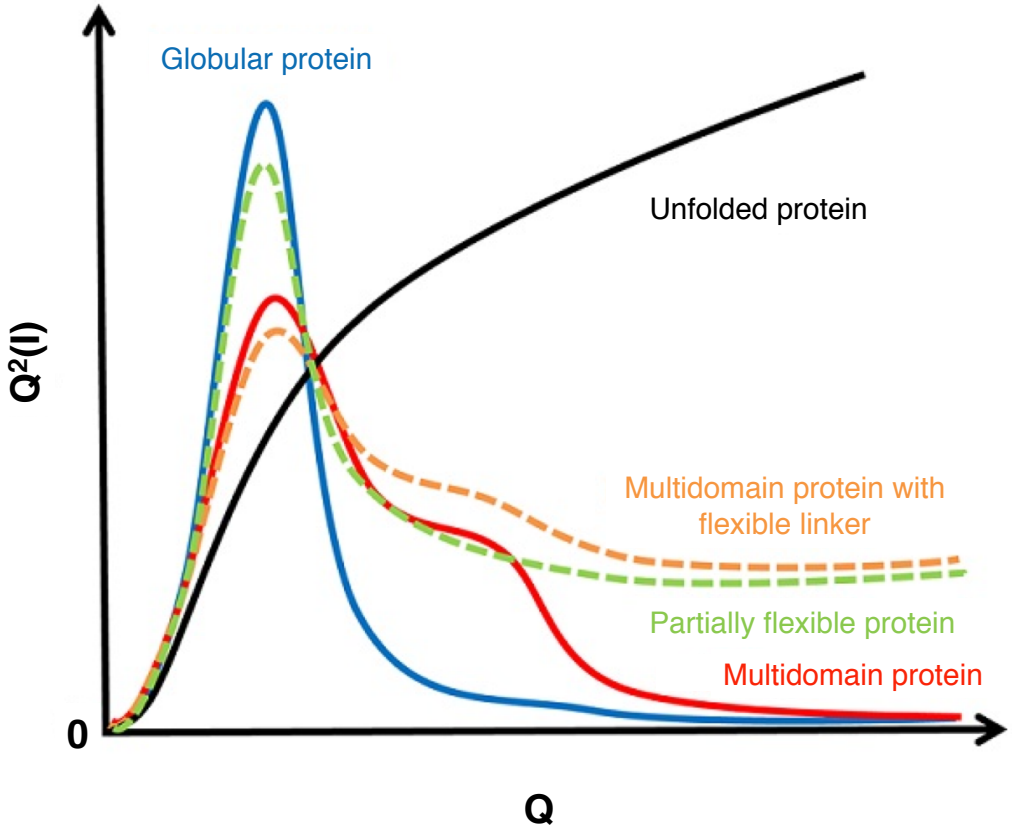

Figure 2.5: Graphical representation of typical Kratky plots. Examples of differently shaped proteins are shown in different colours with appropriate labels.

The Kratky plot of $I(Q) \times Q^2$ vs Q can therefore provide information on the globularity and flexibility of the particle in solution. This is particularly useful in the case of biological systems where the nature of the protein's folding or the flexibility of multidomain proteins can be quickly examined by observing the shape of the curve. If the protein is unfolded or has pronounced flexibility then the curve will never converge to the horizontal axis. Although perhaps the first qualitative plot to analyse the globularity and flexibility of the scatterer, it is not the only one. More recently the Porod-Debye plot has become popular for the same types of qualitative analysis as part of the data validation process [97], this is discussed later in Chapter 4 where it is applied to experimental data.

2.5.4 The Distance Distribution Function

For many further analyses it becomes desirable to work in real space rather than the reciprocal space of the earlier plots and therefore a Fourier transformation of the scattering curve ($I(Q)$) of the scattering particle is introduced in order to produce a real-space distance distribution function. A substantial difficulty arises in that

$P(r)$ cannot be determined directly because I(Q) is not known over the full interval $0 \leq Q \leq \infty$ and because it can only be observed with statistical and systematic errors. The *'indirect Fourier transform'* was therefore introduced by Glatter in 1977 as

$$I(q) = 4\pi V_o \int_0^{D_{max}} P(r) \frac{\sin(Qr)}{Qr} dr \tag{2.11}$$

where V_o is the volume of the scatterer [98]. The integral is carried out to a value known as D_{max}, which is defined as the maximum size of any scattering particle in the solution. D_{max} is chosen to obtain the best fit to the I(Q) *vs* Q data with a R_g that agrees well with that found using the Guinier approximation (equation 2.1). $P(r)$ alone is useful for determining a very general shape of the scatterer, much like a Porod plot, but further analysis using this function is required in order to model structures. The $P(r)$ plot can be essentially summarised as a distribution of inter-atomic distances in the average scattering particle in the solution. R_g values can also be obtained from these real space plots and are usually more accurate than those from the Guinier analysis because they are less influenced by inter-particle interactions. The relationship between $P(r)$ and R_g is revealed in

$$R_g^2 = \frac{\int_0^{D_{max}} r^2 p(r) dr}{2 \int_0^{D_{max}} p(r) dr} \tag{2.12}$$

2.5.5 Modelling SAS Data

Ab Initio Shape Determination

Production of models from the scattering data alone with no additional external caveats or input is known as *ab initio* modelling [99]. For SAS data the most common *ab initio* models are produced though a method called bead modelling, where models or 'envelopes' are built up from hypothetical spherical components that in the end produce a model that represents the real-space data input.

Although based on sophisticated mathematical concepts the basic idea of an automated procedure to reconstruct low-resolution molecular envelopes proposed by Stuhrmann can be described qualitatively [100]. An initial solvent search volume defined by the D_{max} is filled with theoretical beads that are randomly modified in shape (simulated annealing) until the experimental data is fit. The choice of the shape of the search volume is left to the computer to determine, based on the input.

By its very nature SAS data only allows for low-resolution shape determination therefore any meaningful *ab intio* model should provide only a overall shape of the average scattering particle in solution. The software should usually be run for multiple iterations and then averaged in order to limit the over-fitting of smaller

structural features that may be statistically unlikely. Another significant weakness of *ab initio* modelling is the ambiguity from the fact that several shapes are able to yield the same scattering curve so caution should be exercised.

Rigid Body Modelling

A more recent and sophistical form of modelling which is still developing is that of rigid body modelling or *a priori* modelling. This is where pre-existing atomic resolution structures (prior knowledge from X-ray crystallography for example) or models divided into domains attached by flexible linkers are used to fit to the data. Molecular dynamics simulations can be be carried out on the models and then the results fit back to the SAS data [101, 102, 103, 104, 105, 106]. This type of analysis features heavily in this thesis and the specific applications of it will be described in much greater detail in the results section.

Aims and Objectives

The primary aim of this research project was to probe the domain movements in the catalytic cycle of cytochrome P450 reductase. The objective was to identify which factors influence the conformational changes and characterise and quantify the effects and changes at a level beyond that which has been achieved previously. An additional aim was to determine the structure of the complex between CPR and cytochrome *c* in solution.

This thesis has been divided in to three sections. The present section has covered the biological background of the P450 mono-oxygenase system in general and CPR specifically, as well as the theory behind and a detailed introduction to small-angle scattering. A broad range of published experimental findings related to the work presented in this thesis has been described which sets the scene and shows how the primary question that this thesis seeks to answer arose.

Part two covers the experimental section where each major experiment is presented in its own chapter. Beginning with Chapter 3 on expression, purification and characterisation of a catalytically active protein and followed by three further chapters based primarily on investigations using SANS and SAXS. The first SANS investigation, described in Chapter 4, covers the a study of hydrogenated CPR in solution in different redox states and conditions. Chapter 5 details a study of CPR in a complex with cytochrome *c* in solution, where deuteration and contrast matching SANS is employed. Finally Chapter 6 details a time-resolved SAXS experiment explaining how a stopped-flow setup was commissioned on an unusual and versatile beamline at a synchrotron and used to take measurements on CPR and cyt *c* on the millisecond time scale. This section ends with a short chapter on the overall findings of the investigations as well as conclusions which can be drawn and ideas for future work.

The third and final part, an appendix, includes all of the detailed materials and methods sections relevant to the work carried out along with supplementary figures. Publications and additional activities that directly resulted from the work in this project are included after the bibliography.

Part II

Results

Chapter 3

Purification and Characterisation of Cytochrome P450 Reductase

This chapter describes the expression, purification and characterisation of the soluble CPR constructs used throughout this work. A soluble form of CPR was expressed which features a ca. 7.1 kDa reduction in molecular weight from the removal of the N-terminal membrane binding domain from the sequence. This highly hydrophobic region is responsible for anchoring and stabilising the enzyme in the membrane. In earlier studies [107] this domain was found to be responsible for the instability/insolubility of full length human CPR in solution; the truncation was found to solve the problem and allow the protein to maintain its function. Truncation removes the ability for CPR to integrate into a membrane and also interact with cytochrome P450 enzymes [9, 3]. For this reason an alternative redox partner, cytochrome *c*, is adopted for solution enzymatic studies, allowing determination of kinetic parameters. CPR yield was characterised using a number of methods detailed in this chapter and the protein's purity and activity were unambiguously confirmed. Enzymatic competence of CPR was demonstrated using redox titrations and steady state kinetics which were also necessary preparatory steps for further experimentation. Detailed methods for all of the the techniques discussed within this chapter, as well as details of the materials, can be found in the materials and methods chapter, Appendix A.2.1.

3.1 Expression and Purification

Human CPR was expressed in *E. coli* BL21 STAR. These cells were selected for their high level of expression of non-toxic recombinant proteins. The CPR expression construct is contained in the pCS22 vector which is based on the backbone of pET22b [108, 40]; the DNA for the CPR insert was provided by Professor Roland Wolf (Uni-

versity of Dundee), and cloned into the vector by Dr. Jacqueline Ellis (University of Leicester). This expression vector specifically exploits the cold shock protein (cspA) promoter sequence which is one of several cold shock proteins that are significantly upregulated when the bacteria are subjected to a decrease in temperature significantly below the ideal growth condition. The phenomenon is exploited in the pCS22 vector to remove the need for typical isopropyl β-D-1-thiogalactopyranoside (IPTG) triggered transcription of the lac operon to induce expression. Low temperature expression is also beneficial for the stability of the enzyme post-expression and for limiting growth of bacteria during the expression phase. See the Appendix A.1.1 for details protocols and a map of the expression vector. Terrific broth (TB) growth medium was selected to provide a high level of growth and expression in the cell cultures.

It was calculated that CPR would carry a strong overall negative charge of -20.2 [109] at pH 7.8 . For this reason, a Q Sepharose anionic exchange column was used for the first stage of purification (further details can be found in Appendix A.2.1 with an example elution trace in figure). Elution of the protein by an NaCl gradient increasing from 0 to 100%, where the protein began to elute at around 20% of 1 M NaCl. This was followed using the absorbance spectrophotometer fitted to the fast protein liquid chromatography (FPLC) equipment; although both the 280 nm and 450 nm signal were followed, the high levels of impurities at this stage made the more unique 450 nm absorbance of CPR the most informative.

The highly specific NADPH binding site in CPR was exploited by a 2'5'-ADP Sepharose affinity column to further purify the protein. The typical elution from this particular column by 2'-AMP was avoided due to the difficulty of removing it from the eluent afterwards and the strong effects that it has on the enzyme's activity after purification due to the irreversible binding [20, 110]. After this column the protein sample was almost completely pure and this can be seen in the SDS-PAGE gel described in the following section and seen in Figure 3.2 which was made using a sample from this stage of the purification.

Many of the planned experiments for CPR in this work required accurate concentration determination of catalytically active protein and a highly monodisperse system. For this reason size exclusion chromatography was used to ensure that any aggregates were separated from the solution; this step also provided the additional benefit of being a way to economically buffer exchange the enzyme into a deuterium-based buffer when needed for SANS experiments. An example chromatogram from this FPLC column is shown in Figure 3.1, where a substantial main peak is clearly resolved whilst some heavier particles were separated, yielding a highly monodisperse final sample.

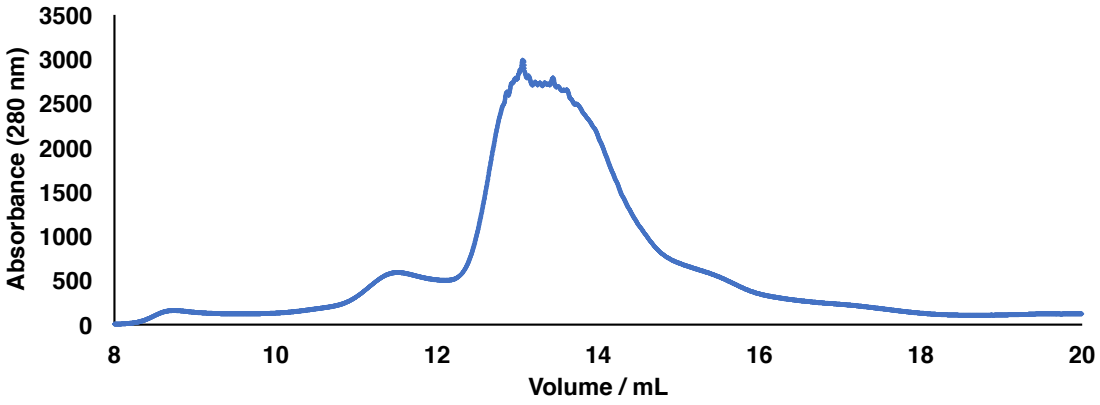

Figure 3.1: Gel filtration elution chromatogram. Superdex 200 column run at 1.5 mL min^{-1}. Fractions from the main peak (13-15 mL were collected.)

3.2 Purity

3.2.1 SDS-PAGE Analysis

SDS-PAGE was used throughout the purification process to monitor the presence of the protein in washes/eluents and to assess the final purity. By the end of the purification process only one significant band of the correct size (ca. 70 kDa) was visible in the gels which indicated that no other proteins or contaminants were present in the preparation. Figure 3.2 shows an example of a gel from a successful purification of wild-type CPR. Impurities were minimal and typically of much lower molecular weight than CPR.

3.2.2 UV-Visible Spectrophotometry Analysis

UV-visible absorption spectrophotometry was used to characterise the protein in terms of flavin content as well as the redox state of the flavins themselves. Fully oxidised CPR (flavins) had an absorption spectrum as shown in Figure 3.3. Maxima at 380 and 450 nm are observed with the peak at 450 nm having approximately +15% AU than the one at 380 nm. In the case of Figure 3.3 there was no noticeable absorbance above the baseline level at 580-600 nm suggesting a fully oxidised enzyme with no blue semiquinone presence [17, 18]. CPR typically purified in a large proportion as the air-stable 1-electron reduced semiquinone. In order to prevent this, a low concentration of potassium ferricyanide was flowed through the 2'5'-ADP column whilst the CPR was bound in order to fully oxidise it. After purification the fully oxidised protein remained stable during long term storage.

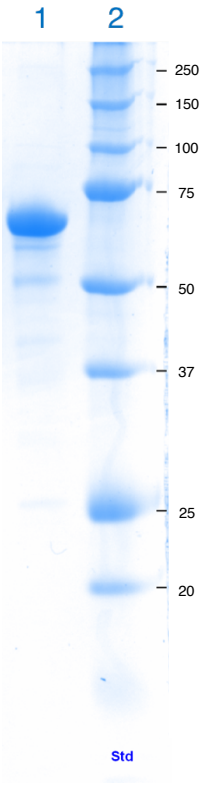

Figure 3.2: CPR purification gel. *Lane 1:* Pure CPR sample after elution from 2'5'-ADP Sepharose column in a late stage of purification. *Lane 2:* Molecular weight marker. Molecular weight in kDa is indicated by the labels in black on the right hand side.

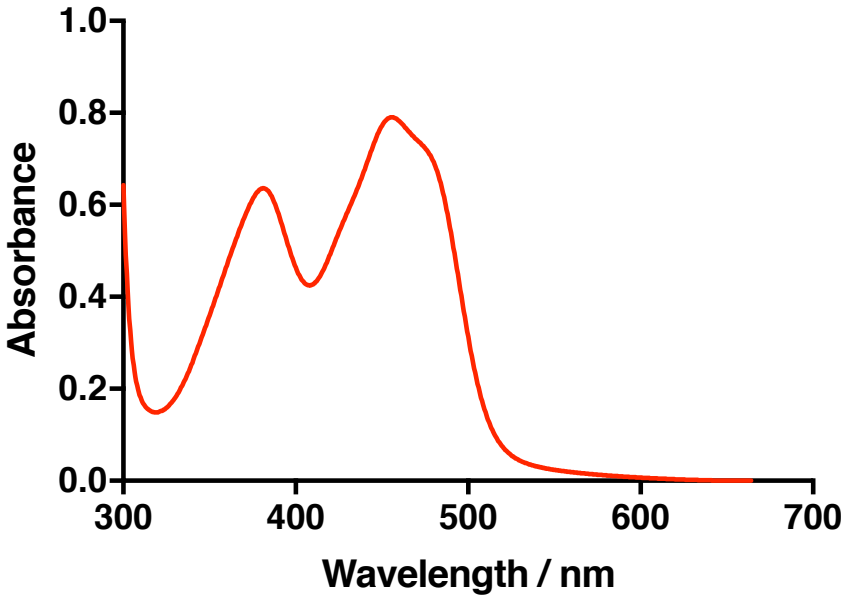

Figure 3.3: UV-visible absorbance spectrum of the flavin region of fully oxidised CPR. The sample concentration was approximately 45 µM in 100 mM BES at pH 7.0.

3.2.3 Mass Spectrometry

Mass spectrometry (MALDI-TOF) combined with peptide mass fingerprinting (PMF) was used to confirm the presence of N-terminal truncated CPR. The amino acid sequence of full-length human CPR from the UniProt database (entry: P16435) is shown in figure 3.4 [111]. The residues highlighted in green are the matching fragments from the mass spectrometric analysis. This produced an above average score for a database search of fragments which was superior to that of the BSA standard that was completed in parallel. Highlighted in red is the ∼7.1 kDa N-terminal membrane binding region which was truncated from the construct being characterised and is therefore not expected to be present in the analysis.

```
  1 MGDSHVDTSSTVSEAVAEEVSLFSMTDMILFSLIVGLLTYWFLFRKKKEE
 51 VPEFTKIQTLTSSVRESSFVEKMKKTGRNIIVFYGSQTGTAEEFANRLSK
101 DAHRYGMRGMSADPEEYDLADLSSLPEIDNALVVFCMATYGEGDPTDNAQ
151 DFYDWLQETDVDLSGVKFAVFGLGNKTYEHFNAMGKYVDKRLEQLGAQRI
201 FELGLGDDDGNLEEDFITWREQFWPAVCEHFGVEATGEESSIRQYELVVH
251 TDIDAAKVYMGEMGRLKSYENQKPPFDAKNPFLAAVTTNRKLNQGTERHL
301 MHLELDISDSKIRYESGDHVAVYPANDSALVNQLGKILGADLDVVMSLNN
351 LDEESNKKHPFPCPTSYRTALTYYLDITNPPRTNVLYELAQYASEPSEQE
401 LLRKMASSSGEGKELYLSWVVEARRHILAILQDCPSLRPPIDHLCELLPR
451 LQARYYSIASSSKVHPNSVHICAVVVEYETKAGRINKGVATNWLRAKEPA
501 GENGGRALVPMFVRKSQFRLPFKATTPVIMVGPGTGVAPFIGFIQERAWL
551 RQQGKEVGETLLYYGCRRSDEDYLYREELAQFHRDGALTQLNVAFSREQS
601 HKVYVQHLLKQDREHLWKLIEGGAHIYVCGDARNMARDVQNTFYDIVAEL
651 GAMEHAQAVDYIKKLMTKGRYSLDVWS
```

Figure 3.4: Amino acid sequence and mass spectrometry analysis of human NADPH-cytochrome P450 reductase. In red is the truncated N-terminal membrane anchor region which is not present in the soluble construct which was analysed. In green are the fragments that were identified from the analysis and in blue are the non-identified residues that were present in the construct.

3.2.4 CPR Mutants

In addition to the wild-type protein, two mutants of particular relevance to experiments in this study were selected to characterise simultaneously, these mutants had been studied to a limited extent in previous work [40]. The first is V233P/E234P, involving two residues that are located at the beginning of the flexible 'hinge' region.

The other mutant, K75E/R78Q/R108Q, is a charge reversal mutation in residues located in the FMN domain which form salt bridges to positively charged residues in the linker domain. In preliminary SAXS experiments both mutants showed increased R_g values relative to the wild-type [40], but detailed kinetic and conformational analysis forms part of the current project. The mutants behaved identically during purification and identification apart from eluting at a slightly different salt concentration from the Q Sepharose ion exchange column.

3.3 Activity

3.3.1 Steady-State Kinetics Analysis

Steady state kinetics of CPR and mutants thereof [40] were carried out to determine the quality and activity of the purified proteins. Kinetic parameters were determined and compared against reference values for the proteins under the same conditions. All proteins were found to be kinetically active reducing cyt *c* in solution.

Sample	K_M (µM)	k_{cat} (s^{-1})
Wildtype	3 ± 0.4	14 ± 1.0
V233P/E234P	16 ± 0.6	26 ± 0.4
K75E/R78E/R108Q	-	36 ± 0.6

Table 3.1: Kinetic parameters of wild-type and mutant CPR. Assays were carried out as described in Appendix A.3.3. Apparent K_M and k_{cat} values for cytochrome *c* reduction measured at 24 °C with 50 µM NADPH and variable cytochrome *c* concentrations in 100 mM BES pH 7.0 buffer.

Table 3.1 shows the kinetic parameters that have been determined for the protein samples. These correlate very well to those from previous studies on the mutants presented above which are believed to favour the open conformation and have noticeably higher catalytic rate constants and much lower K_M for cytochrome *c* [112, 40]. The K_M values for the mutants are so low that it is practically impossible to obtain an accurate value without working in the millisecond timescale. This data further suggests a correlation between an increase in extended conformation and an increase in the rate of cytochrome *c* reduction – demonstrating that conformation plays a role in the catalytic cycle.

3.3.2 Stopped-Flow Kinetics Analysis

Stopped-flow was used to further characterise the kinetics and redox behaviour beyond what would be possible by other available techniques thanks to accurate and thorough mixing coupled with fast timescales. A number of experiments, several of

which will be described throughout this thesis, were undertaken with the assistance of Dr. Jaswir Basran (University of Leicester), to observe CPR in various redox states using different reducing agents and then reacting the reduced CPR with the electron acceptor cyt *c*. These experiments follow on with ideas presented in previous studies on the wild-type protein [58, 113, 71]. Firstly, reduction of CPR by stoichiometric NADPH and NADH, observing the changes specifically at 580 nm and 450 nm. These reactions, some of which will be described here, had been characterised previously [35] but were carried out again in order to demonstrate the competence of the enzyme in adopting the necessary redox states.

Figure 3.5 shows the full spectrum of data collected after the addition of one molar equivalent of NADPH. This should be enough to obtain the first stage of the 2-electron reduced equilibrium where CPR will predominantly exist as FAD−$FMNH_2$ and FADH•−FMNH•. This was then repeated with 10 molar equivalents of NADPH over the same timescale, the spectrum is shown in Figure 3.6. In this instance there is a far more significant decrease in the absorbance at 450 nm and significantly more activity at 580 nm. In both sets of spectra the changes observed were in agreement with earlier work and the final spectra clearly resembled those of the predicted final redox state. A decrease was seen in the 350 and 450 nm peaks whilst at 580 nm the changes are less clear. Viewing absorbance against time at 580 nm only, in Figure 3.7, reveals an increase in absorbance with the addition of the first electron, reflecting the formation of the semiquinone species followed by a slight decrease in absorbance as the second electron enters where the equilibrium favours the FMN hydroquinone. Finally a more steady increase over time is observed which reflects either a slow shift in the equilibrium to an as-yet uncharacterised species or photoreduction induced by the photodiode array. These results are in agreement with similar work published by Wolthers *et al.* [52]. Further tests where CPR was examined against buffer only showed significant photoreduction effects beginning after around 5 s.

Following this, pre-reduced CPR was mixed with oxidised cytochrome *c* to observe spectral changes for this assay reaction. The observed rate of reaction was 45 s^{-1} which is almost exactly double that referenced in a previous study which was carried out at approximately half the temperature [71]. These cytochrome *c* reduction assays form a significant part of the major investigation in the following chapter and for that reason a detailed description and analysis of the assay can be found there.

3.4 Summary

The work presented in this chapter was successful in expressing, purifying and characterising highly pure and catalytically active samples of CPR and respective mu-

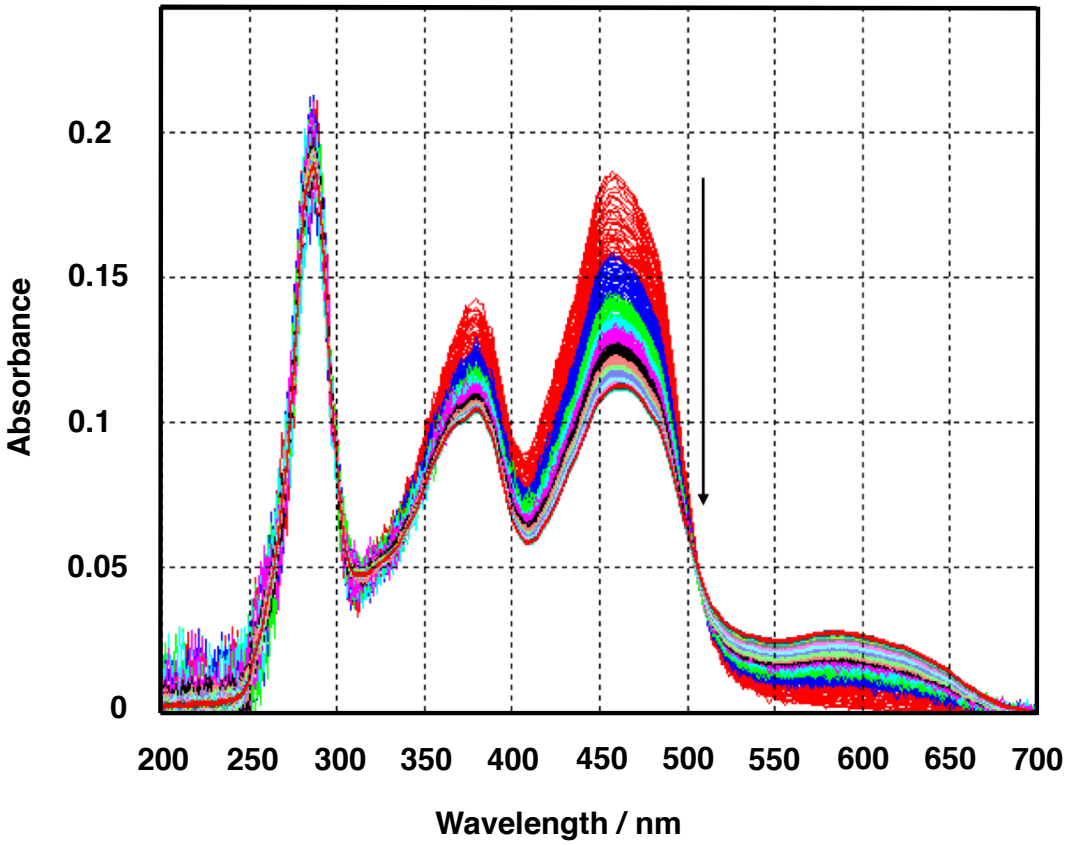

Figure 3.5: Full UV-visible spectral changes observed after mixing CPR with a single molar equivalent of NADPH in a stopped-flow system. CPR at approximately 18 µM was mixed with an equal volume of 180 µM NADPH in 100 mM BES at pH 7.0. Over a period of 10 s 400 spectra were recorded and are shown on the same plot, each trace representing a single measurement. The time points are colour coded for readability from red through to red and the direction of spectral changes are indicated by the arrow.

tants. These samples were confirmed to be of a high enough standard for a variety of further studies including SAS experiments. Although several aspects of the redox behaviour are still as yet uncharacterised, this is beyond the scope of this work and the experiments described hereafter will be within the framework of the accepted behaviour of the enzyme.

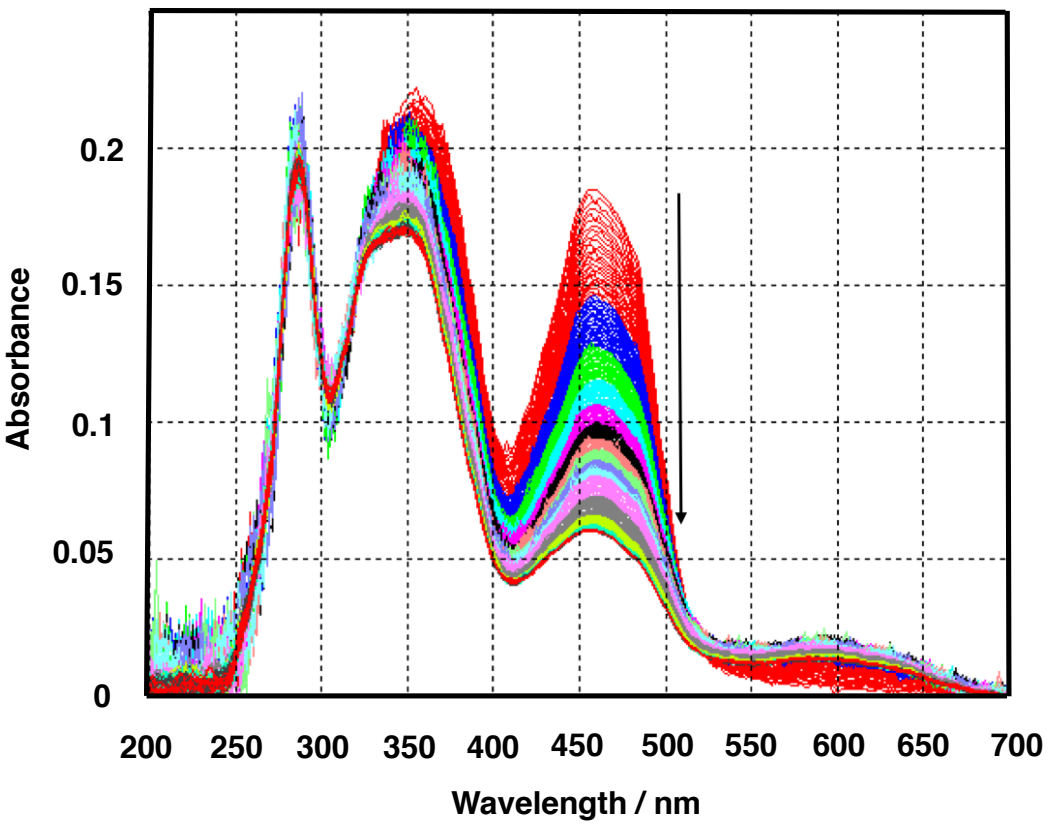

Figure 3.6: Full UV-visible spectral changes of the flavin absorbance region of fully oxidised CPR after mixing with a 10x molar excess of NADPH in a stopped-flow system. CPR at approximately 18 µM was mixed with an equal volume of 180 µ/Molar NADPH in 100 mM BES at pH 7.0. Over a period of 10 s 400 spectra were recorded and are shown on the same plot, each trace representing a single measurement. The time points are colour coded for readability from red through to red and the direction of spectral changes are indicated by the arrow. The stronger than expected absorbance at 350 nm is caused by the high concentration of NADPH which absorbs in this region.

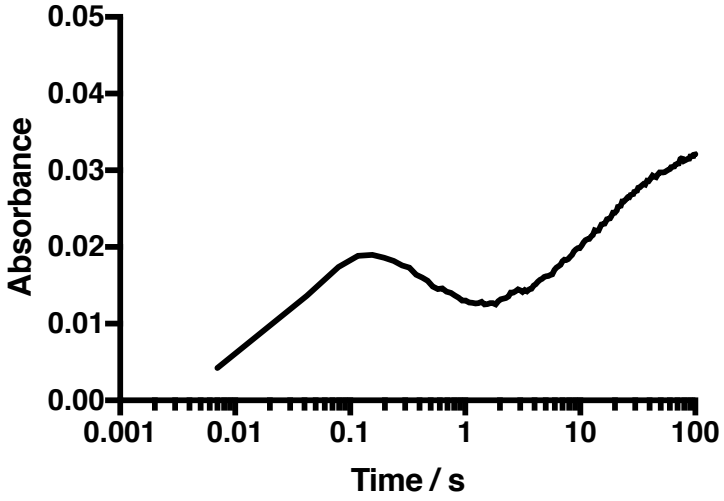

Figure 3.7: Spectral changes over time at 580nm of fully oxidised CPR mixed with a 10x molar excess of NADPH. CPR at approximately 18 µM was mixed with an equal volume of 180 µ/Molar NADPH in 100 mM BES at pH 7.0. The horizontal axis is plotted in a logarithmic scale to exaggerate and improve clarity in the region below 1 s.

Chapter 4

Orchestrated Domain Motions of Cytochrome P450 Reductase

This chapter presents the use of SANS and stopped-flow kinetics for probing the large-scale shape changes of CPR. These changes arise as a function of its change in precisely controlled redox state and buffer conditions, culminating in the definition of a conformational equilibrium. Data are presented which support the idea that domain motions are intrinsically linked to the catalytic activity of the protein and facilitate different stages of its catalytic cycle. By using SANS rather than SAXS unambiguous control of the redox state of the enzyme is possible, where there are no issues associated with reduction of the flavins by X-ray-induced photo-electrons.

The kinetics of the reduction of cytochrome *c* by CPR have been studied extensively but in this work it has been used to complement the SANS data by showing how the shape changes that are observed can be directly linked to the catalytic activity of the enzyme on millisecond timescales.

4.1 Sample Preparation

4.1.1 Redox Titrations

In order to study the protein in different redox states without ambiguity, the reactions must be carried out in an oxygen free environment since CPR is well known to auto-oxidise in air [35]. The protocol for carrying out redox titrations on CPR is well established using various reducing and oxidising agents and therefore the spectral changes that occur are straightforward to identify [38].

All redox titrations were carried out in an oxygen-free enviroment within a Belle Technologies (UK) anaerobic glove box along with a Jasco V-630 spectrophotometer and solutions in kinetics buffer (see Appendix 3.3). The glovebox was purged with nitrogen before use and the oxygen content was measured to be <10 ppm at all

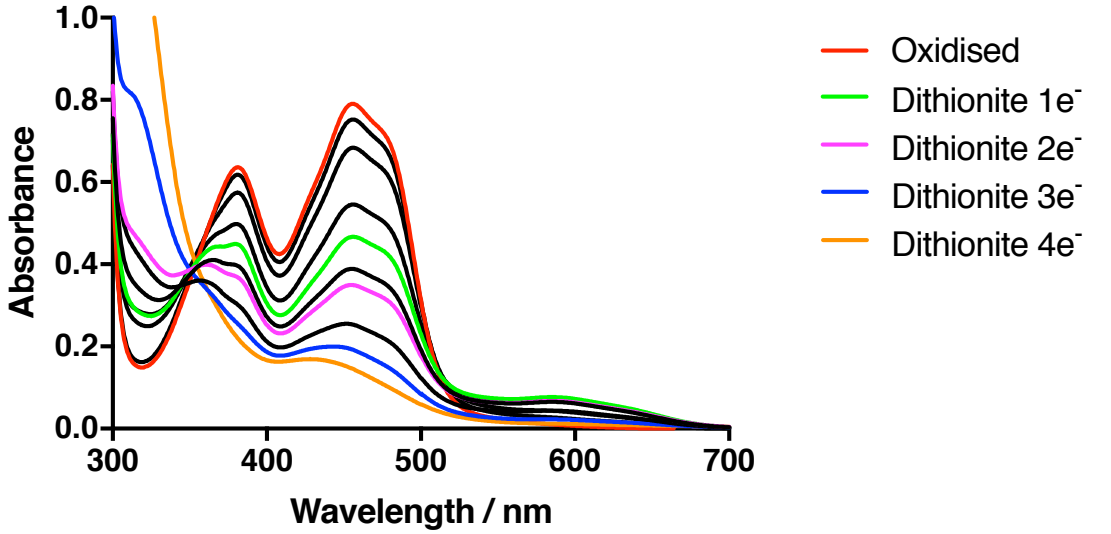

Figure 4.1: Overlaid spectra from a CPR (40 µM) redox titration using dithionite. The titration was carried out as described (see text) and the coloured spectra indicate samples that were collected for SANS measurement. Dithionite concentration was determined using UV-visible spectrophotometry and the molar extinction coefficient of $\epsilon_{315\text{nm}} = 8.04\ \text{mM}^{-1}\,\text{cm}^{-1}$ and titrated stoichiometrically into the CPR solution.

times. Any larges volumes of sample were degassed thoroughly by bubbling nitrogen through the solution for at least 1 h. A solution of fully oxidised CPR (50 µM) was used, along with either sodium dithionite ($\epsilon_{315\text{nm}} = 8.04\ \text{mM}^{-1}\,\text{cm}^{-1}$) or NADPH as a reducing agent. Stocks of 1 mM and 10 mM were made of the reducing agents, in the same buffer solution as the protein sample. Suitable titres of the reducing agent were progressively added to the protein sample taking a UV-visible absorbance scan (300-700 nm) after each titration, allowing. Selected spectra from a typical redox titration can be seen in Figure 4.1 which indicates samples that were taken with coloured traces. Stoichiometry of the reducing agent to CPR was calculated in advance to permit good estimation of when spectral changes would be likely to occur during the titrations. The reducing agent was added in a significant excess to ensure full reduction and no further spectral changes. All samples were sealed in air-tight cells for direct measurement and additionally in an airtight tube for transportation. Samples were stored at 5 °C and measured within 48 hours of preparation.

4.1.2 SANS Sample Preparation and Measurement

All solution neutron scattering and stopped-flow studies were carried out in 100 mM BES, pH 7.0, at 10 °C. The final samples were of a concentration of 1-5 mg mL^{-1} and stored at 5 °C before being measured or further purified using size exclusion chromatography (Superdex 200, GE Healthcare Life Sciences, USA) at the SANS beamline before measurement. Measurements were taken using a standard protocol for ILL D22 which is described in detail in section 8.5.1. A wavelength of 6 Å ±10% was selected as a compromise between the maximum flux (highest at 4.5 Å and lowest at 25 Å) and the available Q-range. A higher wavelength can allow smaller Q-values at long detector distances but that is not necessary for CPR since the Guinier region can already be resolved at 5.6 m sample-to-detector distance at 6 Å. The 10% bandwidth was selected to provide sufficient flux at the sample at the cost of some Q-resolution (a so-called 'pink beam').

4.1.3 Stopped-flow

The general stopped-flow setup and methodology was used as described in Appendix A.4. Burst-phase kinetics of the reduction of cyt *c* by fully reduced CPR was studied under anaerobic conditions at 10.0 °C. A pre-reduced CPR solution containing 10 µM CPR and 200 µM NADPH was incubated for 5 min in anaerobic conditions before taking measurements. The reduced protein solution was rapidly mixed with an equal volume of 100 µM cytochrome *c* (10x excess) in the 2 µL flow cell and the change in absorbance at 550 nm was recorded. A total of 2000 data points were measured over a time period of 1 s in order to ensure that the burst phase and the transition to the slower steady-state phase were observed. In order to provide an initial reading for A_{550} in the absence of reduction, the cyt *c* solution was also mixed with the buffer solution only and a baseline measurement taken. In experiments where the conditions were varied, for example changing ionic strength, the salt concentration was changed in both reagent syringes to avoid any mixing issues. The data were analysed by fitting to the appropriate model using Pro-Data SX software (Applied Photophysics, UK).

4.2 Results

4.2.1 Effects of Redox State on CPR Conformation

A range of samples was chosen for SANS measurement encompassing the various possible redox states of the flavin cofactors in CPR in order to simulate the different stages of the catalytic cycle. The samples are summarised in Table 4.1 which in-

cludes the radii of gyration, R_g and the maximum dimensions, D_{max} for each state. Figure 4.3 shows a selection of curves collected on the SANS diffractometer as well as the associated Guinier plots. The highly linear Guinier plots clearly indicate monodisperse samples which was originally a difficulty since earlier samples were not purified using size exclusion chromatography in the final stage of purification. A large Q-range was collected in order to permit analysis of both the larger and smaller scale feature of the molecules in solution. Figure 4.3 (a and b) illustrates the $P(r)$ intraparticle distance distribution function derived from the SANS data as well as the DAMMIF scattering envelopes in (c and d) derived from an oxidised and a reduced sample.

In order to separate the effects of coenzyme binding from reduction both dithionite and NADPH were used as reducing agents. It is clear from both Table 4.1 and Figure 4.3 that coenzyme binding has a substantial influence on the average size of the molecule in solution. Upon reduction there is a clear increase in the presence of more extended molecule in solution. This is evidenced by the increased R_g and D_{max} values derived from the Guinier approximation and the $P(r)$ plots (a visible tail appears on the curves at on the horizontal axes). The largest effect is seen in the reduction to the $2e^-$ level by dithionite which corresponds to the CPR^{2e-} without NADPH bound intermediate in the catalytic cycle.

By contrast, reduction to the 2-electron level by NADPH which corresponds to an $NADP^+$ bound intermediate, has a smaller effect on the size of the molecule. An almost identical effect is observed when the enzyme is reduced to the 2-electron level by dithionite and then bound to $NADP^+$ manually showing that coenzyme binding makes the reduced enzyme more compact. Low resolution *ab initio* models of the molecule are presented in Figure 4.3c (oxidised) and d (reduced). In the reduced model there is a clear extension present which is likely to be caused by the movement of the FMN domain away from the position that it occupies in the oxidised form and crystal structure.

Rigid-Body Modelling

The results presented in Table 4.1 and Figures 4.2 and 4.3 represent the average scattering particle in solution which is understood to be a conformational ensemble. In view of evidence that CPR exists as a mixture an attempt has been made to deconvolute the data and obtain a fit of the data to rigid body models. Because of the limited information content of SANS curves 'over-parametrisation' is limited by exploring the possibility of fitting just two states to the data as well as a large pool over 10,000 or more structures. This was achieved by using a modification of the software MultiFoxs [114] where a selected number of models were generated and then ensembles of varying size from a single model up to 4 or more models was fit to

Sample	Size Parameters	
	R_g (Å)	D_{max} (Å)
Oxidised	24.7 ± 0.1	71
Dithionite $1e^-$	27.6 ± 0.6	84
Dithionite $2e^-$	28.6 ± 0.4	90
Dithionite $3e^-$	27.6 ± 0.5	94
Dithionite $4e^-$	27.6 ± 0.5	89
Dithionite $2e^-$ + $NADP^+$	26.8 ± 0.4	79
NADPH 1 equiv. ($2e^-$)	27.1 ± 0.4	78
NADPH excess	26.9 ± 0.3	84

Table 4.1: Size parameters derived from the SANS data for different redox states of CPR. Showing radii of gyration (R_g) and maximum dimensions (D_{max}). Errors were in the range of ± 1-2 Å for D_{max} values and were rated as 'good' fits using GNOM in Primus (part of the ATSAS suite, see Appendix A.5.1).

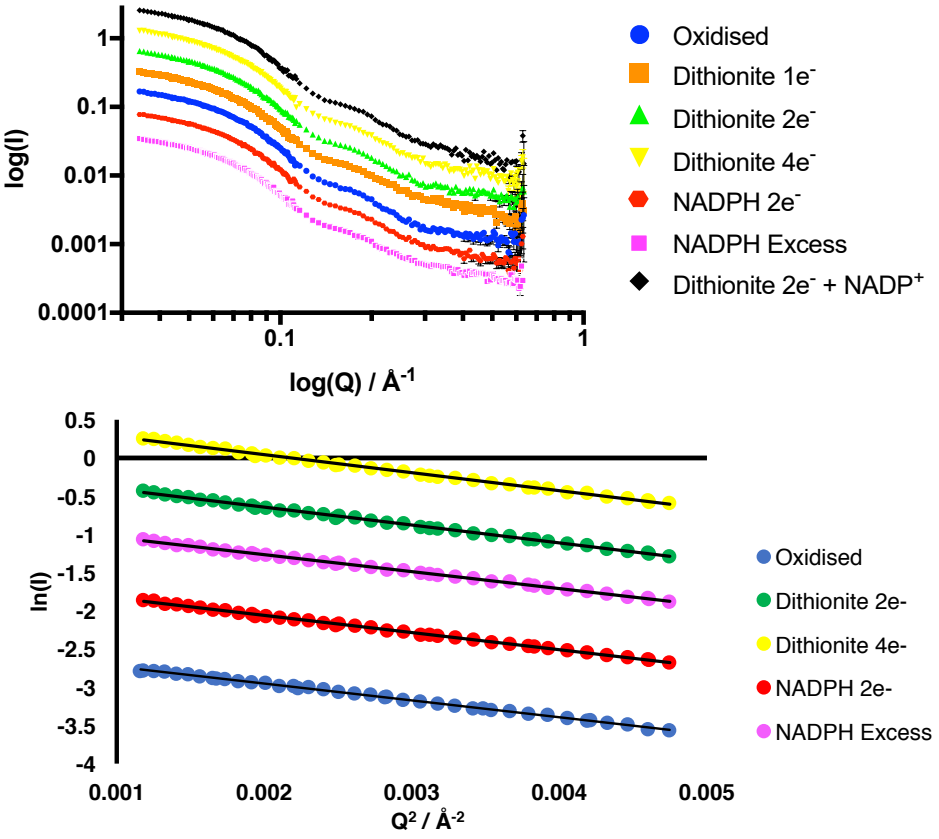

Figure 4.2: SANS Curves and Guinier plots from CPR at different redox states arbitrarily displaced along the vertical axis for clarity. The upper plot shows the SANS curves and the lower plots shows a selection of Guinier plots to demonstrate linearity. Samples were measured at a concentration of 3 mg mL^{-1} in 100 mM BES pD 7.0 at 10 °C (100% D_2O buffer).

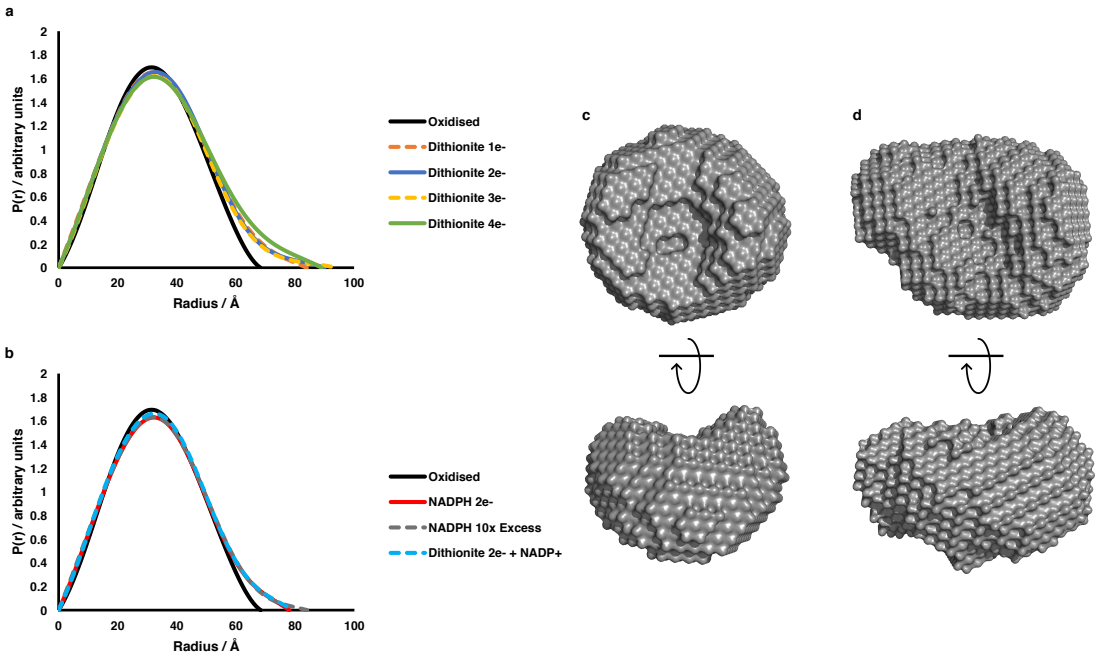

Figure 4.3: Further analysis of the SANS data collected on CPR in different redox states. (**a** and **b**) The $P(r)$ plots derived from the scattering data. (**c**) An *ab initio* model from the oxidised data. (**d**) an *ab initio* model from the dithionite 2-electron reduced data.

the data. The models were generated by specifying a flexible region, in this case the 'hinge' residues linking the FMN-binding to the rest of CPR (specifically residues G240, E241, E242, S243, S244 and I245), and proceeding to calculate the theoretical SANS curves for these models using the software CRYSON [115].

Figure 4.4 (a-c) shows that the ensemble present in the scattering curve is best described by a two state model selected from a large pool of conformations since going beyond this to more states provides no clear benefit to the quality of the fit. Following this, an effort was made to fit the data to specific structural models where the compact state was represented by the crystal structure of soluble (N-truncated) human CPR [2] with a calculated R_g value of 24.88 Å (CRYSON). To represent a more extended state, two models were selected: (i) from Huang *et al.* based on NMR and SAXS of wild-type CPR, and (ii) from Hamdane *et al.* which is a crystal structure of the ΔTGEE mutant of CPR with a deletion in the flexible hinge. Molecule A in the ΔTGEE crystal structure was selected which has the FMN domain rotated away from the FAD and linker domains and yields a calculated R_g value of 26.91 Å. Analysis using either of these models for the extended state, while allowing the rations of compact and extended states to vary, gave reasonable fits to all of the scattering curves studied. Examples are shown in Figure 4.4 (d-g).

SANS data from the oxidised enzyme produced a fit to the data in which the

compact model dominates with 90% existing in the closed conformation regardless of which model is selected to represent an extended conformation. If this search is extended to 10,000 different structures the fit is still 94% of a compact conformation. The curve for the oxidised enzyme has an excellent fit to the theoretical SANS curve for the closed crystal structure (calcualted R_g of 24.70) alone giving a χ^2 value of 1.87. Table 4.2 summarises the proportions in each state for two different models as well as the goodness of fit values.

Sample	Two-state Models					
	Crystal + Huang *et al.* model			Crystal + ΔTGEE mutant model		
	$f_{compact}$	$f_{extended}$	χ^2	$f_{compact}$	$f_{extended}$	χ^2
Oxidised	0.90	0.10	1.64	0.90	0.10	1.75
Dithionite $1e^-$	0.67	0.33	3.12	0.48	0.52	1.99
Dithionite $2e^-$	0.61	0.39	3.27	0.56	0.44	1.81
Dithionite $3e^-$	0.69	0.31	2.25	0.59	0.41	1.87
Dithionite $4e^-$	0.66	0.34	2.64	0.54	0.46	2.03
Dithionite $2e^-$ + $NADP^+$	0.70	0.30	2.55	0.59	0.41	2.21
NADPH 1 equiv. ($2e^-$)	0.69	0.31	2.74	0.55	0.45	1.99
NADPH excess	0.66	0.34	3.07	0.47	0.53	1.60

Table 4.2: Analysis of CPR SANS redox data in terms of two-state models. The models used to analyse the scattering data in terms of a two-state equilibrium are described in the text. In both cases the compact state is described by the crystal structure of oxidised CPR [2]; the extended structure is described *either* by the model of Huang *et al.* [40] or by the structure of the ΔTGEE mutant [60]. The goodness-of-fit to the scattering curve is given by the χ^2 statistic.

Analysis of the SANS data in terms of these two-state models shows that the increase in R_g and D_{max} on reduction can be accounted for in terms of an increase in the population of molecules in more extended state. This is present in all of the reduced states studies with some substantial differences between them. In the dithionite $2e^-$ reduced state ca. 40% of the molecule is calculated to be in the extended conformation. This is true whichever model is used for the extended state though the model of Hamdane *et al.* [60] gives a better fit to the scattering curve at high Q-values, however the resolution of the SANS data does not allow definite differentiation between the two models. The high Q-values describe the smaller details of the model such as individual domain orientation and so this may suggest that the FMN domain is oriented differently, for example since the experimental intensity is less steep than the model intensity at high Q-values (Figure 4.4 e and g) it could suggest that the FMN domain is not as far out as the Huang *et al.* model may suggest. Reduction to the same level using NADPH rather than dithionite has a less significant effect when describing the extended state using the Huang *et al.* model but not when using that of Hamdane *et al.*.

4.2.2 Effects of Ionic Strength on Domain Motion and Catalysis

In addition to studying the effect of redox state, the ionic strength of the buffer was also controlled. An increase in the ionic strength affects the rate of the CPR catalysed reduction of P450s or of cytochrome *c* [40, 116, 30, 117], leading to an increase in catalytic rate, k_{cat} and in the Michaelis-Menten constant K_{M}, for cyt *c*. Kinetic traces from rapid mixing experiments of pre-reduced CPR in an excess of NADPH, and cyt *c* have already been shown to feature a very rapid burst phase upon initial mixing followed by a slower steady state phase [71]. The rapid burst phase is a result of the pre-reduced CPR being predominantly in an open conformation that is ready to react immediately upon binding to cytochrome *c*. Once these initial reduced molecules have reacted they must then interact with NADPH again and undergo domain reorganisation to carry out the necessary intramolecular electron transfers; therefore the domain motions begin to limit the rate of reaction which is reflected in the transition to a slower catalytic rate.

Figure 4.5a shows kinetic traces of cyt *c* reduction at different salt concentrations; the initial burst phase followed by a transition to a slower steady-state phase limited by domain motions and additional electron transfer steps is clearly present. At low salt, 21% reduction of cytochrome *c* takes place within the 2 ms dead-time of the instrument, and this is in reasonable agreement with the analysis of the SANS results obtained in the presence of excess NADPH using the model of Huang *et al.* for the

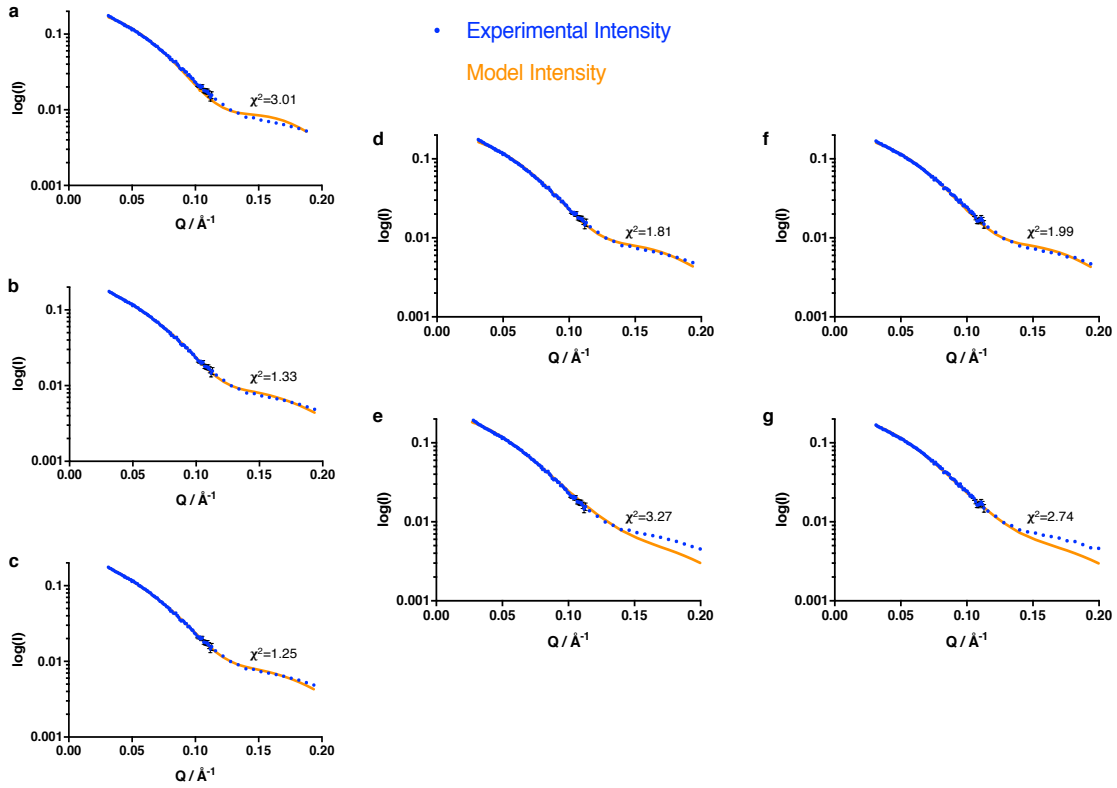

Figure 4.4: Analysis of SANS data in terms of multiple states. (**a-c**) Fits to the scattering curve for CPR reduced to the $2e^-$ level with dithionite using one, two or three states (from a 10,000 conformation pool) respectively. Fits to the scattering curve for CPR reduced to the $2e^-$ level with dithionite using a two-state model; the extended state was represented by, (**d**) the model of Hamdane *et al.* or, (**e**) the model of Huang *et al.*; in both cases the crystal structure was used as a model for the compact state. Fits to the scattering curve for CPR reduced to the $2e^-$ level with NADPH using a two-state model; the extended state was represented by, (**f**) the model of Hamdane *et al.* or, (**g**) the model of Huang *et al.*; in both cases the crystal structure was used as a model for the compact state. In all cases the goodness-of-fit is indicated by the χ^2 value.

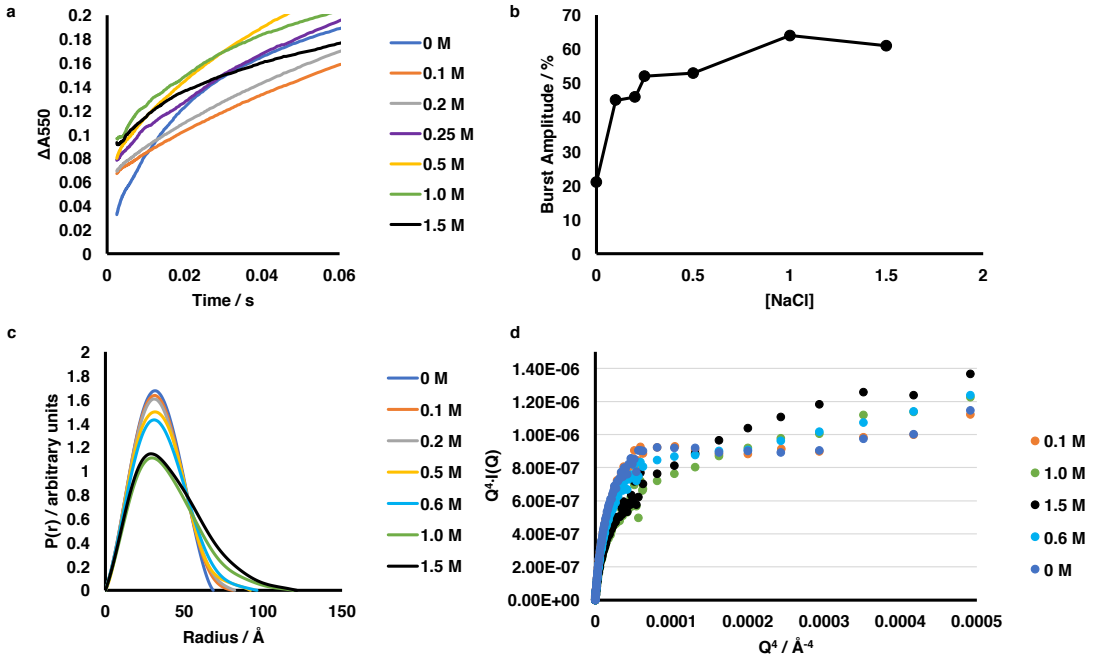

Figure 4.5: Further analysis of the SANS data collected on CPR at different ionic strength. (**a**) Stopped-flow traces showing the reduction of cyt *c* on rapid mixing of CPR pre-reduced with NADPH and cytochrome *c*, at various concentrations of added salt; the percentage of a single turnover which occurred within the 2 ms deadtime of the instrument is plotted as a function of NaCl concentration in (**b**). (**c**) Pairwise distance distribution functions derived from the SANS data at different salt concentrations, showing that increasing the salt concentration leads to a more extended conformation, in qualitative agreement with SAXS studies [40, 117]. (**d**) Porod-Debye plots, showing increased flexibility of CPR at ≥ 0.6 mol dm^{-3} NaCl.

extended conformation (Table 4.2). As the salt concentration is increased, there is a clear increase in the fraction of the first turnover of reduction taking place in the burst phase. On addition of 0.1 M NaCl there is an increase in the fraction of the reduction taking place in the dead time to approximately 45%. This continues to increase up to a maximum of around 60% with 1.0 M NaCl. With 1.5 M NaCl there was a slight decrease which is likely due to a detrimental effect caused by excessive salt which is known to cause unfolding in proteins when present in high concentrations. At approximately 50 ms after mixing the rate of cyt *c* reduction decreases to the steady-state rate, which is also clearly affected by added salt, first increasing as the salt concentration is increased, reaching a maximum at 0.5 M NaCl and then decreasing as the salt concentration is further increased, this is in agreement with earlier data [117]. This trend in observed k_{obs} is illustrated in Figure 4.6.

The SANS data obtained under conditions of defined redox state show how

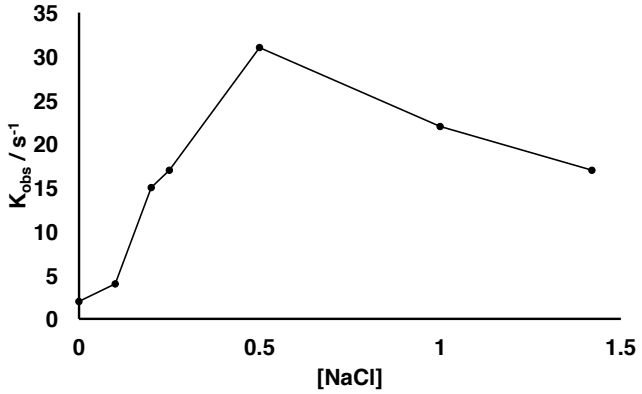

Figure 4.6: Plot of k_{obs} of cytochrome c turnover by CPR at different salt concentrations.

R_g and D_{max} increase with increasing salt concentration (Table 4.3). A gradual increase is seen up to 0.5 M NaCl with a marked increase thereafter. Porod-Debye plots [118, 97] of the scattering data shown in Figure 4 (d) reveals that there is an increase in the flexibility of CPR upon addition of salt and then beyond 0.5 M NaCl the curve begins to take on a shape indicating an extremely flexible/unfolding protein where no plateau is seen after the initial steep curve.

Added NaCl (M)	Size Parameters	
	R_g (Å)	D_{max} (Å)
0	24.7 ± 0.1	71
0.1	27.6 ± 0.1	80
0.2	28.6 ± 0.2	81
0.5	27.6 ± 0.1	91
0.6	27.6 ± 0.2	96
1.0	26.8 ± 03	119
1.5	27.1 ± 0.4	121

Table 4.3: Size Parameters derived from SANS data for CPR with varying salt concentrations in the buffer solution. Showing radii of gyration (R_g) and maximum dimensions (D_{max}). All D_{max} values, determined from $P(r)$ plots using GNOM in Primus as part of the ATSAS suite, were rated as "good" (0.8) fits or better. All errors <2 Å.

Rigid-Body Modelling

As a result of the potentially unfolded nature of the protein at high salt concentrations the rigid-body modelling for this dataset was limited to the 0-0.5 M range. The data were analysed in terms of two-state equilibrium as with the redox state data. The fitting parameters are given in the caption of Table 4.4; the proportion of the extended conformation increases with salt concentration within this range and again

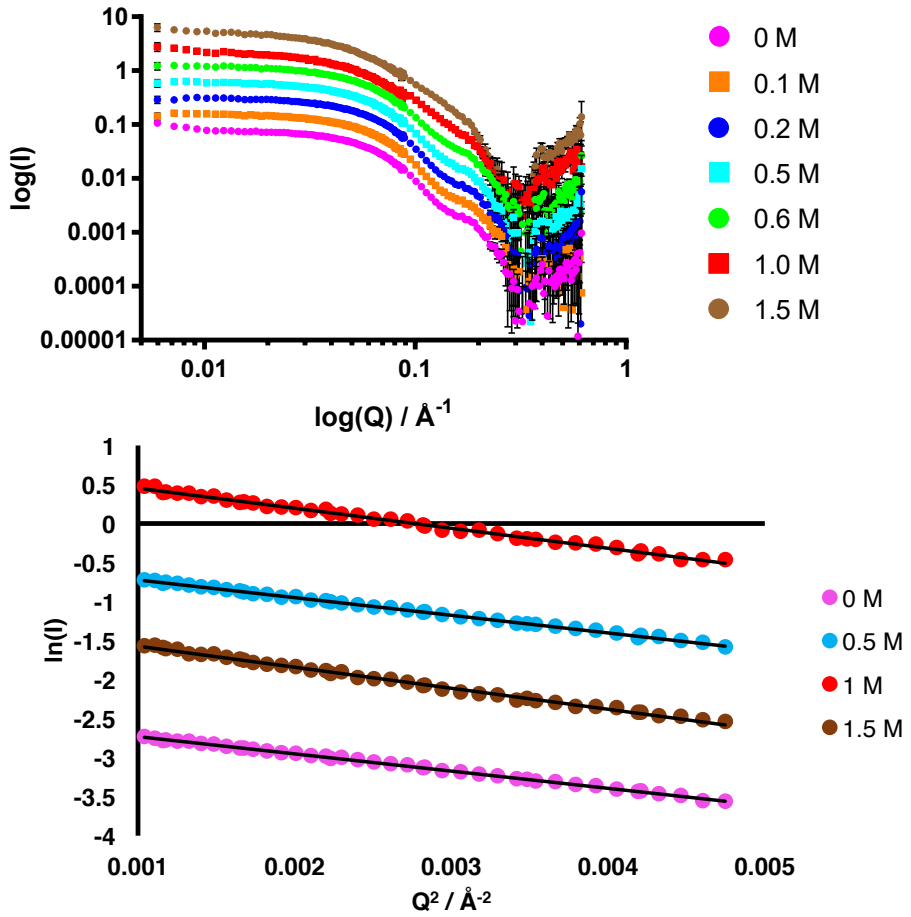

Figure 4.7: SANS Curves and Guinier plots from CPR at different ionic strengths arbitrarily displaced along the vertical axis for clarity. The upper plot shows the SANS curves and the lower plots shows a selection of Guinier plots to demonstrate linearity. Samples were measured at a concentration of 3 mg mL^{-1} in 100 mM BES pD 7.0 at 10 °C (100% D_2O buffer).

both models for the extended state give essentially the same results. Thus the SANS data show that the proportion of the extended conformation increases with increasing ionic strength and comparison with the stopped-flow kinetics data suggests that this conformation has a higher affinity for cytochrome *c* reduction than does the compact conformation. These results also suggest that ionic interactions are important in the stability of the protein especially in maintaining certain conformations since these are clearly disturbed upon alteration of the salt concentration.

Added NaCl (M)	Two-state Models					
	Crystal + Huang *et al.* model			Crystal + ΔTGEE mutant model		
	$f_{compact}$	$f_{extended}$	χ^2	$f_{compact}$	$f_{extended}$	χ^2
0	0.90	0.10	1.64	0.90	0.10	1.75
0.1	0.86	0.14	2.27	0.84	0.16	2.37
0.2	0.85	0.15	2.24	0.85	0.15	2.38
0.5	0.72	0.28	2.12	0.72	0.28	2.52
0.6	N/A	N/A	N/A	N/A	N/A	N/A
1.0	N/A	N/A	N/A	N/A	N/A	N/A
1.5	N/A	N/A	N/A	N/A	N/A	N/A

Table 4.4: MultiFoXS analysis of CPR SANS data at different salt concentrations in terms of two-state models. The models used to analyse the scattering data in terms of a two-state equilibrium are described in the text. In both cases the compact state is described by the crystal structure of oxidised CPR; the extended structure is described *either* by the model of Huang *et al.* or by the structure of the ΔTGEE mutant. The goodness-of-fit to the scattering curve is given by the χ^2 statistic. Thee two-state models were not used to analyse the data for >0.5 M added salt (see text).

4.3 Discussion

4.3.1 The Nature of the Conformational Equilibrium

The data presented in this chapter have been analysed for CPR in terms of a two-state system in equilibrium between a compact and an extended conformation. Deconvolution of the data into a two-state system provides a way to clearly quantify the effects of changing redox state and conditions and allow discussion of the importance of domain movement in CPR.

The crystal structures of wild-type rat, yeast and human CPR [15, 2, 57] all reveal a compact conformation with the isoalloxazine rings of the flavins positioned in such a way to facilitate inter-flavin ET. The crystal structure of the human enzyme fits to the SANS data for the oxidised enzyme well, although the data is fit better if around 10% of an extended structure is included. Compatible with the SANS data is research from Vincent *et al.* that concluded with NMR experiments that CPR exists 95% in a compact conformation when oxidised [119].

Two possible structures have been shown to be able to account for the SANS data within the framework of a two-state system. This may be a result of the low resolution provided by SANS data or the fact that CPR may exist in more than one possible extended state and therefore the curve represents and average of this. Both of the models are consistent with an experiment that shows the abolition of inter-domain salt bridges leads to an increase in the population of an extended conformation [40]. Hedison *et al.* propose that the oxidised form of the enzyme is predominantly in the extended conformation and that coenzyme binding and ET lead to successively greater proportions in the compact form [14]. This is not consistent with the SANS data presented here which shows that the oxidised form is almost entirely in a compact conformation which is supported by NMR and mass spectrometry data [119, 112]. A study by Kovrigina *et al.* has studied domain movement using FRET and two dye-labelled cysteine residues which agrees with the SANS data that oxidised CPR exists in a predominantly closed conformation [120]. The current data are mostly in favour of an extended state that resembled that of the Huang *et al.* model however it should be made clear that SANS data fit slightly better to the ΔTGEE mutant model which itself is able to form a complex with heme oxygenase [72].

4.3.2 Relation to the Catalytic Cycle

The catalytic cycle of CPR for an *in vitro* reaction starting with the fully oxidised enzyme is shown in Figure 4.8; NADPH binds to the FAD domain where it transfers a hydride ion to the N5 of FAD, followed by ET from FAD to FMN to yield a

quasi-equilibrium distribution of $2e^-$ reduced species. Analysis of equilibrium redox titration data [37] led to an estimate of [FAD−$FMNH_2$]/[FAD•−FMN•] = ca. 11, with only a small amount of $FADH_2$−FMN. Intermolecular ET to cytochrome *c* takes place from $FMNH_2$ [3], and then probably from FMN• [22]. This represents a 0-2-1-0 cycle of redox states (in terms of numbers of electrons). It has been suggested that *in vivo* the 'resting state' of CPR is a $1e^-$ reduced (FAD−FMN•) state, reduction by NADPH leading to a $3e^-$ reduced state and ET to cytochrome P450 taking place only from $FMNH_2$ – that is a 1-3-2-1 redox cycle [3]. An unambiguous choice between these two cycles cannot yet be made.

SANS allows relation of the results on domain movements to the catalytic cycle secure in the knowledge that the redox state of CPR is well defined in our experiments. The oxidised enzyme is essentially completely in the compact state (K_{eq} ca. 9; Figure 4.8). In the CPR $2e^-$ $NADP^+$ species, the product of the initial hydride transfer, the proportion of the extended state is 30%. The retention of a significant population of the compact state in this species is consistent with the obvious requirement for a conformation with the FAD and FMN in close proximity for interflavin electron transfer. Indeed, relaxation kinetics shows that the rate of interflavin electron transfer increases on binding $NADP^+$ [29, 58]. On the subsequent dissociation of $NADP^+$, the population of the extended state increases to ca. 40%, facilitating electron transfer to cytochrome P450 (or cyt *c*).

It should be noted that the limitation to this approach is the different time scales that each technique is based on. The SANS data were measured at least 24 h after the samples where prepared by which time the species may have changed somewhat from those that are measured in the kinetics measurements. Though the samples were checked spectroscopically before and after measurement the concentrations were very low and the cuvettes narrow. It has been observed that the reduced species changes over long time periods as evidenced in Chapter 3, Figure 3.7. So although these species may be indicative of various steps in the catalytic cycle, the long time scales of preparation and measurement mean that the conclusions should be used as a guide to more high resolution (temporal and structural) work, rather than an absolute answer. A potential way to avoid this would be a double-mixing stopped-flow system, ideally in an oxygen free or degassed environment attached directly to a SANS/SAXS diffractometer. This type of experimental setup is discussed further in Chapter 6.

4.3.3 Structural Triggers for Domain Movement

The interaction between the FMN and FAD/linker domains in CPR is weak; no interactions between the isolated FMN and FAD/linker domains are detected ki-

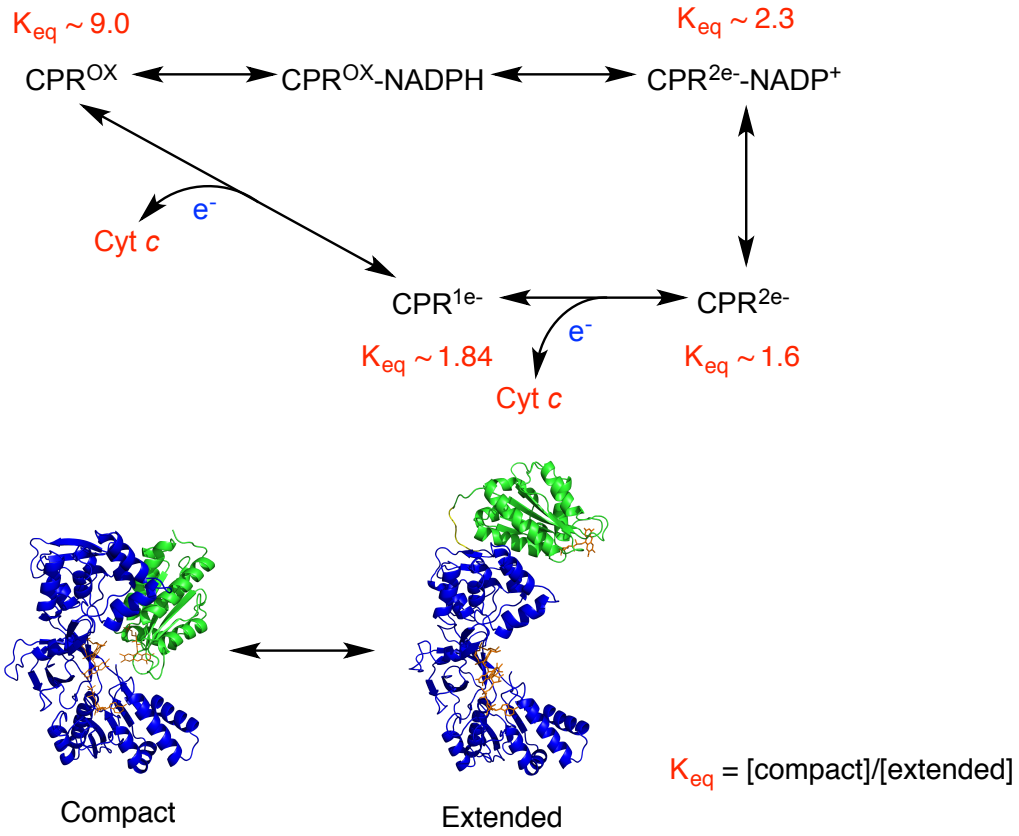

Figure 4.8: Updated catalytic cycle of CPR showing the position of the conformational equilibrium for each intermediate. The reaction shown is cytochrome *c* reduction *in vitro* as discussed in the text. For illustrative purposes, the compact state is represented by the crystal structure of the oxidised enzyme, and the extended conformation by the model of Huang *et al.* where the FAD-binding and linker domain are coloured blue and the FMN-binding domain is in green.

netically, spectroscopically, or by ITC [28, 110] and the redox potentials of the separated domains are essentially the same as those of the intact enzyme. Thus only small changes in interactions across the interface would be required to perturb the conformational equilibrium.

In CPR FMN N5 is positioned so that it might form a hydrogen bond to the peptide NH of G144 when the flavin is oxidized and to the carbonyl of this residue when the flavin is protonated in the reduced states. A reorientation of this peptide bond would thus be required on formation of the neutral semiquinone and protonation at N5. There is good evidence for this in structures of flavodoxins [121, 122] and in the recent comparison of the structures of oxidised and reduced rat CPR with 2'-AMP bound [36]. This 'peptide flip' is accompanied by changes in the neighbouring residues, notably Y143 and E145, the latter being in the inter-domain interface. Although the enzyme was reduced in preformed crystals, possibly inhibiting domain movement, there is a clear change in the relative position of the domains on reduction in one of the two molecules in the asymmetric unit.

Coenzyme binding appears to be a two-step process [42, 36]: First the 2'5'-ADP part binds, then - associated with a displacement of W679 which is stacked against the isoalloxazine ring of FAD - the nicotinamide moves into place next to the FAD. In the structure of the W679/S680 deletion mutant [41] there is a disordered FMN domain in one molecule of the asymmetric unit, suggesting involvement of these residues in determining the relative orientation of the domains. Indeed, in the structure of the human enzyme there are water-mediated hydrogen-bonds between the Cβ-OH of S680 and N178 and D212 in the FMN domain (Figure 4.9) [2]. There is a hydrogen bond between the backbone of W679 and that of D634, in a flexible loop comprising residues G633-N637; R636 in this loop hydrogen-bonds to T180 in the FMN domain. This loop is close to the adenine ring of the bound coenzyme, and in the structures of the disulphide cross-linked mutant it moves on $NADP^+$ binding; mutagenesis studies support a role for this loop in coenzyme binding and flavin reduction. It is thus likely that a concerted movement of W679/S680 and the G633-N637 loop on coenzyme binding will affect the domain interface and alter the equilibrium between the compact and extended states.

It is perhaps most conceivable that cofactor binding is the primary initiator of domain motion or unlocking of the conformational flexibility of the protein. This could be tested further using $NADPH_4$ (requires a short synthesis procedure) which binds to the enzyme exactly as NADPH does but is redox inactive.

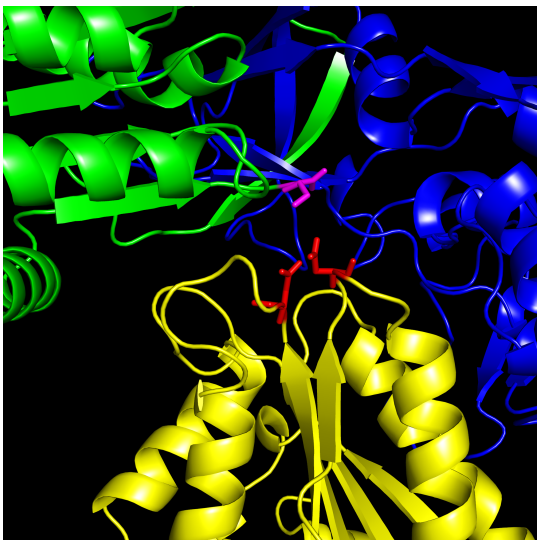

Figure 4.9: A close-up of the compact crystal structure of CPR illustrating the proximity of S680 to N178 and D212. S680 is shown as sticks (**purple**) as part of the FMN-binding domain (**green**) whilst N178 and D212 are shown as sticks (**red**) in the FMN-binding domain (**yellow**). The linker domain is show in **blue**.

4.4 Conclusion

In CPR, it is clear that protein dynamics, and specifically domain motions, are involved in ensuring productive electronic coupling between the flavin cofactors and between them and the electron acceptor protein. The conformational search required to reach these productive configurations can limit the rate of ET. It can be shown that in the case of CPR this search can be adequately described by a two-state equilibrium. For the first time, the conformational equilibrium has been related directly to the catalytic cycle, showing its position in key intermediate steps.

Chapter 5

A Structure of the CPR-Cytochrome *c* Complex in Solution

Complexes between electron transfer proteins require, on the one hand, sufficient specificity of the interaction to allow for rapid and selective electron transfer, and, on the other hand, a fast turnover of the complex. The complexes formed by these proteins are therefore often relatively weak and transient [123, 124]. This generally makes the complexes difficult to crystallize, although some such transient complexes have successfully been studied by NMR [125, 126, 127, 128, 129].

The interaction between CPR and cytochrome *c* (cyt *c*) is one that has long been exploited; CPR was originally characterised in the 1950s as a cyt*c* reductase before it was discovered to be the electron transfer partner of cytochromes P450 [130, 9]. In the liver endoplasmic reticulum, cytochrome P450s are present in excess over CPR, with a molar ratio of cytochrome P450:CPR as high as 20:1, so that electron transfer must occur in transient complexes, whose lifetime has been estimated at 200 ms [131]. As discussed in the introduction in Section 1.1, the two electrons are donated one at a time at two distinct steps in the cytochrome P450 reaction cycle [132, 22], and it is possible that the complex dissociates between these two electron transfer steps [131]. The most common use of this interaction is in the form of cyt *c* reduction assays to test the catalytic activity of CPR in solution [13]. The primary reason for the use of cyt *c* as a surrogate electron acceptor is because CPR will not catalyse the reduction of P450s in solution, only when both enzymes are membrane bound.

While cyt *c* is unlikely to be a physiological redox partner of CPR, the electron transfer reaction between CPR and cyt *c* has continued to be widely used as a standard model to characterize the activity of CPR and it is likely that the binding

sites on CPR for cyt *c* and cytochrome P450 are at least substantially overlapping [133, 134]. Recently, Waskell and Ramamoorthy *et al.* [38] have used NMR techniques together with molecular docking to study complex formation between cyt *c* and the isolated FMN-binding domain of CPR, revealing two possible relative orientations of the proteins in the complex. In the work presented in this chapter, SANS is used to determine the low-resolution structure of the complex between cyt *c* and CPR lacking only the N-terminal membrane-binding sequence; to facilitate this, the K75E/R78E/R108Q mutant of CPR is used, which has a substantially lower K_{M} for cyt *c* than does the wild-type enzyme [40]. Additionally, the powerful capabilities of deuteration and contrast matching in SANS to study the protein-protein complex will be employed.

5.1 Sample Preparation

Deuterated CPR was prepared as described in Appendix A2.2 in the D-lab at the ILL in Grenoble, with substantial support provided by Dr. Juliette Devos. The protein was deuterated to a match-out percentage of 85% to allow both components of the complex to be measured individually whilst both existing in a complex in solution.

5.1.1 Contrast Match Point Determination

Before match-out measurements can be made the point at which each protein contributes the same amount of coherent scattering as the buffer solution must be determined. At this precise point the sample is experimentally invisible and no longer contributes to the scattering intensity and is subtracted along with the buffer. Samples of deuterated CPR (d-CPR) and cyt *c* were prepared with different percentages of D_2O present in the buffer solution and then measurements taken until the forward scattering intensity (I(Q=0)) became zero. This is illustrated in Figure 5.1 where the different D_2O contents yield different I(0) values which produce a linear plot. The point at which the line crosses the horizontal axis is the match-out point which was also confirmed experimentally.

5.2 Results

5.2.1 Characterisation of CPR K75E/R78E/R108Q

The higher affinity of K75E/R78E/R108Q for cyt *c* had already been established by Huang *et al.* [40], where a 5-fold decrease of the K_{M} and a doubling of the k_{cat}

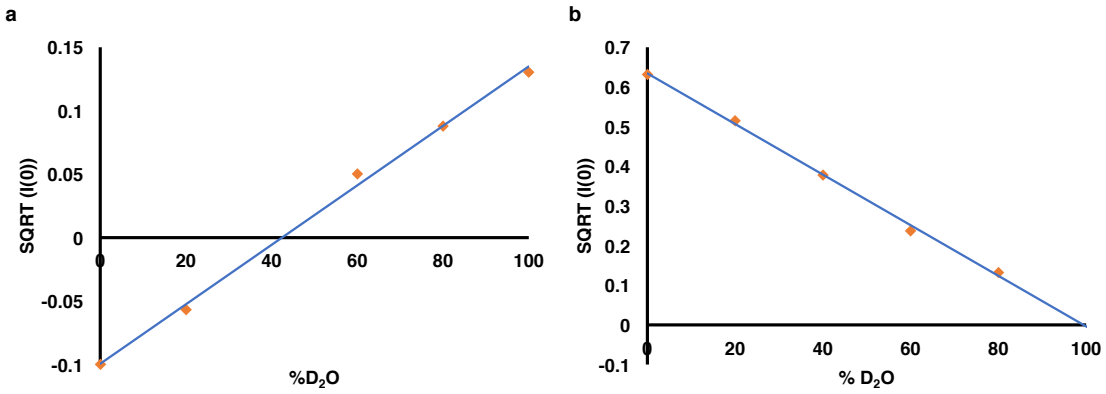

Figure 5.1: Contrast match point determination plots. (**a**) Is for cyt *c* and (**b**) is for deuterated CPR.

for the reduction of cyt *c* was observed. In this mutant two salt bridges believed to stabilise the compact conformation (determined from the X-ray crystal structure) were abolished. Some evidence from SAXS was also presented in this study which suggested the molecule favoured a more open confirmation in solution, though the conclusions from these experiments were partially clouded due to the X-ray induced photoreduction effects that were observed. In this investigation it was established using SANS that this is indeed the case and will be described in more detail in the following section. Utilising the same stopped-flow methodology as described for the previous experimental chapter, the nature of the burst phase kinetics was studied which was first demonstrated by Haque et. al. [**?**]. It was observed that the mutant had significantly more of the burst phase missing (80%) within the deadtime of the instrument than the wild-type (20%) which suggested that more of the molecule was present in the open conformation when reduced and ready to react immediately upon mixing. Figure 5.2 shows a kinetics trace from this experiment, where approximately twice as much of the burst phase is missing in the mutant compared to the wild-type, and almost the entire first turnover of the cyt *c* in the reaction is completed.

The first SANS curves to be collected were of the mutant alone in solution in order to further confirm a greater presence of an extended conformation. These are shown in Figure 5.3 along with the wild-type protein and cyt *c* alone in solution. The size parameters derived from these curves can be found in Table 5.1. The R_g and D_{max} values for the mutant CPR alone in solution are at least 1 Å greater than those that were found for the wild-type here and also those measurements in the preceding chapter. Figure 5.4 shows the *ab initio* scattering envelopes generated using DAMMIF. These along with the size parameters clearly indicate a slightly more extended average structure for the mutant than for the wild-type protein in

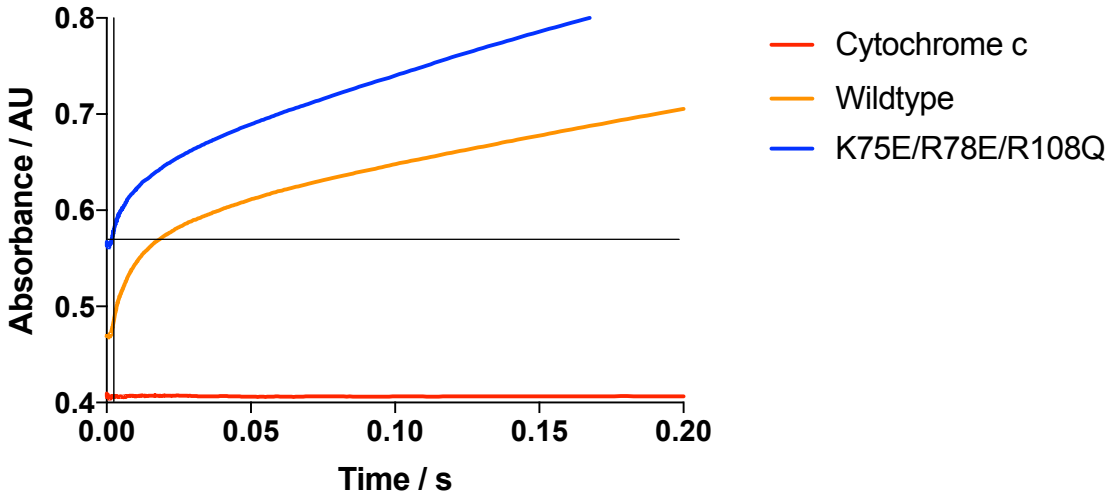

Figure 5.2: Stopped-flow burst kinetics of wild-type CPR (**orange**) and K75E/R78E/R108Q (**blue**), with the cyt *c* baseline (**red**) also shown. The horizontal black line on the plot represents the absorbance at which the first turnover of cyt *c* is completed. The assay was carried out in 100 mM BES pH 7.0 buffer and the methodology was as described in the experimental section of the appendix. The dead time of the instrument was 2 ms. Saturating cytochrome *c* concentrations were used to remove the kinetic dependence on this substrate and produce pseudo first-order conditions.

the oxidised state, with a visible 'cleft' resolved in the mutant envelope which was highly repeatable in envelope generation. For the wild-type model the compact crystal structure [2] was superimposed and for the mutant (for which there is no crystal structure available) a single best fit model from MultiFoXS [114] rigid body modelling was selected from a pool of 10,000 structures.

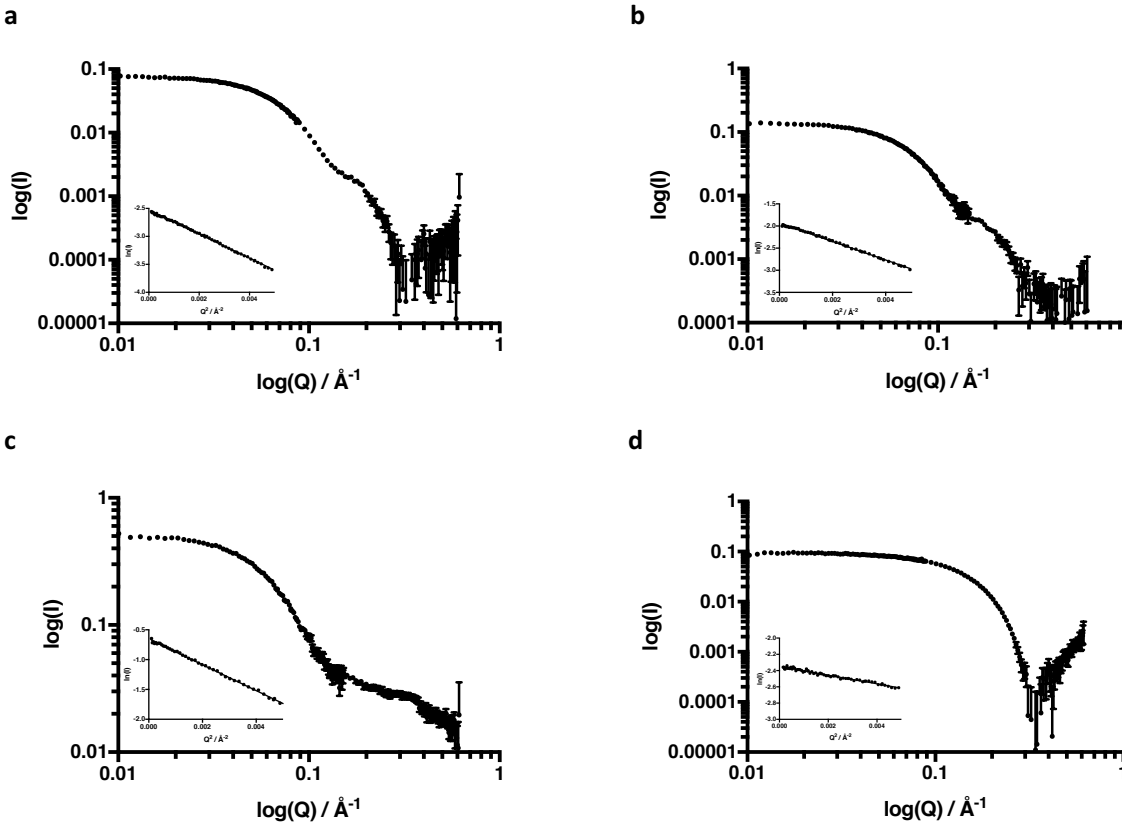

Figure 5.3: CPR and cyt *c* scattering curves. (**a**) Wild-type CPR, (**b**) h-CPR K75E/R78E/R108Q, (**c**) d-CPR K75E/R78E/R108Q and (**d**) cyt *c*. Guinier plots are shown as insets. Conditions were 15 °C, 100 mmol dm^{-3} BES pH 7.0 buffer made up with either D_2O (for hydrogenated protein) or H_2O (deuterated protein) as appropriate.

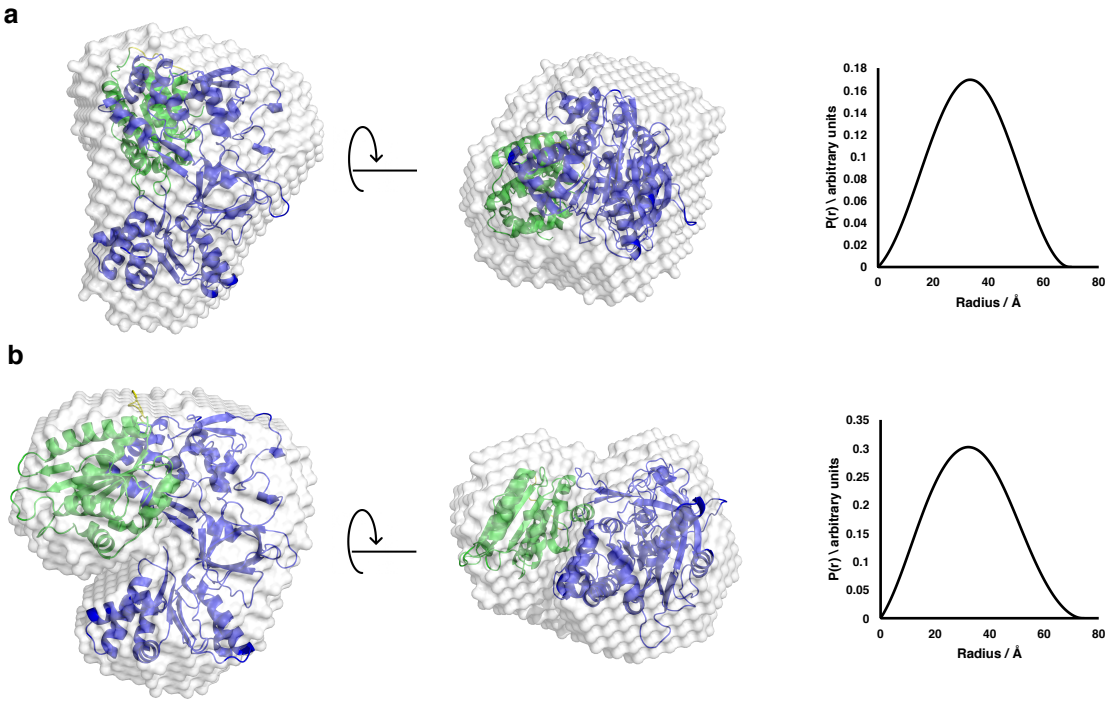

Figure 5.4: *Ab initio* scattering envelopes and $P(r)$ plots from wild-type and mutant CPR SANS data. Where (a) is the wild-type and (b) is K75E/R78E/R108Q mutant. Both envelopes have an atomic resolution model superimposed, for (a) it is the crystal structure of the compact conformation [2] and in (b) it is the single best fit model selected by MultiFoXS [114] where the FAD-binding and linker domain are coloured blue and the FMN-binding domain is in green. The models are rotated 90°about the axis as indicated by the arrow.

Sample	Size Parameters	
	R_g (Å)	D_{max} (Å)
Wildtype	24.7 ± 0.1	71
K75E/R78E/R108Q mutant	25.5 ± 0.2	73

Table 5.1: Size parameters derived from the SANS data for the wild-type and K75E/R78E/R108Q mutant CPR. Showing radii of gyration (R_g) and maximum dimensions (D_{max}). Errors were in the range of ± 1-2 Å for D_{max} values and were rated as 'good' fits using GNOM in Primus (part of the ATSAS suite, see Appendix A.5.1.).

Sample	Two-state Models					
	Crystal + Huang *et al.* model			Crystal + ΔTGEE mutant model		
	$f_{compact}$	$f_{extended}$	χ^2	$f_{compact}$	$f_{extended}$	χ^2
Wildtype	1.00	0.00	1.27	1.00	0.00	1.25
K75E/R78E/R108Q mutant	0.84	0.16	1.82	0.67	0.33	1.20

Table 5.2: Analysis of CPR wild-type and K75E/R78E/R108Q mutant CPR in terms of two-state models. The models used to analyse the scattering data in terms of a two-state equilibrium are described in the text. In both cases the compact state is described by the crystal structure of oxidised CPR [2]; the extended structure is described *either* by the model of Huang *et al.* [40] or by the structure of the ΔTGEE mutant [60]. The goodness-of-fit to the scattering curve is given by the χ^2 statistic.

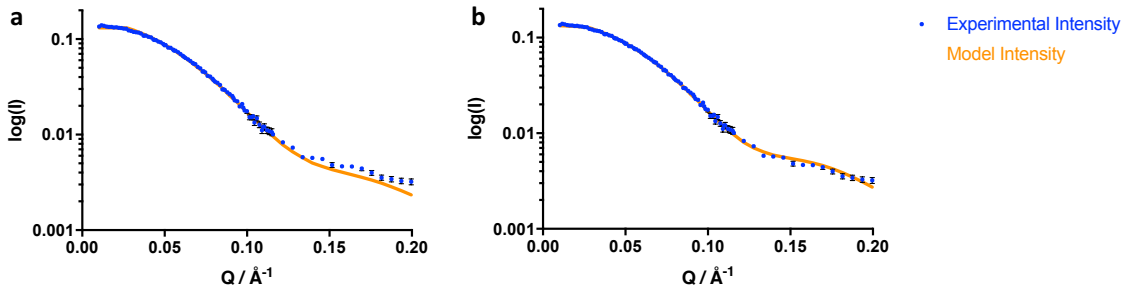

Figure 5.5: 2-State MultiFoXS fits of CPR K75E/R78E/R108Q to (a) the Huang *et al.* model and (b) the ΔTGEE model. The goodness of fit for these models is presented in Table 5.2.

In view of the evidence that CPR exists as an equilibrium between a compact and an extended conformation the data were analysed using MultiFoXS in the manner described in the preceding chapter. Briefly, the crystal structure [2] was used to describe the compact conformation and either the Huang *et al.* [40] or ΔTGEE model [60] was used to represent the extended state. Analysis using either of these models for the extended state yielded satisfactory fits ($\chi^2 < 2$) to the scattering curves (Figure 5.5). At larger Q-values, in the wider scattering region, the fit is somewhat better, even by eye, for the ΔTGEE model which may suggest that the smaller details such as the precise position and orientation of the FMN domain may be better reflected by this structure.

For the wild-type enzyme, the scattering curve is fit best by the compact crystal structure with only 10 % of an extended structure. For the mutant, on the other hand, a good fit requires inclusion of a significantly greater proportion of an extended conformation. Either of the two models for the extended state can give a satisfactory fit, although depending on the model chosen, the fraction of the extended conformation can vary from 16% to 33% (Table 5.2). We conclude, therefore, that the abolition in the mutant CPR of two salt bridges stabilising the compact conformation does indeed lead to an increase in the proportion of the extended, cyt *c* reactive conformation, and that this in turn leads to an increase in the amplitude of the burst phase of the reduction of cyt *c*.

5.2.2 Structure of the Complex Between CPR K74E/R78E/R108Q and Cytochrome *c*

The complex was analysed using SANS and the resulting scattering curves are shown below in Figure 5.6. All curves measured were of suitable statistical quality for further analysis, including *ab initio* modelling. As a result of size exclusion chro-

matography being carried out immediately before sample measurement for further purification and isolation of the complex there was no aggregation present in any of the curves and a very long and clear Guinier region was resolved. The respective Guinier plots of each scattering curve are shown as insets. The only curve of substantially lower statistical quality is that at the d-CPR match out point where only cyt *c* is experimentally visible; the low concentration of cyt *c*, small size of the particle and low contrast led to a noisy curve which nonetheless clearly represented cyt *c*, confirmed by a calculation of the molecular weight from the scattering data. The hydrodynamic parameters and calculated molecular masses derived from these curves are shown in Table 5.3 and the scattering envelopes and respective $P(r)$ plots are shown in Figure 5.7.

Matching out the cyt *c* by carrying out the experiment in 43% D_2O gives a D_{max} value the same as that obtained for the CPR mutant alone, while matching out the CPR mutant in 100% D_2O gives the expected small values for R_g and D_{max} corresponding to cyt *c*. The I(0) values are as expected for the monomeric proteins at their respective concentrations. Comparison of the bead-model *ab initio* envelopes derived from the scattering curves of the full complex and of the cyt *c* matched-out complex allows us to obtain an initial picture of the location of cyt *c* within the complex (Figure 5.7a). Superimposing either atomic resolution models from known crystal structures or hypothetical models on to these envelopes permits visual confirmation of the fit of the data to the molecules in question. The cyt *c* match-out model (Figure 5.7b) was a single best fit model produced using the crystal structure of CPR subjected to a random conformational in MultiFoXS. The CPR matched-out model (Figure 5.7c), revealing only cyt *c*, was produced using the horse heart cyt *c* crystal structure [135].

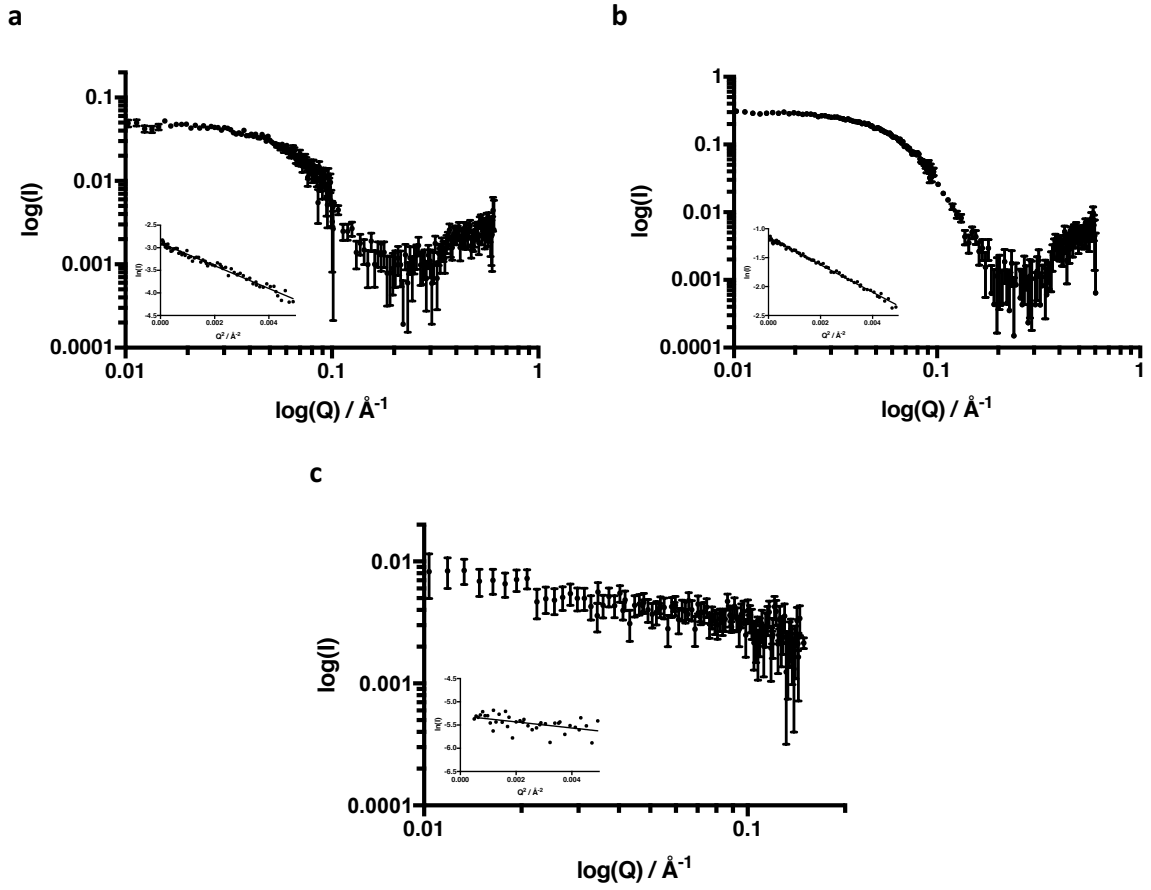

Figure 5.6: CPR-cyt *c* complex scattering curves. (a) The full complex (70% D_2O), (b) cyt *c* match out and (c) d-CPR K75E/R78E/R108Q match out. Conditions were 15 °C, 100 mmol dm^{-3} BES pH 7.0 buffer made up with the appropriate D_2O% to achieve the necessary contrast as indicated in parentheses.

Sample	R_g (Å) (Guinier)	R_g (Å) ($P(r)$)	D_{max} (Å)	I(Q=0)	Calculated M_r (kDa)
d-CPR K75E/R78E/R108Q Mutant Alone	25.2 ± 0.2	25.8	72	0.52 ± 0.0023	73
h-CPR K75E/R78E/R108Q Mutant Alone	25.0 ± 0.2	25.15	72	0.15 ± 0.00078	74
Full Complex (70% D2O)	26.3 ± 0.8	26.9	77	0.05 ± 0.00082	81
Cyt *c* matched out (43% D2O)	26.0 ± 0.3	26.1	72	0.31 ± 0.0018	69
CPR mutant matched out (100% D2O)	11.5 ± 1.1	11.3	38	0.0051 ± 0.0002	12
Cyt *c* alone	12.2 ± 0.1	11.0	35	0.094 ± 0.0003	11

Table 5.3: Size parameters derived from SANS data of CPR mutants and complex data at different match out points. Showing radii of gyration (R_g) and maximum dimensions (D_{max}). Errors were in the range of ± 1-2 Å for D_{max} values and were rated as 'good' fits using GNOM in Primus (part of the ATSAS suite, see appendix section 8.5.1). M_r values were calculated from experimental I(0) values and protein concentrations estimated spectrophotometrically.

5.2.3 Full Complex Rigid-Body Modelling

To obtain a model for the full complex (shown in Figure 5.7a and in more detail in Figure 5.8) the docking software HADDOCK was used together with atomic resolution data available on the interactions of the complex. An increase in ionic strength causes a substantial increase in the K_M of CPR for cyt *c* [40, 136], indicating that electrostatic interactions are likely to be important in the formation of the complex. K13 of cyt *c* can be cross-linked to one of the carboxyl groups from two acidic clusters on the FMN-binding domain of CPR, D207-D208-D209 and E213-E214-D215 and site-directed mutagenesis [137, 138] supports the involvement of the E213-E214-D215 cluster in the interface. Huang *et al.* [38] have recently used changes in NMR chemical shifts to study the interactions between the isolated FMN domain of rat CPR and cyt *c*, leading to two possible models for this complex. Utilising the data from these studies in combination with the SANS data, a model for the complex has been produced using the HADDOCK webserver [139]. A large number of models were initially produced and the model with the lowest docking energies (electrostatics, desolvation, van der Waals and restraints) was chosen as the starting point for further rigid body modelling. This yielded a model where the heme cofactor in cyt *c* was within a distance (<4 Å) of the FMN which would readily allow intermolecular electron transfer. The low-resolution nature of SANS means that the limiting factor in constructing the model is the scattering data; it is clear that a model incorporating both the CPR mutant and cyt *c* fits the data better than one involving the CPR mutant alone.

In the model of the CPR-cyt *c* complex, the FMN-binding domain of CPR and cyt *c* were treated as a single rigid body, so that the contact interface between them was maintained, and only this rigid body, connected to the rest of CPR by the flexible hinge, was allowed to move in the Monte-Carlo conformation search. Conformational optimisation of the starting model was carried out using software from the IMP (Integrative Modelling Platform) suite [140] and the ATSAS suite. A pool of 10,000 conformational samples was created using the RRT (rapidly exploring random tree) sampling tool, which was provided with the starting PDB structure of the complex and a selection of flexible residues (the 'hinge' residues linking the FMN-binding to the rest of CPR, specifically G240, E241, E242, S243, S244 and I245) linking the FMN-binding to the rest of CPR, which residues exactly). Theoretical scattering curves were calculated for each of the sampled conformations using CRYSON [115]. A single best fit model to the experimental data was determined using MultiFoXS [114] in partial mode, where pre-computed scattering intensities were used.

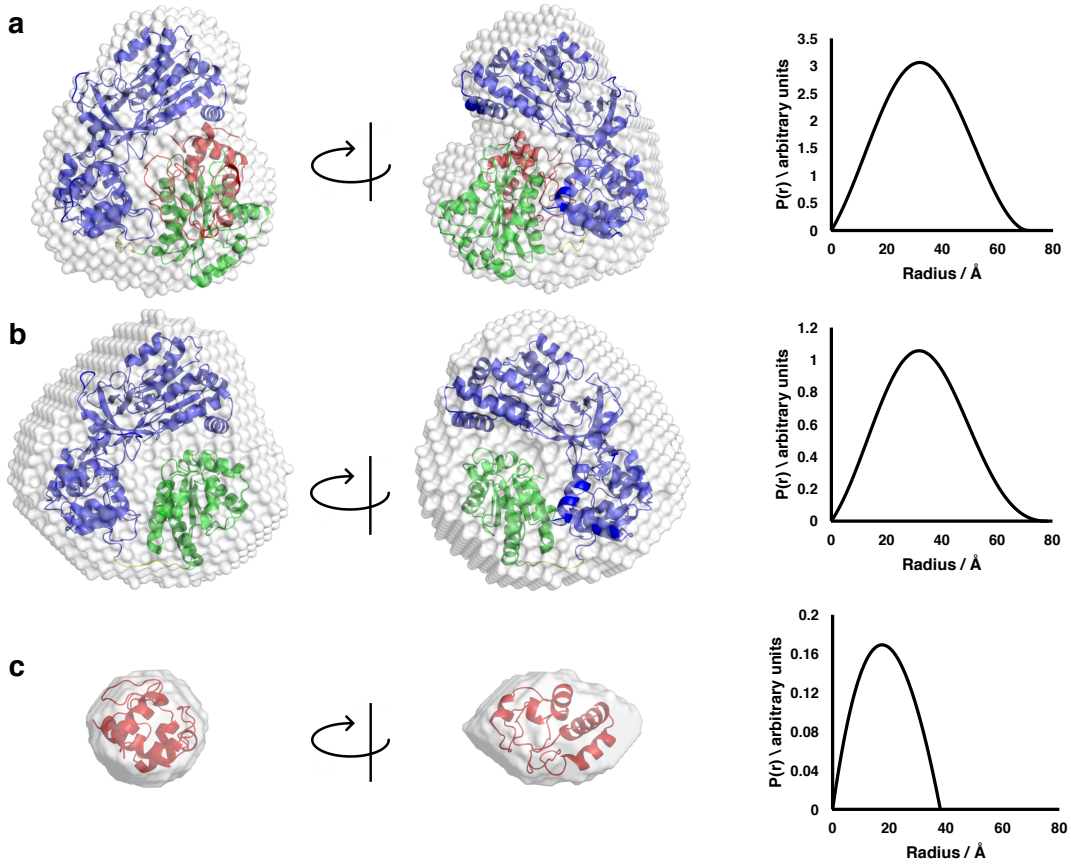

Figure 5.7: *Ab initio* scattering envelopes with superimposed atomic resolution models, and $P(r)$ plots for all complex scattering curves. (**a**) is the full complex, (**b**) is the complex with cyt$c$ matched out and (**c**) is the complex with CPR matched out where the FAD-binding and linker domain are coloured blue, the FMN-binding domain is in green and cyt c is indicated in red. (**a**) and (**b**) are rotated 180° while (**c**) is rotated 90°.

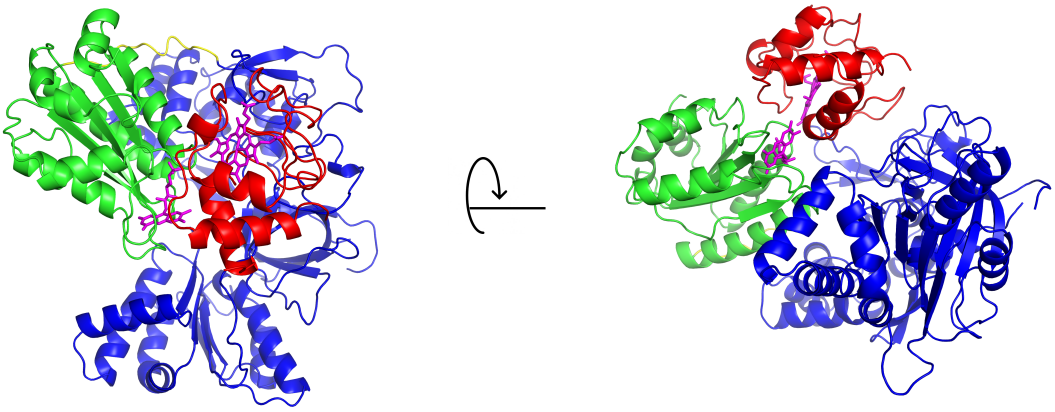

Figure 5.8: Single best-fit model of the CPR-cyt *c* complex where the FAD-binding and linker domain are coloured **blue** and the FMN-binding domain is in **green**. The heme cofactor of cyt *c* and the FMN cofactor of CPR have been included as stick models (**magenta**) to indicate their proximity. The model is rotated 90° about the axis as indicated by the arrow.

5.3 Discussion

A high-resolution structure achieved using X-ray crystallography was published by Sugishima *et al.* [72] of a complex between a CPR mutant and heme oxygenase; it is therefore important to compare this structure with the one proposed in this work since there are a number of notable similarities. The most striking is the compact nature of the complex in both cases. Compared to the model of Huang *et al.* [40] there would have to be significant compaction of the two CPR flavin domains relative to each other in order to adopt the one present in either of the two complex models. Sugishima *et al.* compare the conformation of their CPR to the smallest conformation present in the unit cell of the crystal structure of the ΔTGEE mutant [60] which itself was also used in their complex. A number of interactions between residues in heme oxygenase and domains of CPR besides the FMN-binding domain may contribute to the stability of the complex. This may also be true for cyt *c* though those residues are likely to be different due to the much smaller size of cyt *c* (ca. 12 kDa) compared to heme oxygenase (ca. 30 kDa). The FMN-binding domain and heme oxygenase components of the crystal structure were resolved comparatively poorly to the rest of the CPR molecule, suggesting a level of flexibility and dynamics to this region. This could mean that the precise nature of the complexes formed could vary from molecule to molecule which is not surprising considering the dynamics and flexibility that could be afforded by the structure. This dynamic region led to an overall resolution of 4.3 Å which is relatively low for

a modern X-ray crystal structure determined using synchrotron radiation.

5.4 Conclusion

SANS lacks the resolution and information to be able to resolve the orientation of cyt *c* and the domains of the CPR mutant in the complex in precise atomic detail. However, the model obtained in this work by combining global SANS information and atomic level information (Figure 5.8) indicates a compact structure with extensive inter-domain contacts and a number of significant features. There are several intermolecular polar sidechain-sidechain or sidechain-backbone interactions between cyt *c* (residues 21, 23, 25 and 27) and residues 267, 268, 280 and 359 in the FAD domain of the CPR mutant, showing that the interprotein interface is not limited to the FMN domain of the reductase. The conformation of the CPR mutant in the complex is a relatively extended one, compared to the wildtype crystal structure (Figure 1.3), such that the isoalloxazine rings of the FAD and FMN cofactors are separated by approximately 30 Å. On the other hand, the distance between the FMN isoalloxazine ring and the heme of cyt *c* is <10 Å. This shows that the complex described here is one which is competent for interprotein electron transfer between the FMN and the haem of cyt *c*, but not for intraprotein electron transfer between FAD and FMN, demonstrating that domain movement is required between the intramolecular and the intermolecular electron transfer steps in the CPR mechanism.

Chapter 6

A Time-Resolved Study of the Domain Motions of Cytochome P450 Reductase Using Pump-Probe X-ray Scattering

Up to this point the SAS studies presented have been of static solution samples measured over long periods at multiple detector distances in order to obtain a strong signal to noise ratio and a broad Q-range. However, recording an average of the enzyme in solution provides very little information on the dynamics of the system and no information on the timescale of the changes that take place.

This chapter presents a study using time-resolved SAXS where a stopped-flow system fitted *in situ* to a SAXS beamline to study the shape changes that CPR undergoes with respect to time. This is the first known example of this type of experiment with CPR. Only a radiation synchrotron was able to provide the flux and therefore temporal and spatial resolution needed for SAXS measurements at the necessary time scales. The commissioning of a stopped-flow device to enable rapid mixing on a beamline, as well as protein measurements, are described.

6.1 Time-Resolved X-ray Scattering

In essence, time-resolved X-ray scattering is the capturing of SAXS/WAXS patterns over very short timescale (as low as picoseconds) in order to build up a picture of changes that occur in a molecule over time. These patterns are typically recorded at larger Q-values, the reasons for which will become clear in the description of the instrument.

The basic principle of a pump-probe experiment is to first 'pump' the sample,

with for example a laser, to initiate the reaction in a highly controlled manner followed by a 'probe' which in this case is the X-ray beam. Lasers penetrate the sample and interact with the whole sample almost instantaneously ensuring that the start of the reaction is homogeneous, the wavelength is also highly tunable. Temporal evolution of the reaction is then tracked by adjusting the delay between the laser pulse and X-ray pulse. For most pump-probe experiments 2000 pulses from the synchrotron provide sufficient flux and resolution which arrive 100 ps after the laser. Although lasers are not the only way to initiate the reaction, for the reasons mentioned here they are the most common.

6.1.1 Earlier Work

Historically, pump-probe SAXS has been most heavily used in small-molecule chemistry and solid state physics and very high impact research is now produced in these fields [141, 142, 143]. Over the last few years the technique has been gaining popularity in the study of biological molecules both in solution and in crystalline forms although relatively little work had been published in this field until recently [144, 145, 75, 146, 147, 148].

This is not the first study that has attempted to elucidate the timescales of diflavin reductase function and certainly not the first attempt to use pump-probe measurements. A study published by Heyes *et al.* in 2009 used laser excitation in combination with a chromophore to reduce the flavin cofactors of nitric oxide synthase and follow the subsequent changes using absorbance spectroscopy [149]. The chromophore in question was thiouredopyrene-3,6,8-trisulfonate (TUPS) which was shown in earlier studies to absorb light at around 355 nm and be capable of electron transfer from a photoexcited state to reductase domains of proteins located in close proximity [150, 151]. For this reason, the TUPS molecule must be either covalently bound to the protein structure or mixed in solution in high concentration, both of which were found to be effective. This piece of work concluded that TUPS, coupled with laser excitation, can directly reduce the flavins allowing the subsequent kinetic processes such as interflavin electron transfer to be studied more transparently.

6.1.2 ID09

Insertion Device 09 (ID09), located at the ESRF, is an example of a pump-probe beamline that is designed for the measurement of ultrafast changes in condensed matter. The presence of a high-speed chopper allows extremely short pulses (down to picoseconds) of X-rays to be selected in order to measure very fast changes in the sample. This highly versatile beamline is capable of carrying out the following types of measurement in a time-resolved manner:

- X-ray diffration
- Small-angle X-ray scattering
- Wide-angle X-ray scattering
- Laue diffraction
- Grazing incidence diffraction

When configured for SAXS, the beamline operates on a very similar basic principle to that of a standard SAXS beamline (for example BM29, described in Chapter 2). A diagram showing the basic layout of the beamline is shown in Figure 6.1.

In order to minimise air scattering from the direct beam, this instrument features an helium filled flight tube. Helium, having a much lower scattering cross section than air, will attenuate the beam to a much lower extent, therefore maximising the number of photons which are eventually measured. This, coupled with the extremely high flux of an insertion device beamline is what allows the beamline to be so versatile and carry out measurements with such short exposure times. A set of fast shutters and a rotative chopper are employed to extract X-ray pulses or pulse trains that are suitable for the desired timescales of the dynamic reaction.

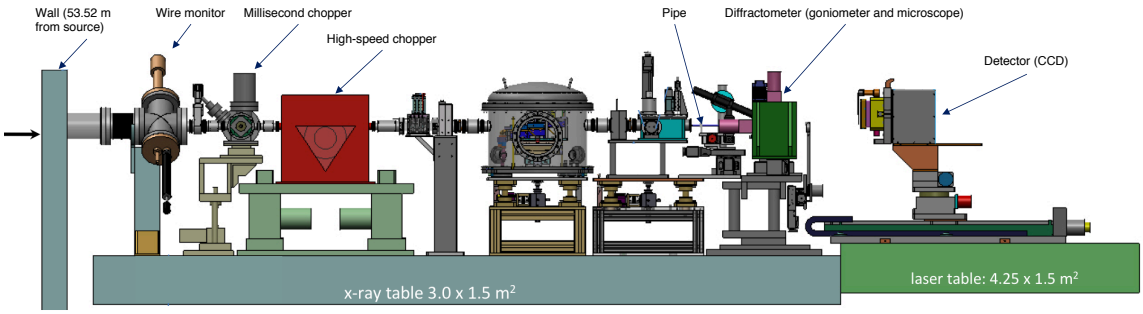

Figure 6.1: Schematic of the ESRF ID09 pump-probe beamline experiment hutch. The direction of the X-ray beam is indicated by the arrow on the left which arrives here after passing through the beamforming elements (shutters, slits, mirrors and monochromator).

6.2 Experimental Setup and Sample Preparation

Before the start of this investigation a brand-new stopped-flow system was installed at the sample position on the beamline which was organised and overseen by Dr. Martin Pedersen, the beamline local contact. In order to demonstrate the functionality of stopped-flow setup and prove the concept is viable for future experiments a number of known reactions were planned to be carried out. Principally, these were the mixing of a solution of CPR with a high ionic strength solution, and the formation of the complex between CPR and cyt *c*. The stopped flow experimental setup for these reactions was, in principle, exactly as described in Chapter 4 and Appendix A.4 with the only major difference being that SAXS/WAXS, rather than absorption spectroscopy was used to probe the changes. Scattering in the WAXS region is substantially weaker but can be very rich in features, the downside of this is that the data can be very hard to interpret at this level, especially when the behaviour of the system at greater levels of detail is unknown. The capillary in the mixing cell of the stopped-flow was carefully aligned with the X-ray beam in order to measure the centre of the capillary at a pint where the solutions were fully mixed. The complex formation was carried out without any reducing agent in order to limit the interactions/shape changes taking place in the mixture, therefore simplifying the interpretation of the data.

A maximum Q-range of 0.02 - 2.75 $Å^{-1}$ was obtained from a sample-to-detector distance of 40 cm. X-ray energy of 18 keV ($\pm$ 5%, pink beam) was selected to give provide a sufficient flux of X-rays. ID09 is capable of a broad energy range; selecting a higher energy would have resulted in harder X-rays resulting in less absorption by the sample and relatively more more elastic scattering, though both decrease in their absolute values. Increasing energy also brings severely reduced flux; the most ideal value for maximum flux would be 12 keV but ID09 is not capable of that, a limitation of the undulator at this beamline (illustrated by Figure B.2 in Appendix B).

6.3 Results

Preliminary SAXS curves were measured on BM29 (described in Chapter 2, Section 2.2), also at the ESRF, in order to show that the samples were not especially susceptible to X-ray radiation damage and were of suitable quality. The curves produced were of a good quality and showed highly monodisperse samples of cyt *c* (Figure 6.2) and CPR (Figure 6.3).

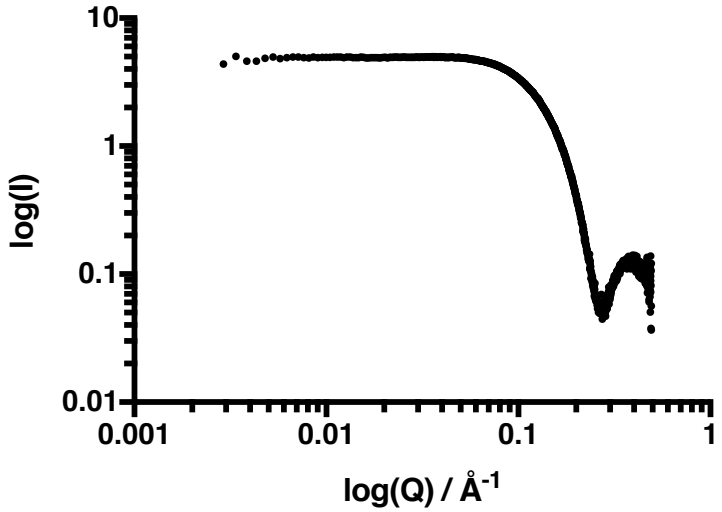

Figure 6.2: SAXS curve of cyt *c* meaured on BM29 at a concentration of 30 mg mL^{-1} with an exposure time of 10 s in 100 mM BES pH 7.0 at 10 °C.

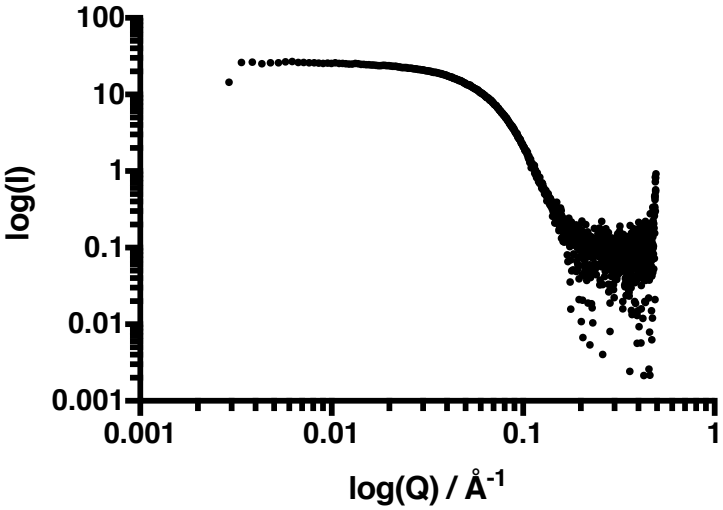

Figure 6.3: SAXS curve of CPR meaured on BM29 at a concentration of 5 mg mL^{-1} with an exposure time of 10 s in 100 mM BES pH 7.0 at 10 °C.

The first measurements taken on ID09 after successfully completing the stopped-flow setup were of cyt *c* alone in solution to check for radiation damage. Figure 6.4 shows successive frames, difference curves relative to the reference scattering pattern at time zero, taken during pulsed exposures where time delays of 0 - 2550 ms were selcted, with intervals of 50 ms. A significant amount of background was present in the low-Q background which led to heavily distorted data in this region. Some changes in the scattering pattern are present, most likely caused by radiation damage in the form of heating the solution by absorption of X-rays. Before the next tests, a new capillary was fitted to the stopped-flow device and realigned to assess whatever was causing the undesirable background.

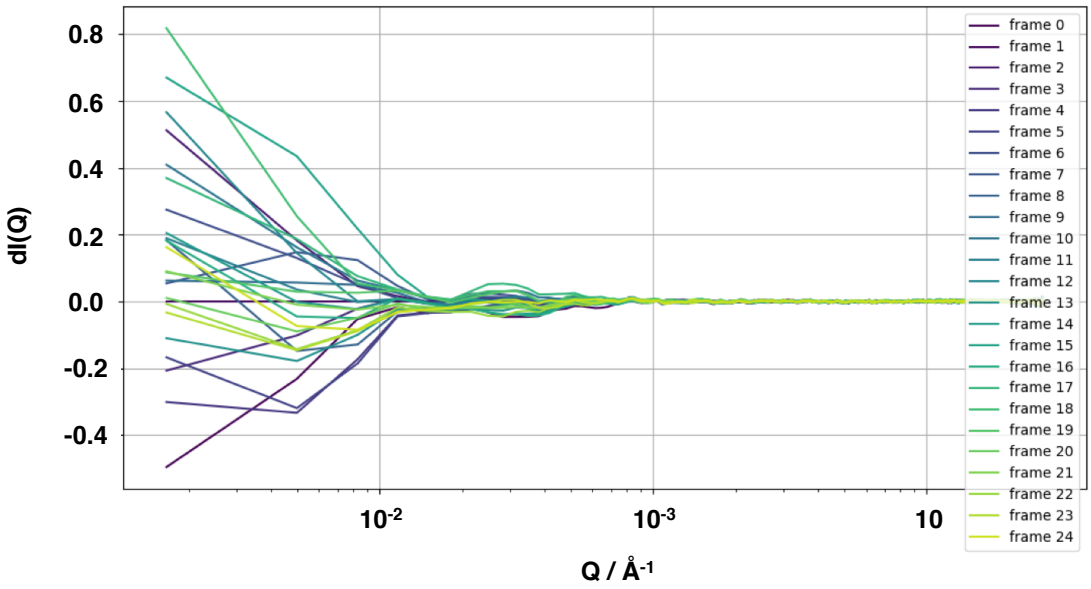

Figure 6.4: Cytochrome *c* radiation damage test difference curves. The progression of frames read out from the detector are coloured as indicated in the legend progressing in colour from purple to light green. The plot shows the scattering vector, Q, on the horizontal axis and the change in scattering intensity from time = 0 on the vertical axis.

The next measurements were of mixing CPR and cyt *c* as previously described. The mixing of these two solutions produced bubbles which led to more undesirable noise in the low-Q region on some of the difference curves. Very strong changes present in the small- and wide-angle scattering regions suggest that this may be radiation damage to the sample in the form of aggregation and heating of the solution, although the trend is extremely systematic as illustrated in Figure 6.5 (an example without any interference from bubble formation). This hypothesis was confirmed by mixing CPR with buffer alone to dilute and then reducing the flux. The same effect was seen with dilution which was then attenuated by reducing the X-ray flux.

The nature of the radiation damage is interesting in itself but the low quality of the SAXS region means that it it difficult to interpret the precise nature of the species being formed. It appears that large structures are forming within hundreds of milliseconds and then rapidly relaxing up to around 8 s when measurements were stopped.

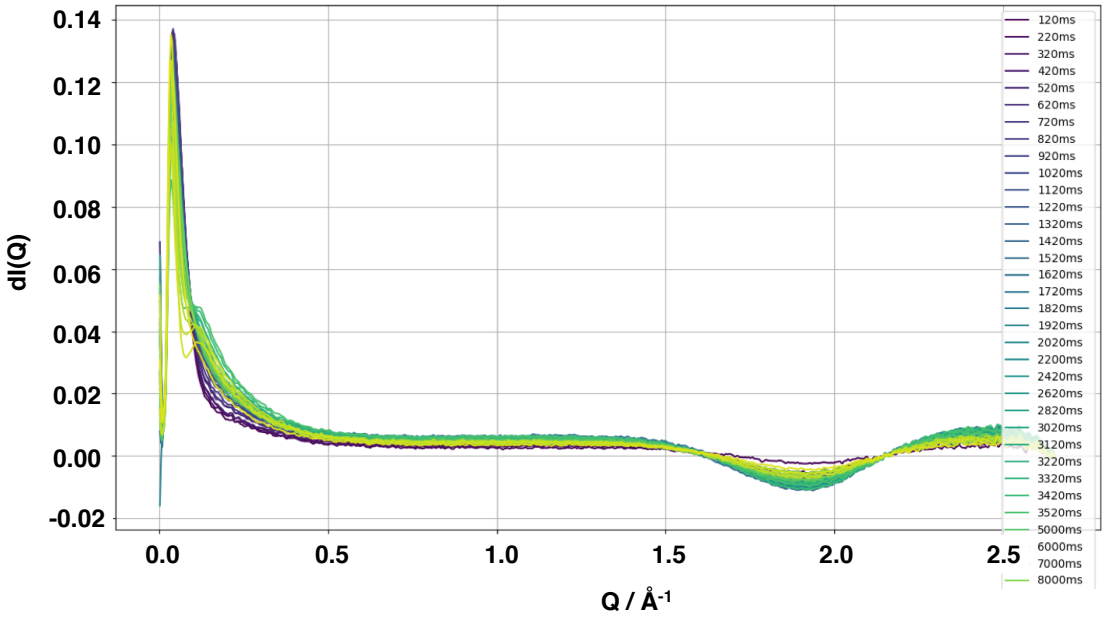

Figure 6.5: CPR + Cytochrome *c* mixing difference curves. The progression of frames read out from the detector are coloured as indicated in the legend, progressing in colour from purple to light green. The plot shows the scattering vector, Q, on the horizontal axis and the change in scattering intensity from time = 0 on the vertical axis.

The final data collected was the mixing of CPR with a solution of 4 M NaCl to determine the effect of a change in ionic strength of the solution. Radiation damage was also present in these samples but a more significant issue was mixing. Mixing and dilution of the salt solution was too slow to be able to take reliable measurements on short timescales and the mixing was extremely inhomogeneous This was not an issue in earlier SAS experiments since the samples were static and averages over long periods of time so poor initial mixing was of no consequence. Additionally, in earlier stopped-flow experiments both of the samples were prepared with the same concentration of salt in order to limit any adverse effects from dilution but this was not possible during the course of this experiment. The dilution appeared to produce some heat currents in the solution and large bubbles.

6.4 Discussion

There were limitations of the beamline that led to significant difficulties in collecting high quality data for this investigation. This was the first attempt to collect stopped-flow time-resolved data on a solution of biological macromolecules on ID09 so the setup is in its infancy and not optimised in any way. The sample was probed with with X-rays that were too soft and therefore a high proportion of beam was absorbed by the sample and the buffer solution, leading to heating and damage to the macromolecules. Due to the nature of the undulator setup, increasing the energy of the X-rays would have led to a significant decrease in the flux which would have been unacceptable on these timescales and the concentration of protein used which was in the region of 10 $\mathrm{mg\,mL^{-1}}$.

It was difficult to interpret the precise nature of the radiation damage to the limited SAXS capability of the beamline. ID09 does not have an evacuated detector tube, only a helium flight tube. This means that there is a significant limitation in the maximum detector distance available and more background noise present in samples that are at a lower concentration. This could have been alleviated by stabilising samples at higher concentration but in the conditions given (100 mM BES pH 7.0, 25 °C) CPR has a tendency to aggregate beyond 10 $\mathrm{mg\,mL^{-1}}$.

Finally, an improvement to the mixing setup could have reduced some of the problems of inhomogeneity and bubble formation and allowed more reliable measurements at the beginning of the interactions. This type of setup has proven successful on beamlines that are better suited to working with solutions of sensitive biological molecules. Examples of this have been discussed in the introduction to this chapter.

6.5 Future Work and Conclusion

TUPS was prepared for this experiment but time constraints and commitment to the stopped-flow setup at the beamline meant that it was not possible to switch to lasers within the allocated beamtime. This experiment would have been carried out in the manner previously described [149] but using X-rays rather than UV-visible light to probe the changes to the molecule. It should also be noted that the strict sample requirements of SAXS/WAXS experiments compared to optical spectroscopy may lead to difficulties. To obtain good scattering data the protein concentrations generally need to be orders of magnitude greater than in optical spectroscopy, this would mean that other reagents which need to be in equimolar ratios or in excess must also be available in much greater quantities. TUPS is typically produced in the microgram-milligram range which may seriously limit the maximum protein

concentration and the inability to recycle samples after X-ray exposure means that repeat measurements may not be possible.

Additionally, the use of NADPH to reduce the enzyme and study the precise rate and structural nature was planned. With the use of WAXS it may be possible to resolve the orientation of the domains relative to one another and the precise extent to which they move. With a functioning and fully synchronised stopped-flow setup further optimisation of the beamline can now take place to improve data collection from sensitive biological samples.

Chapter 7

Summary and Future Work

7.1 Summary of Main Conclusions

A number of significant conclusions have been reached from the interpretation of the data presented in this thesis. They can be summarised as follows:

- The intrinsic link between the redox state of CPR and its conformational equilibrium in solution has been characterised and quantified in Chapter 4.
- The understanding of how buffer conditions affect the conformational equilibrium has been examined, also in Chapter 4.
- A low-resolution structure has been determined for the complex between CPR and cytochrome *c* in solution, revealing the compact nature of the complex, in Chapter 5.
- Time-resolved measurements of the large scale motions of CPR both upon reduction and when complex formation with cytochrome *c* takes place have been made. Although the experiment was completed with limited success, the foundations for further work using the same techniques have been established in Chapter 6.

These findings have significantly furthered the understanding of the behaviour of CPR in solution and established ways in which other flexible proteins, especially members of the diflavin redox family can be studied. Additionally, the power of neutrons for studying sensitive macromolecular complexes has been demonstrated and, despite the lower resolution of this technique, when used in conjunction with other well established techniques can yield strong conclusions.

7.2 Future Work

Despite the fact that CPR has been studied for over 50 years, thanks to constantly evolving techniques there remains much to learn about the behaviour of this fascinating enzyme. In particular a number of incomplete and planned studies remain as a result of this work on CPR. All of the studies presented in this thesis have been carried out with the proteins in solution which, besides cyt *c*, is not their native environment. Additionally cyt *c* is not a physiological electron transfer partner and extensive studies of the complex between CPR and P450s have yet to be published with success. The use of reconstituted liposomes or nanodiscs are at present the most promising candidates combined with SAS to study the native full-length protein and complex, some preliminary studies have already been carried out [64, 68, 152]. It could be possible to use the power of SANS to contrast match the nanodiscs out rendering them experimentally invisible whilst gathering scattering data of the full complex. As an alternative to SAS, the technique of neutron reflectivity could be employed to study the complex in a traditional lipid bilayer on a support surface. This technique relies on the high penetrating power of neutrons to analyse the nature and depths of each layer when a highly collimated beam is reflected off the surface of the sample. As discussed at the end of Chapter 6, there is still a lot of potential to learn about CPR using time-resolved radiation scattering in solution once the experimental setup has been optimised sufficiently. This can be achieved using the rapid mixing setup discussed in the chapter or an electron donating chromophore, such as TUPS, coupled with last excitation which was not attempted due to time constraints.

Besides low-resolution structural studies there is still much to learn about the dynamics CPR and the P450 system. This could be achieved through the use of quasi-elastic neutron scattering. This technique is slowly becoming more popular for the study of biological systems and works by analysing the broadening of incident neutron beam as a result of dynamics in the system and hydration of the protein (in contrast to a crystal with no diffusion that splits the beam into distinct elastic and inelastic lines) [73, 74].

Finally, it is likely that CPR would make an excellent candidate for the technique of cryo-electron microscopy (cryo-EM). Unlike traditional X-ray crystallography this technique does not rely on homogeneous, high-quality crystal formation and therefore permits study of molecules that are notoriously difficult to crystallise, in their native environment [153]. The nature of the technique would allow the structure of molecules in various different conformations to be analysed and then ensemble methods could be used to analyse the conformational equilibrium based on an average structure, or single molecules at a lower resolution, similar to that of SANS

or SAXS. The current major limitation of the technique is the minimum size of the molecule, with acceptable atomic resolution (<5 Å) only being achieved with molecular weights of hundreds of kilodaltons at the time of writing, but this is being constantly diminished as the technique develops [154, 155].

Part III

Appendices

Appendix A

Materials and Methods

In this appendix the routine methods that are relied on throughout this work are presented. These methods are generally accepted to be standard protocols and are therefore not unique to any of the investigations presented earlier. Any aspects of sample preparation or instrument that are specific or unique to certain experiments are discussed in more detail in the relevant results chapter. The first section, A.1, describes the basic DNA techniques, followed by A.2 where expression and purification of CPR both hydrogenated and deuterated is described. Following this is a section on routine analysis and characterisation as complimentary techniques, A.3. The final sections A.4 and A.5 give a detailed overview of the routine methodology for stopped-flow and SANS (on D22) respectively.

A.1 Recombinant DNA Techniques

A.1.1 *E. coli* Expression Vectors

The genes for human fibroblast CPR lacking the N-terminal membrane-anchoring region (and associated mutants) had been cloned by Dr. Jackie Ellis (University of Leicester) in to the cold-shock pCS22 vector (Figure A.1) which is based on the backbone of pET22b [108]. The cDNA for CPR had been inserted into the multiple cloning site between the restriction enzymes XhoI and NdeI. The plasmid features the ampicillin resistance gene and is under cold-shock protein A (cspA) transcription control. When exposed to a low temperature cold shock, 37 °C growth phase followed by 15 °C expression phase, expression is triggered due to the upregulation of cspA. An expression vector without the coding sequence for any form of affinity tag in the amino acid sequence was selected. Cleavage of a tag takes time, reduces yield and an uncleavable tag may result in any number of interferences with structural or kinetic studies.

DNA was cloned into plasmid vectors and sequenced by the University of Le-

icester Protein and Nucleic Acid Chemistry Laboratory (PNACL). Sequencing, also carried out by PNACL, was performed on all plasmid samples after preparation; internal primers based on the CPR insert sequence were used (four forward primers and one reverse, detailed in Appendix B, Supplementary Figures).

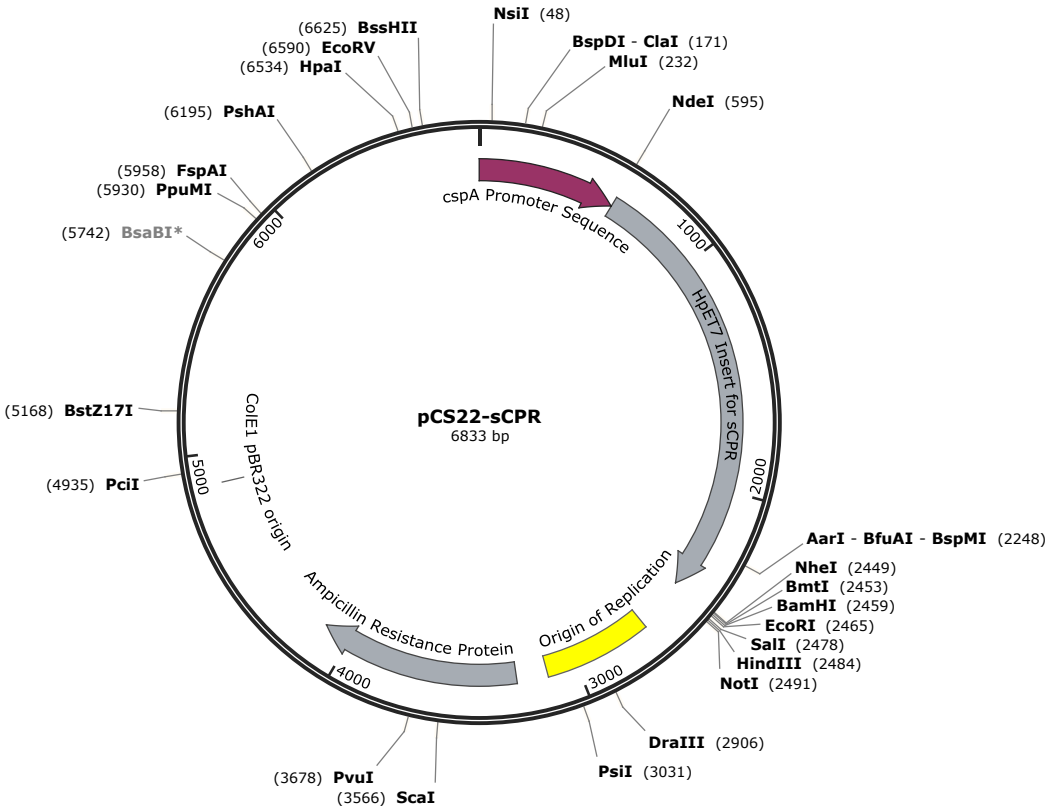

Figure A.1: Plasmid map of the pCS22 CPR expression vector. Indicated around the circumference are the restriction enzymes (outside) and number of base-pairs (increments of 1000, on the inside). The cspA promoter sequence is indicated in purple and the origin of replication in yellow.

A.1.2 Transformation into Competent *E. coli* Cells

A 100 µL aliquot of competent *E. coli* TOP10 cells in a 1 mL Eppendorf tube was thawed on ice. 1 µL of plasmid DNA was added to the cell aliquot which was left on ice for 30 min. The cells and DNA were then heat shocked to 42 °C for 50 s. The mixture was then returned to ice again for a further 2 min. 100 µL of 2xYT growth medium was then added to the tube which was shaker incubated for 60 min at 37 °C. The cells were then pipetted and streaked onto an LB_{amp} agar plate containing ampicillin (100 $\mu g\,mL^{-1}$) which was incubated overnight at 37 °C for growth of bacterial cell colonies.

A.1.3 Isolation of DNA

A single colony of TOP10 cells containing pCS22 CPR DNA was picked from an LB_{amp} agar plate to inoculate 5 mL of LB_{amp} growth medium which was grown at 37 °C to an OD_{600} of 1. The 5 mL culture was then harvested for DNA following the protocol of the Qiagen Maxi Prep plasmid preparation kit.

A.2 Protein Expression and Purification

A.2.1 Human N-terminal Truncated CPR

pCS22 plasmid containing CPR DNA was transformed into *E. coli* BL21 STAR cells for expression (see Appendix A.1.2 for a more detailed procedure). LB_{amp} agar plates were streaked with the transformed BL21 STAR cells and incubated overnight at 37 °C.

Expression in TB Medium

Expression of CPR in TB was developed to provide maximum yield of the protein. A single colony of BL21 STAR transformed with the pCS22 CPR vector was picked from an LB_{amp} agar plate and incubated in autoclaved LB medium (5 mL) containing ampicillin (100 µg mL^{-1}) overnight. A glycerol stock (50%) was made from the overnight growth of the cells in 500 µL aliquots and stored at -80 °C. A scraping (sterile pipette tip) of the glycerol stock cells or single colony from freshly streaked LB_{amp} agar plate was used to inoculate a flask containing LB medium (250 mL) containing ampicillin (100 µg mL^{-1}) which was incubated overnight at 37 °C to form a starter culture. The starter culture (5 mL) was used to inoculate the required amount of TB medium flasks (500 mL) containing ampicillin (100 µg mL^{-1}) for growth and expression. These flasks were shaken (180 RPM) at 37 °C until the OD of the cell culture reached a value between 0.6 and 0.8 at 600 nm. At this point the expression was induced by moving the flasks into a pre-chilled incubator at 15 °C to cold shock the cells for 24 h. Cell cultures were pelleted by centrifugation at 5000 RPM and 4 °C for half an hour before being moved immediately to storage. Pellets were either stored at -80 °C or immediately processed according to the isolation and purification procedure.

Solubility Study

Before beginning large scale purification the solubility of the protein was tested. A small amount of induced cell pellet was resuspended in a minimum of buffer (100 mM, pH 7.8). Cell lysis was achieved by bead milling using a volume of 500 µL of

glass beads with a diameter of 0.1 mM (Scientific Industries Inc.). The suspensions were shaken in a cell disruptor for 5 min. An aliquot with a volume of 50 µL was taken from the sample and centrifuged at 14,000 RPM for 2 min.

Both the precipitate and the supernatant were collected an each sample run on an SDS-PAGE gel. A detailed protocol for SDS-PAGE can be found later in Appendix A.3.1.

Isolation and Purification

CPR isolation and purification was carried out with slight modifications of published methods [40]. The pellets were resuspended in a minimum of lysis buffer (100 mM Tris, pH 7.8, lysozyme 100 µg mL^{-1}, ca. 30 mL of buffer per litre of culture) and then sonicated on ice for 10 x 30 second intervals until the suspension turned dark grey in colour and became less viscous. The suspension was centrifuged at 20,500 RPM for 1 h at 4 °C after sonication and the supernatant crude (cell-free) extract was collected and kept on ice. The crude extract was then loaded directly onto a Q Sepharose ion-exchange column which was pre equilibrated with wash buffer (100 mM Tris, pH 7.8). After a thorough wash of at least 2 column volumes of wash buffer, the protein was eluted with a salt gradient (0-1 M NaCl in wash buffer). During elution the optical absorbance was monitored at wavelengths of 280 nm and 450 nm to confirm protein and flavin presence respectively. The best yellow/green fractions from Q Sepharose elution (see example elution trace in Figure A.2, CPR presence in fractions C2 - C4 confirmed with SDS-PAGE) were then loaded directly onto a 2'5'-ADP Sepharose column which was pre equilibrated with wash buffer. After a 2 column volume wash, half a column volume of oxidation buffer (100 mM Tris, pH 7.8, 100 mM potassium ferricyanide) was washed over the bound protein to ensure the flavin cofactors of the enzyme were in the fully oxidised state. The column with oxidised CPR bound was then washed once more before being eluted slowly with elution buffer (20% glycerol in H_2O, pH 7). The pure protein was eluted using a 20% glycerol solution rather than 2'-AMP in order to avoid undesired persistent binding of the 2'-AMP. A final stage of purification included the use of size exclusion liquid chromatography (Superdex 200 Increase column, GE Healthcare Life Sciences) in order to isolate the purely monomeric form of the protein. The protein concentration was calculated using a molar extinction coefficient of ϵ_{450nm} = 22,000 $M^{-1}\,cm^{-1}$. The final eluent was immediately buffer exchanged into 100 mM Tris, pH 7.8 for refrigerator storage or kinetics buffer (100 mM BES, pH 7) for experimental work as required. Glycerol stocks using 50% w/v of glycerol were made for long term storage at -20 °C.

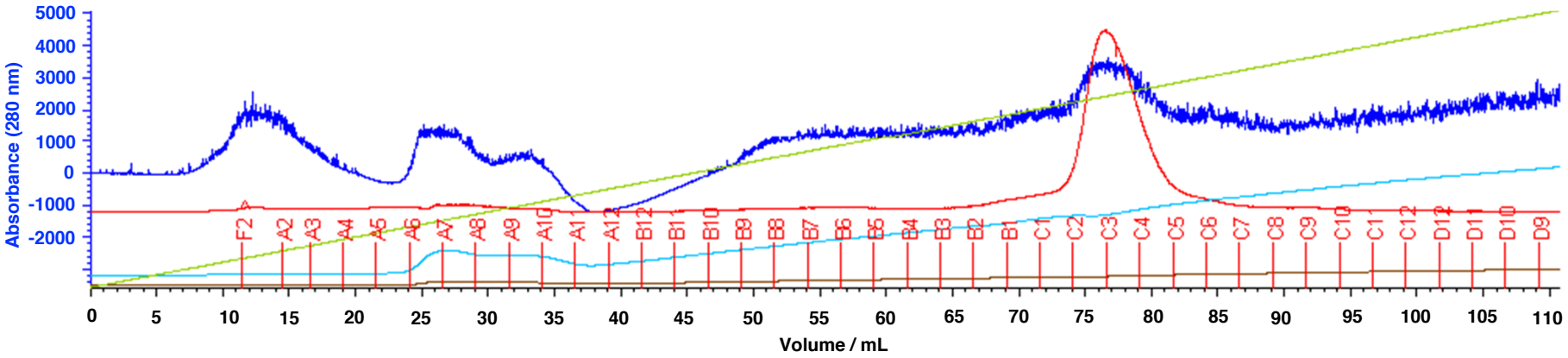

Figure A.2: Q Sepharose FPLC elution chromatogram run at 3 mL min^{-1}. Traces shown are the absorption reading at 280 nm (**dark blue**), the absorption reading at 450 nm (**red**), the% of 1 M NaCl (**green**) and the conductivity of the solution measured in siemens per metre (**light blue**). The vertical axis corresponds to the absorabance of the 280 nm. The fractions are labelled on the chromatogram in red, of which fractions C2 to C4 were collected and pooled for further purification in this instance.

A.2.2 Deuterated Protein Expression and Purification

A modified protocol and some additional procedures were necessary for the production of deuterated soluble CPR in the D-lab at the ILL in Grenoble, France. The purification protocol for deuterated samples was the same as for hydrogenated.

Transposition

The pCS22 vector based construct was adapted for fermenter growth by switching the antibiotic resistance from ampicillin to kanamycin via a transposition reaction using the EZ-Tn5TM T7/KAN-2 Promoter Insertion Kit (Epicentre, USA). All components from the kit for carrying out the transposition reaction were mixed in a single Eppendorf tube:

- EZ-Tn5TM 10x reaction buffer (1 µL)
- Target DNA (0.2 µg)
- Transposon (1 µL)
- Transposase (1 µL)
- Make up to 10 µL total volume with distilled water

The reaction mixture was incubated (37 °C for 2 h). The reaction mixture was than centrifuged for (10 s at maximum speed) in a bench-top centrifuge before adding stock stop solution (1 µL). The solution was then kept on ice until before transformed into *E. coli* TOP10 cells using the protocol described above.

The transformed cells were then screened for successful transposition which involved plating cells onto an LB_{kan} agar plate to grow kanamycin resistant colonies. Individual colonies from the kanamycin plate were then plated out on an LB_{amp} and an LB_{kan} using corresponding numbers on a grid and searching for cells which had lost ampicillin but simultaneously gained kanamycin resistance, ensuring the transposition reaction had taken place on the correct part of the plasmid DNA. A single colony was once again picked from these plates and double checked on two final LB_{amp} and LB_{kan} agar plates. The two final steps are illustrated below in Figure A.3. Successful cells were than used for further DNA isolation and sequencing in order to verify integrity of the CPR gene.

Hydrogenated Minimal Medium Adaptation

Expression and solubility studies were carried out as before using hydrogenated minimal medium as the first stage of adaptation to growth in harsher conditions. A single colony was used to inoculate 15 mL of hydrogenated filter sterilised minimal

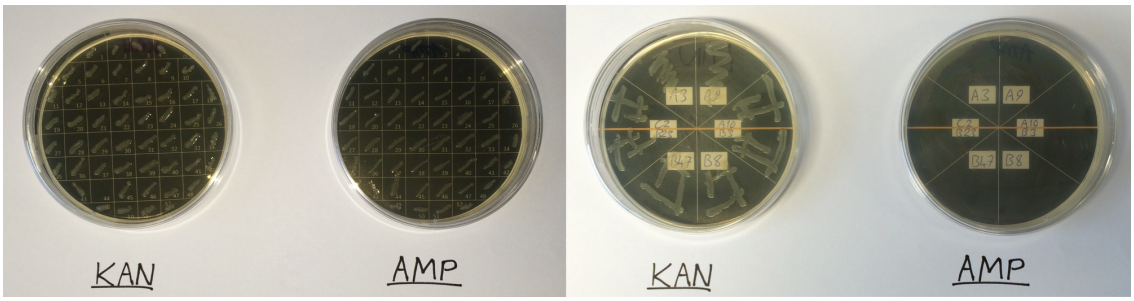

Figure A.3: Agar plates from the screening procedure of the transposition protocol. The left plates are a large selection of single colonies picked from the initial LB_{kan} plate. The right plates are from the final confirmation of new resistance and loss of former resistance gene

medium (see materials section, Appendix A.2.3) containing a final kanamycin (30 $\mu g\,mL^{-1}$). The starter culture was incubated (37 °C, 190 RPM shaking) for 24 hours until the O.D. reached 1-1.5 A.U., indicating a slower growth rate than in rich medium. After 34 hours from the start of the incubation at 37 °C 1 mL of culture was extracted and a 10 fold dilution in kanamycin containing hydrogenated minimal medium was made. The diluted culture was incubated at 37 °C for 16 h and reached an O.D. of around 3.6 A.U. Three aliquots were extracted from the culture. Each aliquot was diluted in kanamycin containing minimal medium to obtain an O.D. of 0.2 A.U. The three cultures were incubated at 37 °C for several hours. Expression was induced by reducing the temperature of the incubator to 15 or 16 °C when the O.D. reached a value between 0.6 and 0.9 A.U. A temperature of 20 °C was also tested to confirm expression at slightly higher temperatures in case it was necessary in later steps due to equipment limitations. This procedure was repeated two further times in order to ensure good adaptation of the cells before taking an aliquot of uninduced cell as a glycerol stock stored in 50% glycerol at -80 °C. Expression and solubility studies were carried out as described in A2.1 and the results are shown in Figure A.4.

Deuterated Minimal Medium Adaptation and Solubility Study

Following adaptation for hydrogenated minimal medium a similar procedure was carried out using 85% D_2O deuterated minimal medium. Deuterated minimal medium was prepared, being analogous to hydrogenated minimal medium except for the use of D_2O rather than H_2O. Ingredients of the medium, including the antibiotic were not deuterated. This yielded a medium that would produce an 85% deuterated protein suitable for contrast matching.

Hydrogenated minimal medium culture (1 mL) was diluted to 15 mL in kanamycin containing deuterated minimal medium and incubated at 37 °C for 24 hours until

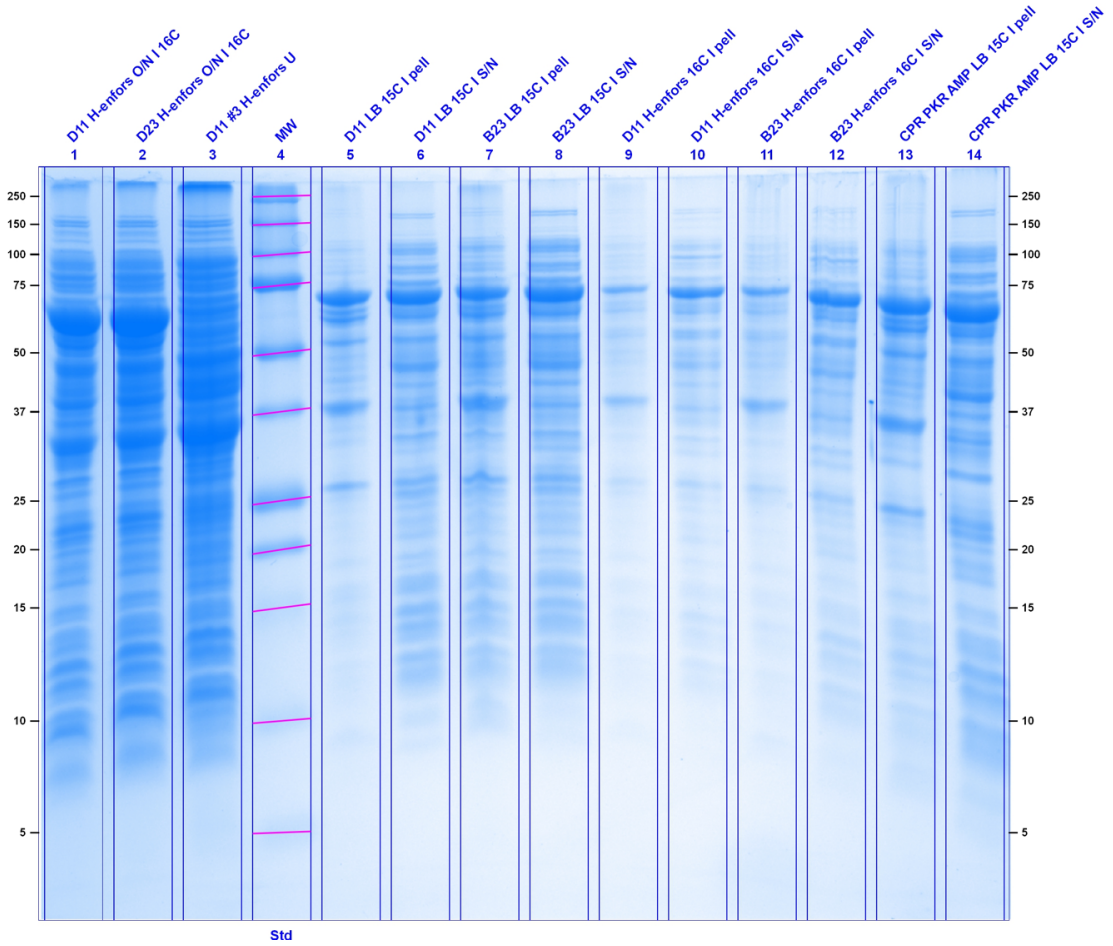

Figure A.4: Hydrogenated minimal medium expression and solubility study. *Lanes 1 and 2*: Show the total lysis of two induced H-minimal medium expressions. *Lane 3*: An uninduced H-minimal medium sample. *Lane 4*: Molecular weight marker. *Lane 5 - 8*: Solubility trial supernatant and pellet of samples induced at 15 °C in LB. *Lane 9 - 12*: Solubility trial supernatant and pellet of samples induced at 16 °C in H-minimal medium. *Lane 13 and 14*: Solubility trial supernatant and pellet of non-transposed CPR samples induced at 15 °C in LB. Molecular weight in kDa is indicated by the labels in black on the right hand side.

the O.D. reached a value of 3 - 3.5 A.U. The resulting culture (1 mL) was added to a final volume of 15 mL in kanamycin containing deuterated minimal medium and incubated at 37 °C for 24 hours until the O.D. reached a value of 3 - 3.5 A.U.

Four aliquots of 1 mL each were diluted in kanamycin containing deuterated minimal medium to final O.D. of about 0.2 A.U. The four samples were incubated at 37 °C until the O.D. reached a value between 0.6 and 0.8 A.U. Expression was induced by reducing the temperature of the incubator to 16 °C and 20 °C to confirm that both temperatures were still effective. Expression was carried out at 16 °C and 20 °C. The SDS-PAGE samples were prepared as described in Appendix A.3.1 and analysed as described in the previous subsection. Induction at 20 °C yielded the largest amount of protein in the soluble fraction. This procedure was repeated for a

further 3 dilution and growth steps to ensure full adaptation to growth in deuterated minimal medium.

Fermenter Growth and Expression

The use of a fermenter rather than more typical growth in large flasks was motivated by the need to grow a high cell density with a minimal use of materials due to the high cost of D_2O. This would also limit exposure to hydrogen since oxygen is supplied to the culture thought a dry air line. A Labfors 2.3 L Bioreator (Infors, France) was used (Figure A.5) allowing very precise control of conditions through the use of direct feeding pumps and various probes.

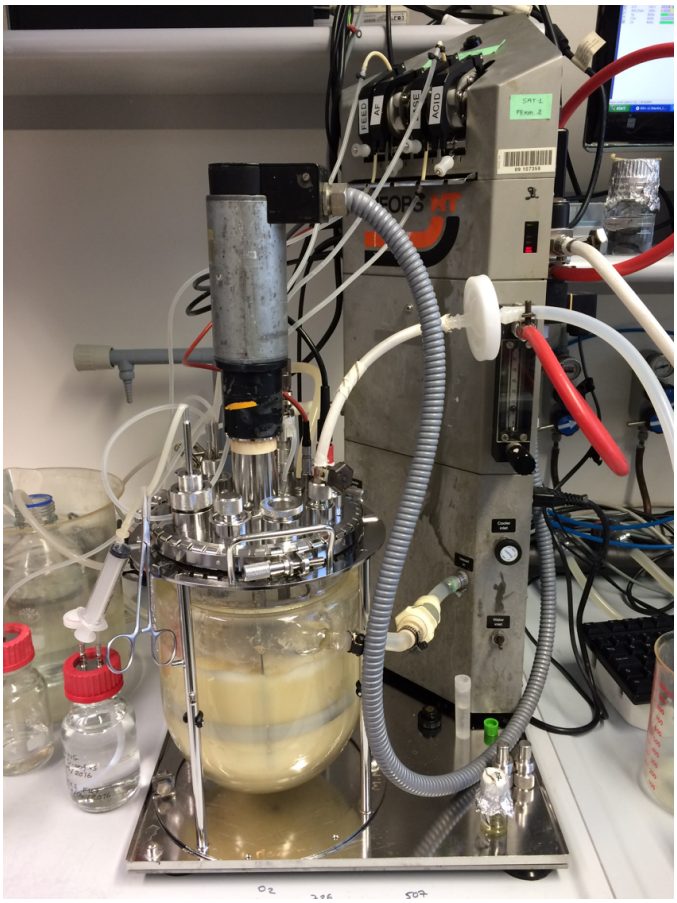

Figure A.5: Photograph of the Fermenter Apparatus in use. The insulated (double glass layer) fermenter vessel is shown in the bottom left with fermentation in progress and the stirrer motor is visible mounted to the top of the vessel (grey). The labelled feeding pumps are in the top right of the apparatus with the PC for direct control and monitoring behind.

The O_2 pressure in the medium was measured throughout the procedure as reported in Figure A.7. Temperature and pH were monitored during the process. The O.D. was measured manually throughout the procedure, by extracting small samples of culture, and is shown in black in Figure A.7. Fermentation was carried

out at 30 °C with stirring. To maintain the correct pH (7.0) an NaOH pump was used supplying 4% NaOH to the culture when the pH value was reported below a threshold value. During the first 14 h from the start of fermentation the oxygen content decreased due to bacteria growth. After 36 h the oxygen level increased significantly due to decreasing bacteria growth rate. The culture was then fed through a feeding pump as shown by the red curve in figure 8.6 providing feeding medium whose composition is described in the materials section. Expression was induced when the optical density reached the value of 18 A.U. The temperature was gradually decreased to 19 °C. 22 h after induction the cells were harvested by centrifugation (4500 RPM and 4 °C, 15 min. A total of 65 g of cell paste was obtained from 1.7 L final culture volume, this was frozen and stored at -80 °C. The final yield of deuterated CPR was approximately 120 mg. An SDS-PAGE gel was made to confirm the expression and is show in Figure A.6 where bands at the correct molecular weight for CPR are clearly visible.

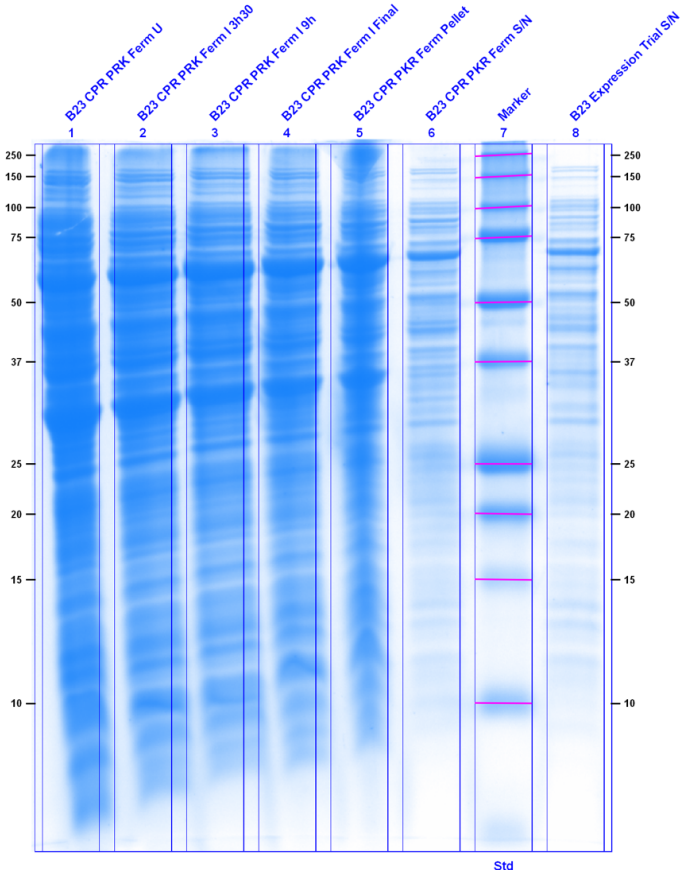

Figure A.6: Fermenter Results Gel. *Lane 1*: Uninduced samples from the fermenter, immediately before induction *Lanes 2 and 3*: Induced samples after 3.5 and 9 hours respectively. *Lane 4*: Final induced sample before cell harvesting. *Lane 5 and 6*: Solubility trial supernatant and pellet of samples induced at 19 °C. *Lane 7*: Molecular weight marker. *Lane 8*: Solubility trial supernatant of CPR sample induced at 15 °C in LB for reference. Molecular weight in kDa is indicated by the labels in black on the right hand side.

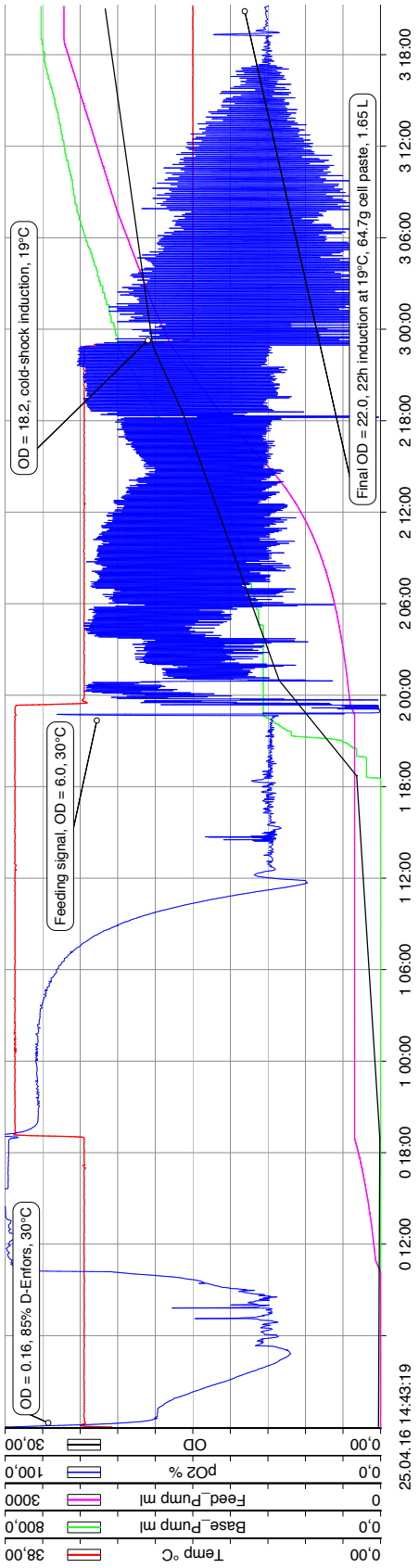

Figure A.7: Fermenter Trace. The horizontal axis shows time in days, hours and minutes, the vertical axis shows O.D. Conditions monitored as per the coloured lines detailed in the legend Indicated in the text bubbles are the time points and values at which a manual O.D. reading was taken.

A.2.3 Materials

All chemicals and media used were of the highest analytical grade and were not purified any further unless otherwise stated. Chemicals for solutions were provided by Fisher Chemicals, Sigma Aldrich and Melford laboratories. Horse heart cytochrome *c* for kinetics and SAS experiments was purchased from Sigma Aldrich. Water was doubly deionised via an Elga PureLab Option (DV35) which used lab deionised water as its supply. All molecular biology and microbiology was carried out under aseptic conditions. The pH of solutions was measured using a Hanna pH meter. FPLC column chromatography was carried out using an ÄKTA Purifier 100. UV-visible spectrophotometry was carried out using a Perkin-Elmer Lambda 40. Additional specific equipment is described within the relevant subsection of this chapter. All buffer solutions were filtered immediately before use for both purification purposes or measurements.

Materials for the expression and measurement of CPR

- **LB-Agar medium** - 20 g of LB low salt powder (Melford), 15 g of agar and 2 g of glucose made up to 1 L with distilled water. The solution was sterilized in an autoclave.
- **Lysogeny broth (LB) medium** - 20 g of LB low salt powder (Melford) and 2 g of glucose made up to 1 L with deionized water. The solution was sterilized in an autoclave.
- **Terrific broth (TB) medium** - 12 g of tryptone, 24 g of yeast extract, 4 mL of glycerol made up to 900 mL with distilled water. The solution was sterilised in an autoclave before adding 100 mL of a sterile solution of 0.17 M KH_2PO_4, 0.72 M K_2HPO_4.
- **Kinetics/SANS buffer** - 100 mM BES, pH 7.0. Solution was made up using H_2O, D_2O or a mixture of both as appropriate.

Materials for the deuteration of CPR

- **Minimal medium** - In 1 litre: 6.86 g $(NH_4)_2SO_4$, 1.56 g KH_2PO_4, 6.48 g $Na_2HPO_4 \cdot 2\,H_2O$, 0.49 g $(NH_4)_2-H-$citrate, 5 g glycerol, 1 mL $MgSO_4$ 1 M, 1 mL metal salts solution. H_2O based solution was sterilised in an autoclave, D_2O based solution was sterilised by filtration.
- **Metal salts solution** - 0.5 g L^{-1} $CaCl_2 \cdot 2\,H_2O$, 16.7 g L^{-1} $FeCl_3 \cdot 6\,H_2O$, 0.18 g L^{-1} $ZnSO_4 \cdot 7\,H_2O$, 0.16 g L^{-1} $CuSO_4 \cdot 5\,H_2O$, 0.15 g L^{-1} $MnSO_4 \cdot 4\,H_2O$, 0.18 g L^{-1} $CoCl_2 \cdot 6\,H_2O$, 20.1 g L^{-1} Na−EDTA.

- **NaOD 4%** - 90 mL of D_2O, 10 mL NaOD in D2O 10 M stock. Sterilised by filtration.
- **Feeding medium** - 30 g glycerol, 250 mL deuterated minimal medium. Sterilised by filtration.

A.3 Analysis and Characterisation

A.3.1 SDS-PAGE

To follow the progress of CPR purification and to assist with confirmation of purity SDS-PAGE analyses were carried out using a Mini Protean Tetra System (Bio-RAD, California, USA) set at 150 V. Discontinuous polyacrylamide gels (10%) containing 0.1% SDS and polyacrylamide stacking gel (5%) were used. A Bio-Rad gel system with 0.75 mm gel thickness was used. Samples were prepared by adding an equal volume of sample and sample buffer (100 mM Tris-HCl, pH 6.8, 4% SDS, 20% w/v glycerol, 0.002% bromophenol blue, 25 mM DTT) then boiled for 5 min. The gels were run in SDS running buffer (25 mM Tris-HCl, 192 mM glycerine, 0.5% w/v SDS) at 180 V until the dye front reached the end of the gel.

Gels were soaked in stain (30% w/v methanol, 12% w/v trichloroacetic acid, 0.01% Coomassie Blue, 10% w/v sulphosalicylic acid) for 1 h before rapid destaining using 3-4 iterations of shaking in fresh microwave heated distilled water to accelerate the process. For a full destain the gels were left to shake in distilled water overnight.

Materials for SDS-PAGE

Solution Components	10% Resolving Gel (mL)	5% Stacking Gel (mL)
H_2O	4.0	6.8
30% acrylamide mix	3.3	1.7
1.0 M Tris (pH 6.8)	2.5	1.25
10% SDS	0.1	0.1
10% ammonium persulfate	0.1	0.1
TEMED	0.004	0.01

Table A.1: 10 mL Solutions for Preparing Gels for Tris-glycine SDS-PAGE.

A.3.2 UV-Visible Absorption Spectroscopy

Ultraviolet-visible (UV-visible) absorption spectra were used to confirm the presence of the protein and respective flavins in the fully oxidised state immediately after purification. The yield of protein was also quantified using the extinction coefficient:

$\epsilon_{450\text{nm}}$ = 22,000 $\text{M}^{-1}\,\text{cm}^{-1}$) [40]. This measures the oxidised flavin content rather than the protein but is considered a very accurate method with a fully oxidised sample of CPR. The extinction coefficient for the protein at 280 nm was estimated to be $\epsilon_{280\text{nm}}$ = 84,000 $\text{M}^{-1}\,\text{cm}^{-1}$ [109] based on the amino acid sequence.

A.3.3 Cytochrome *c* Reduction Assays

Assays were carried out generally according to a published protocol [13]. Protein was buffer exchanged into kinetics buffer (100mM BES, pH 7) and the concentration was determined by UV-visible spectroscopy. Stock solutions of NADPH ($\epsilon_{340\text{nm}}$ = 6220 $\text{M}^{-1}\,\text{cm}^{-1}$) and horse heart cytochrome *c* ($\epsilon_{480\text{nm}}$ = 106,000 $\text{M}^{-1}\,\text{cm}^{-1}$) were made. All stocks and subsequent dilutions were kept on ice in foil wrapped Eppendorf tubes. The spectrophotometer was blanked at 550 nm with a mixture of CPR and cytochrome *c* (saturating) in the kinetics buffer which was allowed to stabilise for 1 min. NADPH (50 µM) was added, followed by rapid agitation and then measurement of absorbance change at 500 nm. The slope of the curve was measured for several repeats and the catalytic rate constant under saturating conditions was determined using

$$\left(\frac{\Delta_{Abs}}{19000}\right) \div [\text{CPR}] = k_{\text{cat}} \tag{A.1}$$

where 19000 is the molar extinction coefficient for the formation of reduced cytochrome *c* at 550 nm.

For Michaelis-Menten kinetic parameter determination (${K_\text{M}}^{\text{cytochrome}c}$ and V_{max}) the concentration of cytochrome *c* was varied whilst that of CPR (5 µM) and NADPH (50 µM) remained constant. This produced a hyperbolic curve which was analysed using a nonlinear regression using the model

$$Y = V_{max} \times X \div (K_\text{M} + X) \tag{A.2}$$

where V_{max} is the maximum rate achieved by the system at saturating substrate concentration and K_M, the Michaelis constant is the substrate concentration at which the rate is half of V_{max}.

A.4 Stopped-Flow Kinetics

All kinetic experiments were carried out at room temperature (approx 25 °C, unless otherwise specified) using an SX.18 MV-R stopped-flow spectrophotometer (Applied Photophysics, UK) with a dead time of ca. 1 ms. A photodiode array was used in order to provide the full spectrum of UV-visible wavelengths at the same time. The

sample-handling unit of the stopped flow instrument was contained within a customized glovebox (Belle Technology, UK). Kinetics buffer (100 mM BES pH 7) was made anaerobic by bubbling nitrogen gas for ca. 2 h prior to placing in the anaerobic glovebox. Reagent solutions were made up in small volumes (<1.5 mL) outside the glovebox but allowed to equilibrate for at least an hour inside the glovebox to ensure removal of residual dissolved oxygen. Anaerobic samples were introduced into the sample syringes and allowed to equilibrate for 5 min where necessary (for example in the case of NADPH and CPR in the same syringe). The system was cleaned by driving two samples through the observation cell before taking any recordings. In single mix mode, the equipment operates by mixing and therefore diluting two samples in equal volume, therefore halving the starting concentration. Absorbance measurements are made over a set time period up to 1000 s and a spectrum can be taken every millisecond if required; this was varied depending on the timescale used. The entire UV-visible spectrum was recorded in each measurement but single wavelength data were obtained from these readings where necessary. Kinetic and mechanistic parameters were calculated from the data obtained with most analysis carried out using the Pro-Data SX software package (Applied Photophysics, UK).

A.5 Small-Angle Scattering

The predominant SAS technique presented in this thesis is SANS and therefore a detailed generic protocol for SANS measurements on solution CPR on ILL D22 is given below. Specific aspects of sample preparation that are unique for a particular experiment are described in the relevant results chapter.

A.5.1 SANS Data Collection and Routine Analysis

SANS measurements were carried out on the D22 beamline, the high-flux neutron diffractometer at the Institut Laue-Langevin, Grenoble, France. Each protein sample of 2-5 $\mathrm{mg\,mL^{-1}}$ in an appropriate H_2O- or D_2O-based buffer was measured in a 1 mm path length suprasil quartz cuvette (Hellma) for a total of 1 h in order to gather data with a suitably high statistical precision. Data were recorded at two collimation lengths (5.6 m and 2.8 m) and respective sample-to-detector distances (5.6 m and 1.4 m) in order to provide a full range of momentum transfer, Q, from the Guinier region of the monomer to the solvent level of incoherent scattering. The 2-dimensional ^{3}He detector was positioned at different distances from the sample and off-centred with regard to direct beam in order to provide a usable Q-range of 0.001 - 0.5 $\mathrm{Å^{-1}}$, where $Q = 4\pi \sin\theta/\lambda$ with 2θ and λ the wavelength (6 Å ±10% in our measurements). The raw scattering data were reduced using the software

GRASP, which included thickness and transmission scaling, empty cell and blocked beam subtractions, calibration to absolute intensity using incident flux measured at sample position and azimuthal averaging then merged to produce the full scattering curves. Buffer subtraction and normalisation for concentration as appropriate was carried out using NCNR SANS reduction macros (Nist Centre for Neutron Research, Maryland, USA) for the IGORpro software package [156].

Where necessary, contrast match points were estimated by determining and plotting the ${I_{(Q=0)}}^{1/2}$ values of protein samples at various D_2O:H_2O ratios while maintaining a constant protein concentration. The linear trend was then used to estimate the D_2O:H_2O ratio at which the protein no longer contributed any coherent scattering (i.e. the x-axis intercept). This estimate was then tested and confirmed before proceeding with contrast match SANS measurements on the protein complex.

Initial data processing and analysis were carried out using programs from the ATSAS suite [157]. Determination of size parameters was performed using PRIMUS [158]. Rg was determined using the Guinier approximation and from $P(r)$ plots; D_{max} and $P(r)$ were calculated using GNOM [159]. The Primus Distance Distribution Wizard gave values of at least 77% for the quality of $P(r)$ for the different samples, where values over 70% indicate a "good" solution. Model-independent *ab initio* molecular envelopes were generated using DAMMIF [160]. Fifteen independent DAMMIF runs were averaged using DAMAVER [99] to obtain a typical molecular shape and filtered using DAMFILT to produce a refined model revealing only the most common structural features. High resolution models were superimposed on to low resolution dummy atom models using SUPALM [104] as part of the SASpy [102] plugin for PyMol.

Rigid body modelling was carried out using software from the IMP (Integrative Modelling Platform) suite [140] and the ATSAS suite. A pool of 10,000 conformational samples was created using the RRT (rapidly exploring random tree) sampling tool, which was provided with a PDB structure and a selection of flexible residues. Theoretical scattering curves were calculated for each of the sampled conformations using CRYSON [115]. A single best fit model to the experimental data was determined using MultiFoXS [114] in partial mode, where precomputed scattering intensities were used. Alternatively a fixed number of known models were used, rather than a large pool, to suit the investigation.

Appendix B

Supplementary Figures

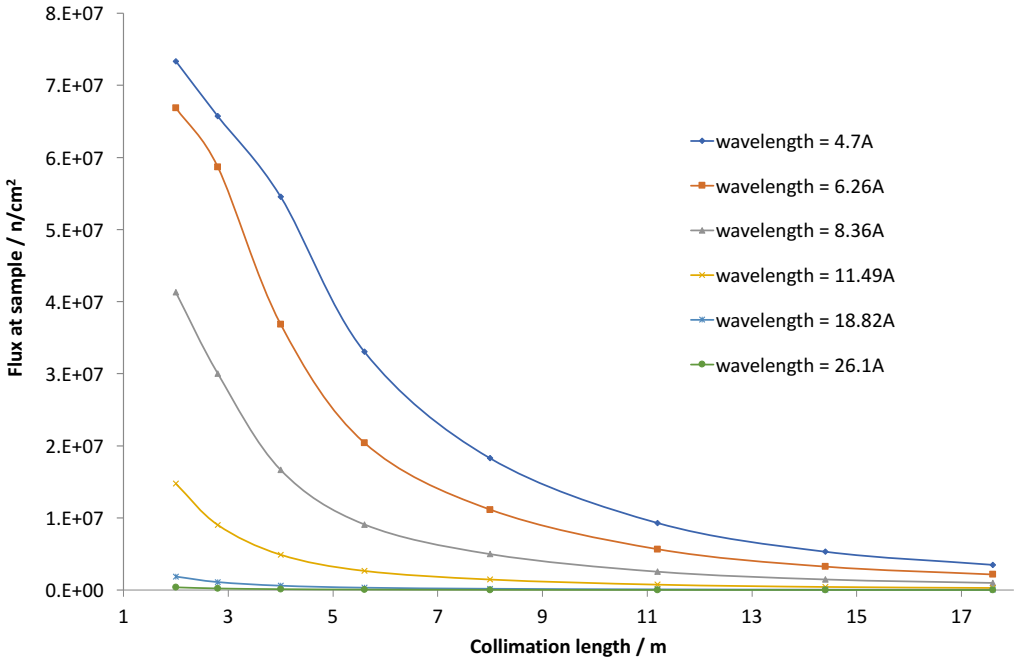

Figure B.1: D22 Flux at Sample Position

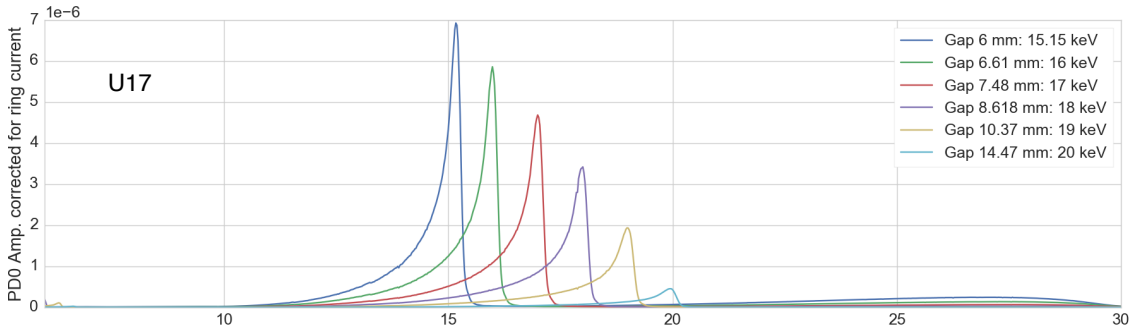

Figure B.2: ID09 Intensity as a function of X-ray energy. In this case the U17 undulator is in place where the gap between each fixed dipole magnet is 17 mm

Human NADPH-Cytochrome P450 Reductase Sequencing Primers

Listed are the sequencing primers used for the trunctated CPR construct presented in this work which was cloned in to the pCS22 plasmid.

CPR forward 1 - *tttctgcatggccaccta*

CPR forward 2 - *cacctggaattggacatctc*

CPR forward 3 - *ttgtggagtacgagaccaag*

CPR forward 4 - *ggtggactacatcaagaaac*

CPR reverse 1 - *gaagtgctcgaggtcttgt*

Bibliography

[1] Cy M. Jeffries, Melissa A. Graewert, Clement E. Blanchet, David B. Langley, Andrew E. Whitten, and Dmitri I. Svergun. Preparing monodisperse macromolecular samples for successful biological small-angle x-ray and neutron-scattering experiments. *Nat. Protocols*, 11(11):2122–2153, 2016.

[2] C. Xia, S. P. Panda, C. C. Marohnic, P. Martasek, B. S. Masters, and J. J. Kim. Structural basis for human nadph-cytochrome p450 oxidoreductase deficiency. *Proceedings of the National Academy of Sciences*, 108(33):13486–91, 2011. ISSN 1091-6490 (Electronic) 0027-8424 (Linking).

[3] Kim J.J.P. Waskell, L. *Cytochromes P450: Structure, Function and Mechanism*. Springer, London, 2015.

[4] D.F. Lewis. *Cytochromes P450: Structure, Function and Mechanism*. Springer, 1996.

[5] M. Klingenberg. Pigments of rat liver microsomes. *Archives of biochemistry and biophysics*, 75(2):376–86, 1958. ISSN 0003-9861.

[6] T. Omura and R. Sato. The carbon monoxide-binding pigment of liver microsomes. i. evidence for its hemoprotein nature. *The Journal of biological chemistry*, 239:2370–8, 1964. ISSN 0021-9258.

[7] I. G. Denisov, T. M. Makris, S. G. Sligar, and I. Schlichting. Structure and chemistry of cytochrome p450. *Chem Rev*, 105(6):2253–77, 2005. ISSN 0009-2665 (Print) 0009-2665.

[8] Scrutton N.S. Munro A.W. Gutierrez A. Roberts-G.C.K. Wolf C.R. Paine, M.J.I. *Cytochromes P450: Structure, Function and Mechanism*. 1996.

[9] Y. Yasukochi and B. S. S. Masters. Some properties of a detergent-solubilized nadph-cytochrome c (cytochrome-p-450) reductase purified by biospecific affinity chromatographrome p-450) reductase purified by biospecific affinity chromatography. *Journal of Biological Chemistry*, 251(17):5337–5344, 1976. ISSN 0021-9258.

[10] B. A. Schacter, E. B. Nelson, B. S. S. Masters, and H. S. Marver. Immunochemical evidence for an association of heme oxygenase with microsomal electron-transport system. *Journal of Biological Chemistry*, 247(11):3601–3603, 1972. ISSN 0021-9258.

[11] F. P. Guengerich. Reduction of cytochrome b5 by nadph-cytochrome p450 reductase. *Arch Biochem Biophys*, 440(2):204–11, 2005. ISSN 0003-9861 (Print) 0003-9861.

[12] T. Ono, K. Takahashi, S. Odani, H. Konno, and Y. Imai. Purification of squalene epoxidase from rat liver microsomes. *Biochemical and Biophysical Research Communications*, 96(1):522–528, 1980. ISSN 0006-291X.

[13] F. Peter Guengerich, Martha V. Martin, Christal D. Sohl, and Qian Cheng. Measurement of cytochrome p450 and nadph-cytochrome p450 reductase. *Nat. Protocols*, 4(9):1245–1251, 2009. ISSN 1754-2189.

[14] T. M. Hedison, S. Hay, and N. S. Scrutton. Real time analysis of conformational control in electron transfer reactions of human cytochrome p450 reductase with cytochrome c. *FEBS Journal*, 2015. ISSN 1742-4658 (Electronic) 1742-464X (Linking).

[15] Ming Wang, David L. Roberts, Rosemary Paschke, Thomas M. Shea, Bettie Sue Siler Masters, and Jung-Ja P. Kim. Three-dimensional structure of nadph–cytochrome p450 reductase: Prototype for fmn- and fad-containing enzymes. *Proceedings of the National Academy of Sciences*, 94(16):8411–8416, 1997.

[16] T. Iyanagi, C. W. Xia, and J. J. P. Kim. Nadph-cytochrome p450 oxidoreductase: Prototypic member of the diflavin reductase family. *Archives of Biochemistry and Biophysics*, 528(1):72–89, 2012. ISSN 0003-9861.

[17] T. Iyanagi, N. Makino, and H. S. Mason. Redox properties of reduced nicotinamide adenine-dinucleotide phosphate-cytochrome p-450 and reduced nicotinamide adenine dinucleotide-cytochrome b5 reductases. *Biochemistry*, 13(8): 1701–1710, 1974. ISSN 0006-2960.

[18] T. Iyanagi and H. S. Mason. Some properties of hepatic reduced nicotinamide adenine-dinucleotide phosphate - cytochrome-c reductase. *Biochemistry*, 12 (12):2297–2308, 1973. ISSN 0006-2960.

[19] T. Senda, M. Senda, S. Kimura, and T. Ishida. Redox control of protein conformation in flavoproteins. *Antioxidants and Redox Signaling*, 11(7):1741–1766, 2009. ISSN 1523-0864.

[20] A. Gutierrez, A. Grunau, M. Paine, A. W. Munro, C. R. Wolf, G. C. K. Roberts, and N. S. Scrutton. Electron transfer in human cytochrome p450 reductase. *Biochemical Society Transactions*, 31:497–501, 2003. ISSN 0300-5127.

[21] L. Aigrain, F. Fatemi, O. Frances, E. Lescop, and G. Truan. Dynamic control of electron transfers in diflavin reductases. *International Journal of Molecular Sciences*, 13(11):15012–15041, 2012. ISSN 1422-0067.

[22] M. B. Murataliev, R. Feyereisen, and A. Walker. Electron transfer by diflavin reductases. *Biochimica Et Biophysica Acta-Proteins and Proteomics*, 1698(1): 1–26, 2004. ISSN 1570-9639.

[23] Y. V. Grinkova, I. G. Denisov, and S. G. Sligar. Functional reconstitution of monomeric cyp3a4 with multiple cytochrome p450 reductase molecules in nanodiscs. *Biochemical and Biophysical Research Communications*, 398(2): 194–198, 2010. ISSN 0006-291X.

[24] K. D. Watenpau, L. C. Sieker, and L. H. Jensen. Binding of riboflavin-5'-phosphate in a flavoprotein - flavodoxin at 2.0-a resolution. *Proceedings of the National Academy of Sciences*, 70(12):3857–3860, 1973. ISSN 0027-8424.

[25] P. A. Karplus, M. J. Daniels, and J. R. Herriott. Atomic-structure of ferredoxin-nadp+ reductase - prototype for a structurally novel flavoenzyme family. *Science*, 251(4989):60–66, 1991. ISSN 0036-8075.

[26] D. J. Stuehr, J. Tejero, and M. M. Haque. Structural and mechanistic aspects of flavoproteins: electron transfer through the nitric oxide synthase flavoprotein domain. *FEBS Journal*, 276(15):3959–3974, 2009. ISSN 1742-464X.

[27] K. R. Wolthers, X. D. Lou, H. S. Toogood, D. Leys, and N. S. Scrutton. Mechanism of coenzyme binding to human methionine synthase reductase revealed through the crystal structure of the fnr-like module and isothermal titration calorimetry. *Biochemistry*, 46(42):11833–11844, 2007. ISSN 0006-2960.

[28] Aldo Gutierrez, Lu-Yun Lian, C. Roland Wolf, Nigel S. Scrutton, and Gordon C. K. Roberts. Stopped-flow kinetic studies of flavin reduction in human cytochrome p450 reductase and its component domains†. *Biochemistry*, 40 (7):1964–1975, 2001. ISSN 0006-2960.

[29] Aldo Gutierrez, Andrew W. Munro, Alex Grunau, C. Roland Wolf, Nigel S. Scrutton, and Gordon C. K. Roberts. Interflavin electron transfer in human cytochrome p450 reductase is enhanced by coenzyme binding. relaxation kinetic studies with coenzyme analogues. *European Journal of Biochemistry*, 270(12):2612–2621, 2003. ISSN 0014-2956 1432-1033.

[30] D. S. Sem and C. B. Kasper. Effect of ionic-strength on the kinetic mechanism and relative rate limitation of steps in the model nadph-cytochrome p450 oxidoreductase reaction with cytochrome-c. *Biochemistry*, 34(39):12768–12774, 1995. ISSN 0006-2960.

[31] J. L. Vermilion, D. P. Ballou, V. Massey, and M. J. Coon. Separate roles for fmn and fad in catalysis by liver microsomal nadph-cytochrome p-450 reductase. *Journal of Biological Chemistry*, 256(1):266–277, 1981. ISSN 0021-9258.

[32] J. L. Vermilion and M. J. Coon. Identification of the high and low potential flavins of liver microsomal nadph-cytochrome p-450 reductase. *Journal of Biological Chemistry*, 253(24):8812–8819, 1978. ISSN 0021-9258.

[33] A. K. Bhattacharyya, J. J. Lipka, L. Waskell, and G. Tollin. Laser flash photolysis studies of the reduction kinetics of nadph:cytochrome p-450 reductase. *Biochemistry*, 30(3):759–65, 1991. ISSN 0006-2960 (Print) 0006-2960.

[34] A. W. Munro, S. Daff, J. R. Coggins, J. G. Lindsay, and S. K. Chapman. Probing electron transfer in flavocytochrome p-450 bm3 and its component domains. *European Journal of Biochemistry*, 239(2):403–409, 1996. ISSN 0014-2956.

[35] A. W. Munro, M. A. Noble, L. Robledo, S. N. Daff, and S. K. Chapman. Determination of the redox properties of human nadph-cytochrome p450 reductase. *Biochemistry*, 40(7):1956–1963, 2001. ISSN 0006-2960.

[36] Freeborn Rwere, Chuanwu Xia, Sangchoul Im, Mohammad Mahfuzul Haque, Dennis J. Stuehr, Lucy Waskell, and Jung-Ja P. Kim. Mutants of cytochrome p450 reductase lacking either gly-141 or gly-143 destabilize its fmn semiquinone. *Journal of Biological Chemistry*, 2016.

[37] S. Brenner, S. Hay, A. W. Munro, and N. S. Scrutton. Inter-flavin electron transfer in cytochrome p450 reductase - effects of solvent and ph identify hidden complexity in mechanism. *FEBS Journal*, 275(18):4540–4557, 2008. ISSN 1742-464X.

[38] R. Huang, M. Zhang, F. Rwere, L. Waskell, and A. Ramamoorthy. Kinetic and structural characterization of the interaction between the fmn binding domain of cytochrome p450 reductase and cytochrome c. *Journal of Biological Chemistry*, 2014. ISSN 0021-9258 1083-351X.

[39] M. B. Murataliev and R. Feyereisen. Mechanism of cytochrome p450 reductase from the house fly: evidence for an fmn semiquinone as electron donor. *FEBS Letters*, 453(1-2):201–204, 1999. ISSN 0014-5793.

[40] W. C. Huang, J. Ellis, P. C. Moody, E. L. Raven, and G. C. Roberts. Redox-linked domain movements in the catalytic cycle of cytochrome p450 reductase. *Structure*, 21(9):1581–9, 2013. ISSN 1878-4186 (Electronic) 0969-2126 (Linking).

[41] P. A. Hubbard, A. L. Shen, R. Paschke, C. B. Kasper, and J. J. P. Kim. Nadph-cytochrome p450 oxidoreductase - structural basis for hydride and electron transfer. *Journal of Biological Chemistry*, 276(31):29163–29170, 2001. ISSN 0021-9258.

[42] C. Xia, D. Hamdane, A. L. Shen, V. Choi, C. B. Kasper, N. M. Pearl, H. Zhang, S. C. Im, L. Waskell, and J. J. Kim. Conformational changes of nadph-cytochrome p450 oxidoreductase are essential for catalysis and cofactor binding. *Journal of Biological Chemistry*, 286(18):16246–60, 2011. ISSN 1083-351X (Electronic) 0021-9258 (Linking).

[43] H. Frauenfelder, S. G. Sligar, and P. G. Wolynes. The energy landscapes and motions of proteins. *Science*, 254(5038):1598–1603, 1991. ISSN 0036-8075.

[44] S. J. Benkovic, G. G. Hammes, and S. Hammes-Schiffer. Free-energy landscape of enzyme catalysis. *Biochemistry*, 47(11):3317–21, 2008. ISSN 0006-2960 (Print) 0006-2960.

[45] E. Z. Eisenmesser, O. Millet, W. Labeikovsky, D. M. Korzhnev, M. Wolf-Watz, D. A. Bosco, J. J. Skalicky, L. E. Kay, and D. Kern. Intrinsic dynamics of an enzyme underlies catalysis. *Nature*, 438(7064):117–121, 2005. ISSN 0028-0836.

[46] K. A. Henzler-Wildman, V. Thai, M. Lei, M. Ott, M. Wolf-Watz, T. Fenn, E. Pozharski, M. A. Wilson, G. A. Petsko, M. Karplus, C. G. Hubner, and D. Kern. Intrinsic motions along an enzymatic reaction trajectory. *Nature*, 450(7171):838–U13, 2007. ISSN 0028-0836.

[47] D. D. Boehr, R. Nussinov, and P. E. Wright. The role of dynamic conformational ensembles in biomolecular recognition. *Nature Chemical Biology*, 5(11): 789–796, 2009. ISSN 1552-4450.

[48] G. Y. Qi and S. Hayward. Database of ligand-induced domain movements in enzymes. *Bmc Structural Biology*, 9:9, 2009. ISSN 1471-2237.

[49] L. Zerrad, A. Merli, G. F. Schroder, A. Varga, E. Graczer, P. Pernot, A. Round, M. Vas, and M. W. Bowler. A spring-loaded release mechanism regulates domain movement and catalysis in phosphoglycerate kinase. *Journal of Biological Chemistry*, 286(16):14040–14048, 2011. ISSN 0021-9258.

[50] D. Taylor, G. Cawley, and S. Hayward. Quantitative method for the assignment of hinge and shear mechanism in protein domain movements. *Bioinformatics*, 30(22):3189–3196, 2014. ISSN 1367-4803.

[51] Elise Delaforge, Sigrid Milles, Guillaume Bouvignies, Denis Bouvier, Stephane Boivin, Nicola Salvi, Damien Maurin, Anne Martel, Adam Round, Edward A. Lemke, Malene Ringkjøbing Jensen, Darren J. Hart, and Martin Blackledge. Large-scale conformational dynamics control h5n1 influenza polymerase pb2 binding to importin . *Journal of the American Chemical Society*, 2015. ISSN 0002-7863.

[52] K. R. Wolthers, C. Levy, N. S. Scrutton, and D. Leys. Large-scale domain dynamics and adenosylcobalamin reorientation orchestrate radical catalysis in ornithine 4,5-aminomutase. *Journal of Biological Chemistry*, 285(18):13942–13950, 2010. ISSN 0021-9258.

[53] Elisabeth Darrouzet, Christopher C. Moser, P. Leslie Dutton, and Fevzi Daldal. Large scale domain movement in cytochrome bc1: a new device for electron transfer in proteins. *Trends in Biochemical Sciences*, 26(7):445–451, 2001. ISSN 0968-0004.

[54] K. Danyal, D. Mayweather, D. R. Dean, L. C. Seefeldt, and B. M. Hoffman. Conformational gating of electron transfer from the nitrogenase fe protein to mofe protein. *J Am Chem Soc*, 132(20):6894–5, 2010. ISSN 1520-5126 (Electronic) 0002-7863 (Linking).

[55] V. L. Davidson. Protein control of true, gated, and coupled electron transfer reactions. *Accounts of Chemical Research*, 41(6):730–8, 2008. ISSN 1520-4898 (Electronic) 0001-4842 (Linking).

[56] H. S. Toogood, D. Leys, and N. S. Scrutton. Dynamics driving function - new insights from electron transferring flavoproteins and partner complexes. *FEBS Journal*, 274(21):5481–5504, 2007. ISSN 1742-464X.

[57] David C. Lamb, Youngchang Kim, Liudmila V. Yermalitskaya, Valery N. Yermalitsky, Galina I. Lepesheva, Steven L. Kelly, Michael R. Waterman, and Larissa M. Podust. A second fmn binding site in yeast nadph-cytochrome p450 reductase suggests a mechanism of electron transfer by diflavin reductases. *Structure*, 14(1):51–61. ISSN 0969-2126.

[58] A. Gutierrez, M. Paine, C. R. Wolf, N. S. Scrutton, and G. C. K. Roberts. Relaxation kinetics of cytochrome p450 reductase: Internal electron transfer is limited by conformational change and regulated by coenzyme binding. *Biochemistry*, 41(14):4626–4637, 2002. ISSN 0006-2960.

[59] A. K. Bhattacharyya, J. K. Hbikbikey, G. Tollin, and L. Waskell. Investigation of the rate limiting step for electron transfer from nadph:cytochrome p450 reductase to cytochrome b5: A laser flash-photolysis study. *Archives of Biochemistry and Biophysics*, 310(2):318–324, 1994. ISSN 0003-9861.

[60] D. Hamdane, C. W. Xia, S. C. Im, H. M. Zhang, J. J. P. Kim, and L. Waskell. Structure and function of an nadph-cytochrome p450 oxidoreductase in an open conformation capable of reducing cytochrome p450. *Journal of Biological Chemistry*, 284(17):11374–11384, 2009. ISSN 0021-9258.

[61] S. Hay, S. Brenner, B. Khara, A. M. Quinn, S. E. J. Rigby, and N. S. Scrutton. Nature of the energy landscape for gated electron transfer in a dynamic redox protein. *Journal of the American Chemical Society*, 132(28):9738–9745, 2010. ISSN 0002-7863.

[62] J. Ellis, A. Gutierrez, I. L. Barsukov, W. C. Huang, J. G. Grossmann, and G. C. Roberts. Domain motion in cytochrome p450 reductase: conformational equilibria revealed by nmr and small-angle x-ray scattering. *Journal of Biological Chemistry*, 284(52):36628–37, 2009. ISSN 1083-351X (Electronic) 0021-9258 (Linking).

[63] C. R. Pudney, B. Khara, L. O. Johannissen, and N. S. Scrutton. Coupled motions direct electrons along human microsomal p450 chains. *Plos Biology*, 9(12):10, 2011. ISSN 1544-9173.

[64] A. Nath, W. M. Atkins, and S. G. Sligar. Applications of phospholipid bilayer nanodiscs in the study of membranes and membrane proteins. *Biochemistry*, 46(8):2059–69, 2007. ISSN 0006-2960 (Print) 0006-2960.

[65] T. H. Bayburt and S. G. Sligar. Single-molecule height measurements on microsomal cytochrome p450 in nanometer-scale phospholipid bilayer disks. *Proceedings of the National Academy of Sciences*, 99(10):6725–6730, 2002. ISSN 0027-8424.

[66] T. H. Bayburt and S. G. Sligar. Membrane protein assembly into nanodiscs. *FEBS Letters*, 584(9):1721–7, 2010. ISSN 0014-5793.

[67] I. G. Denisov and S. G. Sligar. Cytochromes p450 in nanodiscs. *Biochimica et Biophysica Acta*, 1814(1):223–9, 2011. ISSN 0006-3002 (Print) 0006-3002.

[68] M. Wadsater, T. Laursen, A. Singha, N. S. Hatzakis, D. Stamou, R. Barker, K. Mortensen, R. Feidenhans'l, B. L. Moller, and M. Cardenas. Monitoring shifts in the conformation equilibrium of the membrane protein cytochrome p450 reductase (por) in nanodiscs. *Journal of Biological Chemistry*, 287(41): 34596–603, 2012. ISSN 1083-351X (Electronic) 0021-9258 (Linking).

[69] M. Wadsater, R. Barker, K. Mortensen, R. Feidenhans'l, and M. Cardenas. Effect of phospholipid composition and phase on nanodisc films at the solid-liquid interface as studied by neutron reflectivity. *Langmuir*, 29(9):2871–2880, 2013. ISSN 0743-7463.

[70] S. Maric, N. Skar-Gislinge, S. Midtgaard, M. B. Thygesen, J. Schiller, H. Frielinghaus, M. Moulin, M. Haertlein, V. T. Forsyth, T. G. Pomorski, and L. Arleth. Stealth carriers for low-resolution structure determination of membrane proteins in solution. *Acta Crystallographica D Biological Crystallography*, 70 (Pt 2):317–28, 2014. ISSN 0907-4449.

[71] Mohammad M. Haque, Mekki Bayachou, Jesus Tejero, Claire T. Kenney, Naw M. Pearl, Sang-Choul Im, Lucy Waskell, and Dennis J. Stuehr. Distinct conformational behaviors of four mammalian dual-flavin reductases (cytochrome p450 reductase, methionine synthase reductase, neuronal nitric oxide synthase, endothelial nitric oxide synthase) determine their unique catalytic profiles. *FEBS Journal*, 1:1–16, 2014. ISSN 1742-4658.

[72] M. Sugishima, H. Sato, Y. Higashimoto, J. Harada, K. Wada, K. Fukuyama, and M. Noguchi. Structural basis for the electron transfer from an open form of nadph-cytochrome p450 oxidoreductase to heme oxygenase. *Proceedings of the National Academy of Sciences*, 111(7):2524–2529, 2014. ISSN 0027-8424.

[73] D. Nickels J , H. O'Neill, L. Hong, M. Tyagi, G. Ehlers, K. L. Weiss, Q. Zhang, Z. Yi, E. Mamontov, C. Smith J , and P. Sokolov A . Dynamics of protein and its hydration water: Neutron scattering studies on fully deuterated gfp. *Biophysical Journal*, 103(7):1566–75, 2012. ISSN 0006-3495 (Print).

[74] M. Grimaldo, F. Roosen-Runge, N. Jalarvo, M. Zamponi, F. Zanini, M. Hennig, F. Zhang, F. Schreiber, and T. Seydel. *High-resolution neutron spectroscopy on protein solution samples*, volume 83 of *EPJ Web of Conferences*. E D P Sciences, Cedex A, 2015. ISBN 2100-014X.

[75] David Arnlund, Linda C. Johansson, Cecilia Wickstrand, Anton Barty, Garth J. Williams, Erik Malmerberg, Jan Davidsson, Despina Milathianaki, Daniel P. DePonte, Robert L. Shoeman, Dingjie Wang, Daniel James, Gergely Katona, Sebastian Westenhoff, Thomas A. White, Andrew Aquila, Sadia Bari, Peter Berntsen, Mike Bogan, Tim Brandt van Driel, R. Bruce Doak, Kasper Skov Kjaer, Matthias Frank, Raimund Fromme, Ingo Grotjohann, Robert Henning, Mark S. Hunter, Richard A. Kirian, Irina Kosheleva, Christopher Kupitz, Mengning Liang, Andrew V. Martin, Martin Meedom Nielsen,

Marc Messerschmidt, M. Marvin Seibert, Jennie Sjohamn, Francesco Stellato, Uwe Weierstall, Nadia A. Zatsepin, John C. H. Spence, Petra Fromme, Ilme Schlichting, Sebastien Boutet, Gerrit Groenhof, Henry N. Chapman, and Richard Neutze. Visualizing a protein quake with time-resolved x-ray scattering at a free-electron laser. *Nature Methods*, 11(9):923–926, 2014.

[76] T. R. M. Barends, L. Foucar, S. Botha, R. B. Doak, R. L. Shoeman, K. Nass, J. E. Koglin, G. J. Williams, S. Boutet, M. Messerschmidt, and I. Schlichting. De novo protein crystal structure determination from x-ray free-electron laser data. *Nature*, 505(7482):244–+, 2014. ISSN 0028-0836.

[77] G. K. Feld and M. Frank. Enabling membrane protein structure and dynamics with x-ray free electron lasers. *Current Opinion in Structural Biology*, 27:69–78, 2014. ISSN 0959-440X.

[78] J. Hattne, N. Echols, R. Tran, J. Kern, R. J. Gildea, A. S. Brewster, R. Alonso-Mori, C. Glockner, J. Hellmich, H. Laksmono, R. G. Sierra, B. Lassalle-Kaiser, A. Lampe, G. Han, S. Gul, D. DiFiore, D. Milathianaki, A. R. Fry, A. Miahnahri, W. E. White, D. W. Schafer, M. M. Seibert, J. E. Koglin, D. Sokaras, T. C. Weng, J. Sellberg, M. J. Latimers, P. Glatzel, P. H. Zwart, R. W. Grosse-Kunstleve, M. J. Bogan, M. Messerschmidt, G. J. Williams, S. Boutet, J. Messinger, A. Zouni, J. Yano, U. Bergmann, V. K. Yachandra, P. D. Adams, and N. K. Sauter. Accurate macromolecular structures using minimal measurements from x-ray free-electron lasers. *Nature Methods*, 11(5):545–548, 2014. ISSN 1548-7091.

[79] 2016. URL `https://www.ill.eu/.../instruments/d22`.

[80] Ashley Jordan, Mark Jacques, Catherine Merrick, Juliette Devos, V. Trevor Forsyth, Lionel Porcar, and Anne Martel. Sec-sans: size exclusion chromatography combined in situ with small-angle neutron scatteringthis article will form part of a virtual special issue of the journal, presenting some highlights of the 16th international conference on small-angle scattering (sas2015). *Journal of Applied Crystallography*, 49(6), 2016. ISSN 1600-5767.

[81] Petra Pernot, Adam Round, Ray Barrett, Alejandro De Maria Antolinos, Alexandre Gobbo, Elspeth Gordon, Julien Huet, Jerôme Kieffer, Mario Lentini, Muriel Mattenet, Christian Morawe, Christoph Mueller-Dieckmann, Staffan Ohlsson, Werner Schmid, John Surr, Pascal Theveneau, Louiza Zerrad, and Sean McSweeney. Upgraded esrf bm29 beamline for saxs on macromolecules in solution. *Journal of Synchrotron Radiation*, 20(Pt 4):660–664, 2013. ISSN 0909-0495 1600-5775.

[82] M. C. Corbett, M. J. Latimer, T. L. Poulos, I. F. Sevrioukova, K. O. Hodgson, and B. Hedman. Photoreduction of the active site of the metalloprotein putidaredoxin by synchrotron radiation. *Acta Crystallographica D Biological Crystallography*, 63(Pt 9):951–60, 2007. ISSN 0907-4449 (Print) 0907-4449 (Linking).

[83] E. F. Garman and M. Weik. Radiation damage to biological macromolecules: some answers and more questions. *Journal of Synchrotron Radiation*, 20:1–6, 2013. ISSN 0909-0495.

[84] S. P. Meisburger, M. Warkentin, H. Chen, J. B. Hopkins, R. E. Gillilan, L. Pollack, and R. E. Thorne. Breaking the radiation damage limit with cryo-saxs. *Biophysical Journal*, 104(1):227–36, 2013. ISSN 1542-0086 (Electronic) 0006-3495 (Linking).

[85] R. L. Owen, E. Rudino-Pinera, and E. F. Garman. Experimental determination of the radiation dose limit for cryocooled protein crystals. *Proceedings of the National Academy of Sciences*, 103(13):4912–4917, 2006. ISSN 0027-8424.

[86] O. B. Zeldin, S. Brockhauser, J. Bremridge, J. M. Holton, and E. F. Garman. Predicting the x-ray lifetime of protein crystals. *Proceedings of the National Academy of Sciences*, 110(51):20551–20556, 2013. ISSN 0027-8424.

[87] H. P. Hersleth and K. K. Andersson. How different oxidation states of crystalline myoglobin are influenced by x-rays. *Biochimica et Biophysica Acta*, 1814(6):785–96, 2011. ISSN 0006-3002 (Print) 0006-3002 (Linking).

[88] W. H. Bragg and W. L. Bragg. The reflection of x-rays by crystals. *Proceedings of the Royal Society of London. Series A*, 88(605):428, 1913.

[89] D. A. Jacques and J. Trewhella. Small-angle scattering for structural biology–expanding the frontier while avoiding the pitfalls. *Protein Sci*, 19(4):642–57, 2010. ISSN 1469-896X (Electronic) 0961-8368 (Linking).

[90] D. A. Jacques, J. M. Guss, D. I. Svergun, and J. Trewhella. Publication guidelines for structural modelling of small-angle scattering data from biomolecules in solution. *Acta Crystallographica D Biological Crystallography*, 68(Pt 6): 620–6, 2012. ISSN 1399-0047 (Electronic) 0907-4449 (Linking).

[91] B.; Jacrot. The study of biological structures by neutron scattering from solution. *Reports on Progress in Physics*, 36(63):911–953, 1976.

[92] Bernard Jacrot and Giuseppe Zaccai. Determination of molecular weight by neutron scattering. *Biopolymers*, 20(11):2413–2426, 1981. ISSN 1097-0282.

[93] R. P. Rambo and J. A. Tainer. Accurate assessment of mass, models and resolution by small-angle scattering. *Nature*, 496(7446):477–81, 2013. ISSN 1476-4687 (Electronic) 0028-0836 (Linking).

[94] M. Haertlein, M. Moulin, J. M. Devos, V. Laux, O. Dunne, and V. T. Forsyth. Biomolecular deuteration for neutron structural biology and dynamics. *Methods Enzymol*, 566:113–57, 2016. ISSN 0076-6879.

[95] Michael Haertlein, Martine Moulin, Juliette M. Devos, Valerie Laux, Orla Dunne, and V. Trevor Forsyth. *Chapter Five - Biomolecular Deuteration for Neutron Structural Biology and Dynamics*, volume Volume 566, pages 113–157. Academic Press, 2016. ISBN 0076-6879.

[96] A. Guinier and G. Fournet. Small angle scattering of x-rays. a. guinier and g. fournet. translated by c. b. wilson and with a bibliographical appendix by k. l. yudowitch. wiley, new york, 1955. 268 pp. *Journal of Polymer Science*, 19 (93):594–594, 1956. ISSN 1542-6238.

[97] R. P. Rambo and J. A. Tainer. Characterizing flexible and intrinsically unstructured biological macromolecules by sas using the porod-debye law. *Biopolymers*, 95(8):559–71, 2011. ISSN 0006-3525 (Print) 0006-3525.

[98] O. Glatter. A new method for the evaluation of small-angle scattering data. *Journal of Applied Crystallography*, 10(5):415–421, 1977. ISSN 0021-8898.

[99] Vladimir V. Volkov and Dmitri I. Svergun. Uniqueness of ab initio shape determination in small-angle scattering. *Journal of Applied Crystallography*, 36(3 Part 1):860–864, 2003. ISSN 0021-8898.

[100] D. I. Svergun and H. B. Stuhrmann. New developments in direct shape determination from small-angle scattering. 1. theory and model calculations. *Acta Crystallographica Section A*, 47(6):736–744, 1991. ISSN 0108-7673.

[101] G. Tria, H. D. T. Mertens, M. Kachala, and D. I. Svergun. Advanced ensemble modelling of flexible macromolecules using x-ray solution scattering. *Iucrj*, 2: 207–217, 2015. ISSN 2052-2525.

[102] A. Panjkovich and D. I. Svergun. Saspy: a pymol plugin for manipulation and refinement of hybrid models against small angle x-ray scattering data. *Bioinformatics*, 32(13):2062–4, 2016. ISSN 1367-4803.

[103] M. Pelikan, G. L. Hura, and M. Hammel. Structure and flexibility within proteins as identified through small angle x-ray scattering. *General Physiology and Biophysics*, 28(2):174–189, 2009. ISSN 0231-5882.

[104] Petr V. Konarev, Maxim V. Petoukhov, and Dmitri I. Svergun. Rapid automated superposition of shapes and macromolecular models using spherical harmonics. *Journal of Applied Crystallography*, 49(3):953–960, 2016. ISSN 1600-5767.

[105] M. V. Petoukhov and D. I. Svergun. Analysis of x-ray and neutron scattering from biomacromolecular solutions. *Current Opinion in Structural Biology*, 17 (5):562–571, 2007. ISSN 0959-440X.

[106] D. Schneidman-Duhovny, M. Hammel, and A. Sali. Foxs: a web server for rapid computation and fitting of saxs profiles. *Nucleic Acids Research*, 38: W540–W544, 2010. ISSN 0305-1048.

[107] A. Gutierrez, O. Doehr, M. Paine, C. R. Wolf, N. S. Scrutton, and G. C. K. Roberts. Trp-676 facilitates nicotinamide coenzyme exchange in the reductive half-reaction of human cytochrome p450 reductase: Properties of the soluble w676r and w676a mutant reductases. *Biochemistry*, 39(51):15990–15999, 2000. ISSN 0006-2960.

[108] M. Mujacic, K. W. Cooper, and F. Baneyx. Cold-inducible cloning vectors for low-temperature protein expression in escherichia coli: application to the production of a toxic and proteolytically sensitive fusion protein. *Gene*, 238 (2):325–332, 1999. ISSN 0378-1119.

[109] 2013. URL `http://protcalc.sourceforge.net/`.

[110] Alex Grunau, Mark J. Paine, John E. Ladbury, and Aldo Gutierrez. Global effects of the energetics of coenzyme binding: nadph controls the protein interaction properties of human cytochrome p450 reductase†. *Biochemistry*, 45 (5):1421–1434, 2006. ISSN 0006-2960.

[111] Uniprot: a hub for protein information. *Nucleic Acids Res*, 43(Database issue): D204–12, 2015. ISSN 0305-1048.

[112] M. Jenner, J. Ellis, W. C. Huang, E. L. Raven, G. C. K. Roberts, and N. J. Oldham. Detection of a protein conformational equilibrium by electrospray ionisation-ion mobility-mass spectrometry. *Angewandte Chemie-International Edition*, 50(36):8291–8294, 2011. ISSN 1433-7851.

[113] A. Grunau, K. Geraki, J. G. Grossmann, and A. Gutierrez. Conformational dynamics and the energetics of protein–ligand interactions: role of interdomain loop in human cytochrome p450 reductase. *Biochemistry*, 46(28):8244–55, 2007. ISSN 0006-2960 (Print) 0006-2960 (Linking).

[114] D. Schneidman-Duhovny, M. Hammel, J. A. Tainer, and A. Sali. Foxs, foxsdock and multifoxs: Single-state and multi-state structural modeling of proteins and their complexes based on saxs profiles. *Nucleic Acids Res*, 44(W1): W424–9, 2016. ISSN 0305-1048.

[115] D. I. Svergun, S. Richard, M. H. Koch, Z. Sayers, S. Kuprin, and G. Zaccai. Protein hydration in solution: experimental observation by x-ray and neutron scattering. *Proceedings of the National Academy of Sciences*, 95(5):2267–72, 1998. ISSN 0027-8424 (Print) 0027-8424.

[116] H. H. Jang, A. P. Jamakhandi, S. Z. Sullivan, C. H. Yun, P. F. Hollenberg, and G. P. Miller. Beta sheet 2-alpha helix c loop of cytochrome p450 reductase serves as a docking site for redox partners. *Biochimica Et Biophysica Acta-Proteins and Proteomics*, 1804(6):1285–1293, 2010. ISSN 1570-9639.

[117] Oriane Frances, Fataneh Fatemi, Denis Pompon, Eric Guittet, Christina Sizun, Javier Pérez, Ewen Lescop, and Gilles Truan. A well-balanced preexisting equilibrium governs electron flux efficiency of a multidomain diflavin reductase. *Biophysical Journal*, 108(6):1527–1536, 2015. ISSN 00063495.

[118] M. Hammel. Validation of macromolecular flexibility in solution by small-angle x-ray scattering (saxs). *Eur Biophysical Journal*, 41(10):789–99, 2012. ISSN 0175-7571.

[119] B. Vincent, N. Morellet, F. Fatemi, L. Aigrain, G. Truan, E. Guittet, and E. Lescop. The closed and compact domain organization of the 70-kda human cytochrome p450 reductase in its oxidized state as revealed by nmr. *Journal of Molecular Biology*, 420(4-5):296–309, 2012. ISSN 0022-2836.

[120] Elizaveta A. Kovrigina, Brian Pattengale, Chuanwu Xia, Azamat R. Galiakhmetov, Jier Huang, Jung-Ja P. Kim, and Evgenii L. Kovrigin. Conformational states of cytochrome p450 oxidoreductase evaluated by förster resonance energy transfer using ultrafast transient absorption spectroscopy. *Biochemistry*, 2016. ISSN 0006-2960.

[121] M. L. Ludwig, K. A. Pattridge, A. L. Metzger, M. M. Dixon, M. Eren, Y. C. Feng, and R. P. Swenson. Control of oxidation-reduction potentials in flavodoxin from clostridium beijerinckii: The role of conformation changes. *Biochemistry*, 36(6):1259–1280, 1997. ISSN 0006-2960.

[122] D. M. Hoover, C. L. Drennan, A. L. Metzger, C. Osborne, C. H. Weber, K. A. Pattridge, and M. L. Ludwig. Comparisons of wild-type and mutant flavodoxins from anacystis nidulans. structural determinants of the redox potentials. *Journal of Molecular Biology*, 294(3):725–743, 1999. ISSN 0022-2836.

[123] Q. Bashir, S. Scanu, and M. Ubbink. Dynamics in electron transfer protein complexes. *FEBS Journal*, 278(9):1391–400, 2011. ISSN 1742-4658 (Electronic) 1742-464X (Linking).

[124] J. Schilder and M. Ubbink. Formation of transient protein complexes. *Current Opinion in Structural Biology*, 23(6):911–8, 2013. ISSN 1879-033X (Electronic) 0959-440X (Linking).

[125] S. Ahuja, N. Jahr, S. C. Im, S. Vivekanandan, N. Popovych, S. V. Le Clair, R. Huang, R. Soong, J. Xu, K. Yamamoto, R. P. Nanga, A. Bridges, L. Waskell, and A. Ramamoorthy. A model of the membrane-bound cytochrome b5-cytochrome p450 complex from nmr and mutagenesis data. *Journal of Biological Chemistry*, 288(30):22080–95, 2013. ISSN 0021-9258.

[126] J. A. Worrall, Y. Liu, P. B. Crowley, J. M. Nocek, B. M. Hoffman, and M. Ubbink. Myoglobin and cytochrome b5: a nuclear magnetic resonance study of a highly dynamic protein complex. *Biochemistry*, 41(39):11721–30, 2002. ISSN 0006-2960 (Print) 0006-2960.

[127] S. Deep, S. C. Im, E. R. Zuiderweg, and L. Waskell. Characterization and calculation of a cytochrome c-cytochrome b5 complex using nmr data. *Biochemistry*, 44(31):10654–68, 2005. ISSN 0006-2960 (Print) 0006-2960.

[128] A. N. Volkov. Structure and function of transient encounters of redox proteins. *Accounts of Chemical Research*, 48(12):3036–43, 2015. ISSN 1520-4898 (Electronic) 0001-4842 (Linking).

[129] A. N. Volkov, J. A. Worrall, E. Holtzmann, and M. Ubbink. Solution structure and dynamics of the complex between cytochrome c and cytochrome c peroxidase determined by paramagnetic nmr. *Proceedings of the National Academy of Sciences*, 103(50):18945–50, 2006. ISSN 0027-8424 (Print) 0027-8424.

[130] B. L. Horecker. Triphosphopyridine nucleotide-cytochrome c reductase in liver. *Journal of Biological Chemistry*, 183:593–605, 1950.

[131] Y. Farooq and G. C. Roberts. Kinetics of electron transfer between nadph-cytochrome p450 reductase and cytochrome p450 3a4. *Biochem J*, 432(3): 485–93, 2010. ISSN 1470-8728 (Electronic) 0264-6021 (Linking).

[132] Denisov I. Schlichting I. Makris, T.M. and S.G. Sligar. *Activation of molecular oxygen by cytochrome P450*, pages 149–182. Kluwer Academic / Plenum, New York, 3rd. edition, 2005.

[133] D. R. Davydov, B. V. Darovsky, I. R. Dedinsky, I. P. Kanaeva, G. I. Bachmanova, V. M. Blinov, and A. I. Archakov. Cytochrome c (fe2+) as a competitive inhibitor of nadph-dependent reduction of cytochrome p450 lm2: locating protein-protein interaction sites in microsomal electron carriers. *Arch Biochem Biophys*, 297(2):304–13, 1992. ISSN 0003-9861 (Print) 0003-9861.

[134] P. P. Tamburini and J. B. Schenkman. Differences in the mechanism of functional interaction between nadph-cytochrome p-450 reductase and its redox partners. *Molecular Pharmacology*, 30(2):178–85, 1986. ISSN 0026-895X (Print) 0026-895x.

[135] G. W. Bushnell, G. V. Louie, and G. D. Brayer. High-resolution three-dimensional structure of horse heart cytochrome c. *Journal of Molecular Biology*, 214(2):585–95, 1990. ISSN 0022-2836 (Print) 0022-2836.

[136] Jamakhandi A.P. Sullivan S.Z. Yun C.-H. Hollenberg P.F. Miller G.P. Jang, H.-H. Beta sheet 2–alpha helix c loop of cytochrome p450 reductase serves as a docking site for redox partners. *Biochimica et Biophysica Acta*, 1804(6): 1285–93, 2010.

[137] A. L. Shen and C. B. Kasper. Role of acidic residues in the interaction of nadph-cytochrome p450 oxidoreductase with cytochrome p450 and cytochrome c. *Journal of Biological Chemistry*, 270(46):27475–80, 1995.

[138] Q. Zhao, S. Modi, G. Smith, M. Paine, P. D. McDonagh, C. R. Wolf, D. Tew, L. Y. Lian, G. C. K. Roberts, and H. P. C. Driessen. Crystal structure of the fmn-binding domain of human cytochrome p450 reductase at 1.93 angstrom resolution. *Protein Science*, 8(2):298–306, 1999. ISSN 0961-8368.

[139] G. C. P. van Zundert, J. P. G. L. M. Rodrigues, M. Trellet, C. Schmitz, P. L. Kastritis, E. Karaca, A. S. J. Melquiond, M. van Dijk, S. J. de Vries, and A. M. J. J. Bonvin. The haddock2.2 web server: User-friendly integrative modeling of biomolecular complexes. *Journal of Molecular Biology*, 428(4): 720–725, 2016. ISSN 0022-2836.

[140] D. Russel, K. Lasker, B. Webb, J. Velazquez-Muriel, E. Tjioe, D. Schneidman-Duhovny, B. Peterson, and A. Sali. Putting the pieces together: Integrative modeling platform software for structure determination of macromolecular assemblies. *Plos Biology*, 10(1):5, 2012. ISSN 1545-7885.

[141] H. Ihee, M. Lorenc, T. K. Kim, Q. Y. Kong, M. Cammarata, J. H. Lee, S. Bratos, and M. Wulff. Ultrafast x-ray diffraction of transient molecular structures in solution. *Science*, 309(5738):1223, 2005.

[142] T. Reusch, D. D. Mai, M. Osterhoff, D. Khakhulin, M. Wulff, and T. Salditt. Nonequilibrium collective dynamics in photoexcited lipid multilayers by time resolved diffuse x-ray scattering. *Physical Review Letters*, 111(26):268101, 2013.

[143] M. Sander, M. Herzog, J. E Pudell, M. Bargheer, N. Weinkauf, M. Pedersen, G. Newby, J. Sellmann, J. Schwarzkopf, V. Besse, V. V Temnov, and P. Gaal.

Spatiotemporal coherent control of thermal excitations in solids. *Physical Review Letters*, 119(7):075901, 2017.

[144] Marco Cammarata, Matteo Levantino, Friedrich Schotte, Philip A. Anfinrud, Friederike Ewald, Jungkweon Choi, Antonio Cupane, Michael Wulff, and Hyotcherl Ihee. Tracking the structural dynamics of proteins in solution using time-resolved wide-angle x-ray scattering. *Nature Methods*, 5(10):881–886, 2008.

[145] Erik Malmerberg, Ziad Omran, Jochen S Hub, Xuewen Li, Gergely Katona, Sebastian Westenhoff, Linda C Johansson, Magnus Andersson, Marco Cammarata, Michael Wulff, David van der Spoel, Jan Davidsson, Alexandre Specht, and Richard Neutze. Time-resolved waxs reveals accelerated conformational changes in iodoretinal-substituted proteorhodopsin. *Biophysical Journal*, 101(6):1345–1353, 2011. ISSN 0006-3495.

[146] Jong Goo Kim, Tae Wu Kim, Jeongho Kim, and Hyotcherl Ihee. Protein structural dynamics revealed by time-resolved x-ray solution scattering. *Accounts of Chemical Research*, 48(8):2200–2208, 2015. ISSN 0001-4842.

[147] Annemarie B. Wöhri, Gergely Katona, Linda C. Johansson, Emelie Fritz, Erik Malmerberg, Magnus Andersson, Jonathan Vincent, Mattias Eklund, Marco Cammarata, Michael Wulff, Jan Davidsson, Gerrit Groenhof, and Richard Neutze. Light-induced structural changes in a photosynthetic reaction center caught by laue diffraction. *Science*, 328(5978):630, 2010.

[148] Oskar Berntsson, Ralph P. Diensthuber, Matthijs R. Panman, Alexander Björling, Ashley J. Hughes, Léocadie Henry, Stephan Niebling, Gemma Newby, Marianne Liebi, Andreas Menzel, Robert Henning, Irina Kosheleva, Andreas Möglich, and Sebastian Westenhoff. Time-resolved x-ray solution scattering reveals the structural photoactivation of a light-oxygen-voltage photoreceptor. *Structure*, 25(6):933–938.e3, 2017. ISSN 0969-2126.

[149] Derren J. Heyes, Anne-Marie Quinn, Paul M. Cullis, Michael Lee, Andrew W. Munro, and Nigel S. Scrutton. Internal electron transfer in multi-site redox enzymes is accessed by laser excitation of thiouredopyrene-3,6,8-trisulfonate (tups). *Chemical Communications*, (9):1124–1126, 2009. ISSN 1359-7345.

[150] A. Kotlyar, N. Borovok, M. Hazani, I. Szundi, and O. Einarsdottir. Photoinduced intracomplex electron transfer between cytochrome c oxidase and tups-modified cytochrome c. *European Journal of Biochemistry*, 267(18):5805–5809, 2000. ISSN 0014-2956.

[151] Alexander B. Kotlyar, Natalia Borovok, and Miron Hazani. Use of thiouredopyrenetrisulfonate photochemistry for driving electron transfer reactions in aqueous solutions. *Biochemistry*, 36(50):15823–15827, 1997. ISSN 0006-2960.

[152] K. C. Liu, J. M. X. Hughes, S. Hay, and N. S. Scrutton. Liver microsomal lipid enhances the activity and redox coupling of colocalized cytochrome p450 reductase-cytochrome p450 3a4 in nanodiscs. *FEBS Journal*, 284(14):2302–2319, 2017. ISSN 1742-464x.

[153] Werner Kühlbrandt. Cryo-em enters a new era. *eLife*, 3:e03678, 2014. ISSN 2050-084X.

[154] Cosma Dellisanti. A barrier-breaking resolution. *Nature Structural and Molecular Biology*, 22(5):361–361, 2015. ISSN 1545-9993.

[155] Basil J. Greber, Thi Hoang Duong Nguyen, Jie Fang, Pavel V. Afonine, Paul D. Adams, and Eva Nogales. The cryo-electron microscopy structure of human transcription factor iih. *Nature*, 549(7672):414–417, 2017. ISSN 0028-0836.

[156] Steven Kline. Reduction and analysis of sans and usans data using igor pro. *Journal of Applied Crystallography*, 39(6):895–900, 2006. ISSN 0021-8898.

[157] Maxim V. Petoukhov, Daniel Franke, Alexander V. Shkumatov, Giancarlo Tria, Alexey G. Kikhney, Michal Gajda, Christian Gorba, Haydyn D. T. Mertens, Petr V. Konarev, and Dmitri I. Svergun. New developments in the atsas program package for small-angle scattering data analysis. *Journal of Applied Crystallography*, 45(2):342–350, 2012. ISSN 0021-8898.

[158] Petr V. Konarev, Vladimir V. Volkov, Anna V. Sokolova, Michel H. J. Koch, and Dmitri I. Svergun. Primus: a windows pc-based system for small-angle scattering data analysis. *Journal of Applied Crystallography*, 36(5):1277–1282, 2003. ISSN 0021-8898.

[159] D. Svergun. Determination of the regularization parameter in indirect-transform methods using perceptual criteria. *Journal of Applied Crystallography*, 25(4):495–503, 1992. ISSN 0021-8898.

[160] Daniel Franke and Dmitri I. Svergun. Dammif, a program for rapid ab-initio shape determination in small-angle scattering. *Journal of Applied Crystallography*, 42(2):342–346, 2009. ISSN 0021-8898.

Part IV

Publications and List of Activities

SCIENTIFIC REPORTS

OPEN

Orchestrated Domain Movement in Catalysis by Cytochrome P450 Reductase

Received: 17 May 2017
Accepted: 31 July 2017
Published online: 29 August 2017

Samuel L. Freeman[1,2], Anne Martel[2], Emma L. Raven[1] & Gordon C. K. Roberts[3]

NADPH-cytochrome P450 reductase is a multi-domain redox enzyme which is a key component of the P450 mono-oxygenase drug-metabolizing system. We report studies of the conformational equilibrium of this enzyme using small-angle neutron scattering, under conditions where we are able to control the redox state of the enzyme precisely. Different redox states have a profound effect on domain orientation in the enzyme and we analyse the data in terms of a two-state equilibrium between compact and extended conformations. The effects of ionic strength show that the presence of a greater proportion of the extended form leads to an enhanced ability to transfer electrons to cytochrome *c*. Domain motion is intrinsically linked to the functionality of the enzyme, and we can define the position of the conformational equilibrium for individual steps in the catalytic cycle.

The concept of an energy landscape for a folded protein requires that proteins exist as an equilibrium population of conformational states. Interconversions between these states are of fundamental importance to biological function[1–4], but remain incompletely understood. Internal motions in proteins range from bond vibrations through local loop movements to large-scale domain motion and occur across an extremely wide range of time scales (femtoseconds to seconds). The choreography of local loop motions in the catalytic cycle has been studied in some enzymes[5–8], but in other instances much larger-scale movements of whole domains are important[9–11]. This is particularly true in electron transfer pathways; electron transfer (ET) is generally carried out by proteins associated in large dynamic complexes, and in such systems domain motion can be required to provide access for the protein partner(s) to the redox centre(s)[12–15].

An important family of ET proteins which depends on domain movement in this way is that of the diflavin reductases[16], which includes cytochrome P450 reductase (CPR; Fig. 1)[17–19], mammalian nitric oxide synthase (NOS)[20,21], the cancer-related novel reductase 1[22], and methionine synthase reductase[23,24], as well as the bacterial proteins sulfite reductase[25] and CYP BM3[26]. These enzymes (or their reductase components) have three domains: an FMN-binding domain, related to flavodoxins, an FAD- and NADPH-binding domain, related to ferredoxin/flavodoxin reductases, and a 'linker' domain, which may serve to position the other two domains. The FMN domain is connected to the linker and FAD domains through a highly flexible 'hinge'. In all the members of this family the ET pathway involves the sequence NADPH → FAD → FMN → acceptor, and there is good evidence from mutagenesis and kinetic experiments for motion of the FMN-binding domain to allow it to accept electrons from the FAD and deliver them to the acceptor[18,20,21,27–29].

CPR is located on the endoplasmic reticulum where it is a key component of the P450 mono-oxygenase system which plays a central role in drug metabolism[18], and in the biosynthesis of secondary metabolites in plants[30]. In man, polymorphisms or mutations in CPR can lead to changes in drug metabolism[31,32], and to disordered steroidogenesis and skeletal malformations[33,34]. The conformation of truncated soluble CPR seen by X-ray crystallography[17,19] (Fig. 1) is well suited for rapid electron transfer from FAD to FMN, as the two isoalloxazine rings are ~4 Å apart. However, ET between the FAD and FMN co-factors is in fact relatively slow (10–60 s^{-1})[27,28,35,36], suggesting that the interflavin ET is 'gated'. Furthermore, in the CPR conformation seen in the crystal it is difficult to see how cytochrome P450 (or cytochrome *c*, widely used as a surrogate redox partner for studies in solution) could approach close enough to the FMN for ET to occur[16,18].

[1]Department of Chemistry and Leicester Institute of Structural and Chemical Biology, University of Leicester, Henry Wellcome Building, Lancaster Road, Leicester, LE1 7RH, UK. [2]Institut Laue-Langevin, 71 avenue des Martyrs, 38000, Grenoble, France. [3]Department of Molecular & Cell Biology and Leicester Institute of Structural and Chemical Biology, University of Leicester, Henry Wellcome Building, Lancaster Road, Leicester, LE1 7RH, UK. Correspondence and requests for materials should be addressed to E.L.R. (email: emma.raven@le.ac.uk) or G.C.K.R. (email: gcr@le.ac.uk)

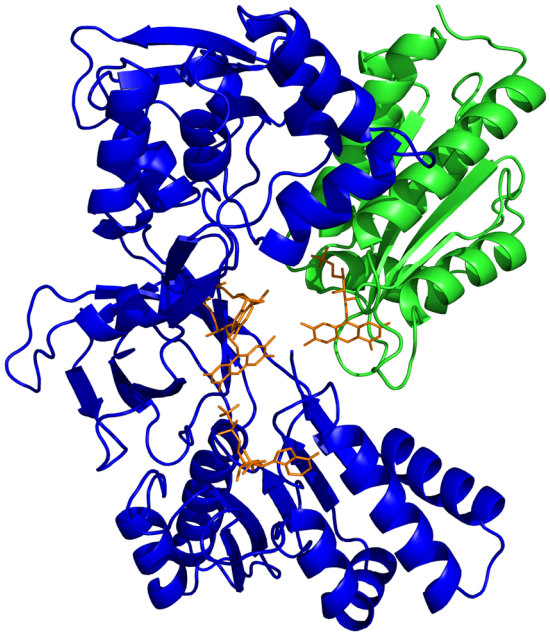

Figure 1. Crystal structure of human CPR in the oxidised state[19]; the FMN-binding domain is in green, the FAD-binding and linker domains in blue and the cofactors are shown as orange sticks.

There is thus evidence for the existence of domain motion in CPR and for its importance in catalysis[16,18,28,37,38], but it remains to be established precisely where in the reaction cycle it occurs. To address this question we examine the conformational equilibrium of CPR in solution using small-angle neutron scattering (SANS) and transient kinetics. The power of solution scattering in studying domain organisation in proteins is well established; by using SANS rather than SAXS we are able to control the redox state of the enzyme precisely without the problems associated with reduction of the flavins by X-ray-induced photo-electrons[37]. These experiments allow us to relate the domain movement to individual steps in the catalytic cycle of the enzyme.

Results

Effects of redox state on CPR conformation. Figure 2a,b shows the intraparticle distance distribution function, P(*r*), derived from the neutron scattering (SANS) curves, for each state of the enzyme studied, while Table 1 summarises the radii of gyration, R_g, and the maximum dimensions, D_{max}, for each state. (The scattering curves and the derived Guinier plots are shown in the Supplementary Material; Supplementary Figure 2).

To separate the effects of coenzyme binding and of flavin reduction, we studied the effects of reduction of CPR by dithionite as well as by NADPH. It is clear from Fig. 2 and Table 1 that reduction of CPR with dithionite leads to an elongation of the average shape of the enzyme, with increases in the observed R_g and D_{max} and the appearance of a clear 'tail' on the distance distribution function. This is true for all the levels of reduction studied, with significant differences between a number of the reduced species. The largest effect in terms of R_g is seen for reduction by dithionite to the 2-electron level, corresponding to the CPR^{2e-} intermediate in the catalytic cycle (see Fig. 5 below). By contrast, reduction to the 2-electron level with NADPH, corresponding to the CPR^{2e-} $NADP^+$ intermediate, has a smaller effect on the shape of the enzyme; essentially the same results are obtained for NADPH-reduced CPR and for dithionite-reduced CPR with bound $NADP^+$, showing that coenzyme binding makes the reduced enzyme more compact. These changes in shape on reduction and on coenzyme binding are illustrated in Fig. 2c,d by *ab initio* low-resolution models calculated from the scattering curves.

The results presented in Fig. 2 and Table 1 are averages over the conformational ensemble of the enzyme and the models in Fig. 2c,d do not necessarily represent single conformations. In view of the evidence cited above that CPR exists in solution as a mixture of conformational states, we have investigated whether the SANS data are better explained by such mixtures. Because of the limited information content of scattering curves and the danger of 'over-parameterisation', we adopt a parsimonious approach, exploring the possibility that just two conformations could fit the data adequately. Using a modification of the program MultiFoXS[39,40], a pool of 10,000 conformations of CPR was generated and MultiFoXS was used to select from this the single conformation or the mixture of 2, 3, … conformations which best fit the SANS data. Figure 3a–c shows that a mixture of 2 conformations was able to fit the scattering curve for $2e^-$-reduced CPR much better than a single conformation, while little improvement in fit was obtained by using a mixture of 3 conformations.

We next attempted to fit the data by using specific structural models. The compact state was represented by the crystal structure of soluble (N-terminally truncated) oxidised human CPR[19]; the R_g value calculated from this structure using CRYSON[41] is 24.88 Å. To represent the more extended state we used either the model we described earlier[37] (calculated R_g 30.36 Å), which was based on NMR and SAXS data on wild-type CPR, or the crystal structure of the ΔTGEE mutant of CPR, which has a deletion in the flexible hinge[42] (PDB 3ES9); in

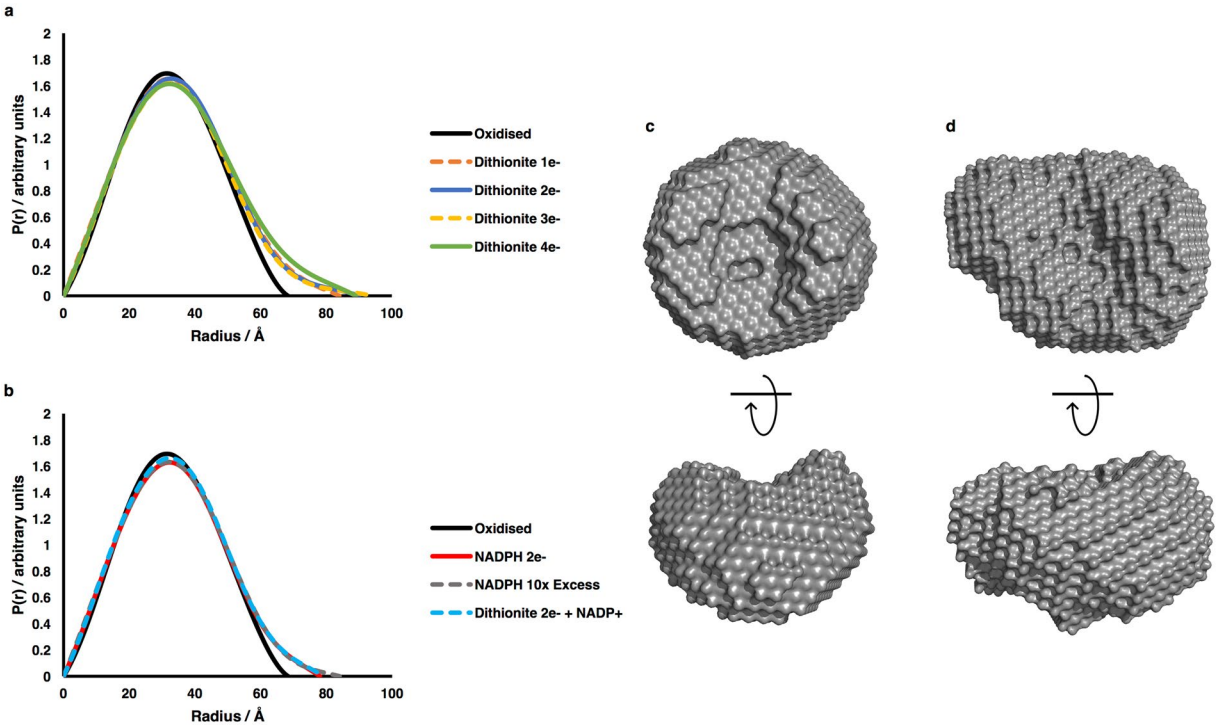

Figure 2. Structural information from SANS data on the different redox states of CPR. (**a**,**b**) Pairwise distance distribution functions; (**a**) samples reduced with dithionite; (**b**) samples reduced with NADPH. The longer 'tail' on the distribution functions for the reduced states as compared to the oxidised state demonstrates a more extended average conformation. (**c**,**d**) *ab initio* envelopes calculated using DAMMIF from the scattering curves of (**c**) oxidised CPR and (**d**) CPR reduced to the $2e^-$ level with dithionite; in (**c** and **d**) the lower envelopes have been rotated 90° about the horizontal axis.

Sample	Hydrodynamic parameters		Two-state Models[a]					
	R_g, Å	D_{max}[b], Å	Crystal structure + Huang *et al.* model			Crystal structure + ΔTGEE mutant model		
			$f_{compact}$[c]	$f_{extended}$[d]	χ^2	$f_{compact}$[c]	$f_{extended}$[d]	χ^2
Oxidised	24.7 ± 0.1	71	0.90	0.10	1.64	0.90	0.10	1.75
Dithionite $1e^-$-reduced	27.6 ± 0.6	84	0.67	0.33	3.12	0.48	0.52	1.99
Dithionite $2e^-$-reduced	28.6 ± 0.4	90	0.61	0.39	3.27	0.56	0.44	1.81
Dithionite $3e^-$-reduced	27.6 ± 0.5	94	0.69	0.31	2.25	0.59	0.41	1.87
Dithionite $4e^-$-reduced	27.6 ± 0.5	89	0.66	0.34	2.64	0.54	0.46	2.03
Dithionite $2e^-$-reduced + $NADP^+$	26.8 ± 0.4	79	0.70	0.30	2.55	0.59	0.41	2.21
NADPH 1 equiv. ($2e^-$-reduced)	27.1 ± 0.4	78	0.69	0.31	2.74	0.55	0.45	1.99
NADPH excess	26.9 ± 0.3	84	0.66	0.34	3.07	0.47	0.53	1.60

Table 1. SANS data for different redox states of CPR; Derived hydrodynamic parameters and analysis in terms of two-state models. [a]The models used to analyse the scattering data in terms of a two-state equilibrium are described in the text. In both cases the compact state is described by the crystal structure of oxidised CPR; the extended structure is described *either* by the model of Huang *et al.*[37] *or* by the structure of the ΔTGEE mutant[42]. The goodness-of-fit to the scattering curve is given by the χ^2 statistic. [b]All D_{max} values, determined from P(r) fits using GNOM in Primus, as part of the ATSAS suite were rated as "good" (0.8) fits or better. All errors < 2 Å. [c]Fraction of the compact conformation. [d]Fraction of the extended conformation.

molecule A of the crystal structure of the mutant the FMN domain has rotated away from the linker and FAD domains so as to expose the FMN to the solvent (calculated R_g 26.91 Å). Analysis using either of these models for the extended state, while allowing the ratio of compact to extended states to vary, gave reasonable fits to the scattering curves for all the samples studied (Fig. 3d–g; Table 1).

The SANS data for the oxidised enzyme indicated that this is almost wholly in a conformation corresponding to the crystal structure of the truncated enzyme[19]; this single conformation fits the scattering curve with a χ^2

value of 1.87, and the experimental estimate of R_g is close to that calculated from the crystal structure: 24.7 (±0.1) *vs*. 24.88 Å. Introduction of a second conformation produces only a marginal increase in the goodness-of-fit; using the specific structural models for the extended state described above leads to a fit with 90% of the compact state and 10% of the extended state, giving χ^2 values of 1.75 and 1.64 (Table 1). Even using a pool of 10,000 conformations, the MultiFoXS fit shows a population of 94% of a compact conformation closely similar to the crystal structure.

Analysis of the SANS data in terms of these two-state models shows that the increase in R_g and D_{max} on reduction can be accounted for by an increase in the population of the extended state (Table 1); this is observed in all the different reduced states studied, but there are some significant differences between them. In the dithionite $2e^-$-reduced state ~40% of the enzyme is calculated to be in the extended conformation. This is true whichever model is used for the extended state; the model of Hamdane *et al.*[42] gives a somewhat better fit to the scattering curve at high *q* values, but the resolution of the SANS data does not allow us to distinguish definitively between these two models. Reduction to the same level with NADPH rather than dithionite has a significantly smaller effect when describing the extended state by the model of Huang *et al.*[37] but not when using that of Hamdane *et al.*[42]. This difference was also noted above in terms of the average shape of the enzyme.

Effects of ionic strength on domain motion and catalysis. Increasing ionic strength affects the rates of CPR-catalyzed reduction of P450s or of cyt *c*[37, 43–45], leading to an increase in catalytic rate, k_{cat}, and in the Michaelis-Menten constant, K_M, for cyt *c*. Kinetic traces from rapid-mixing experiments at different salt concentrations are shown in Fig. 4a. Haque *et al.*[46] have shown that rapid mixing of CPR (pre-reduced by excess NADPH) with cyt *c* leads to a burst of cyt *c* reduction by those CPR molecules which are in a reactive ('open' or 'extended') state, followed by a slower reduction of cyt *c* by those CPR molecules that exist in a cyt *c* unreactive ('closed' or 'compact') conformation and which need to change to the 'open' conformation in order in interact with cyt *c*. At low salt 21% reduction of cyt *c* takes place within the 2ms dead-time (Fig. 4b), and this is in reasonable agreement with the analysis of the SANS results obtained in the presence of excess NADPH, using the model of Huang *et al.*[37] for the extended conformation (Table 1).

As the salt concentration is increased, there is a clear increase in the fraction of the reduction taking place in the burst phase; on addition of 0.1 M NaCl, there is an increase in the fraction of reduction in the dead time to ~45%. Further increase in salt concentration leads to modest further increases in the fraction of reduction in the dead time, to ~60% at 1.5 M. Thus the kinetic results with CPR reduced by excess NADPH suggest that the fraction of the extended conformation is increased by the addition of salt. Some 50ms after mixing, the rate of cyt *c* reduction decreases to the steady-state rate, which is also clearly affected by added salt, first increasing as the salt concentration is increased, reaching a maximum at ~0.5 M NaCl, and then decreasing as the salt concentration is further increased (Supplementary Figure 3).

SANS data (Fig. 4c, Supplementary Figure 4) obtained under conditions of defined redox state show that R_g and D_{max} increased with increasing salt concentration (Table 2), with a gradual increase in R_g and D_{max} up to 0.5 M added NaCl and a considerably more marked increase thereafter. Porod-Debye plots[47, 48] of the scattering data (Fig. 4d) indicate that there is a marked increase in the flexibility of CPR at salt concentrations of 0.6 M and above, raising the possibility of partial unfolding of the enzyme at these high salt concentrations. Analysis of the data in terms of a two-state equilibrium between compact and extended conformations was therefore restricted to data between zero and 0.5 M added salt. The fitting parameters are given in Table 2; the proportion of the extended conformation increases with salt concentration within this range, and again both models for the extended sate give essentially the same results. Thus, the SANS data show that the proportion of the extended conformation increases with increasing ionic strength, and comparison with the stopped-flow kinetic data suggests that this conformation has higher activity for cyt *c* reduction than does the compact conformation.

Discussion

The solution scattering data presented here provide unambiguous evidence that the movement of domains of CPR relative to one another is affected by redox state of the flavins and by coenzyme binding. In turn, perturbation of the conformational equilibrium affects the ET to cytochrome *c*. Together, these experiments demonstrate orchestrated domain movements in the catalytic cycle of CPR.

The nature of the conformational equilibrium. The most parsimonious description of CPR in solution is a *two-state* equilibrium between compact & extended conformations, the two states being similar for all the states of CPR studied, and this provides a good framework within which to discuss the importance of domain movement in CPR.

The crystal structures of wild-type rat, yeast and human CPR[17, 19, 49] all show a compact conformation, with the isoalloxazine rings of FAD and FMN in close proximity as would be required for inter-flavin ET. The crystal structure of the human enzyme accounts for the SANS data on oxidised CPR in solution reasonably well, although the data are fit slightly better if ~10% of an extended model is included. Consistent with the present SANS data, Vincent *et al.*[50] concluded from NMR experiments that oxidised CPR is 95% in the compact state.

Two structural models of the extended state[37, 42] can account for the SANS data within the framework of a two-state model. Both these models for the extended state are consistent with the observation that two mutants in which the inter-domain salt bridges K75-E354 and R78-D352 (residue numbering throughout corresponds to that for the human enzyme used in our earlier work)[37] seen in the compact conformation are abolished show an increased population of the extended conformation[37, 51], since in both models these pairs of residues are distant from one another. Scrutton's laboratory has used FRET measurements between dyes attached to the naturally occurring cysteine residues in the FMN and FAD domains to study domain movement[38]. The results were

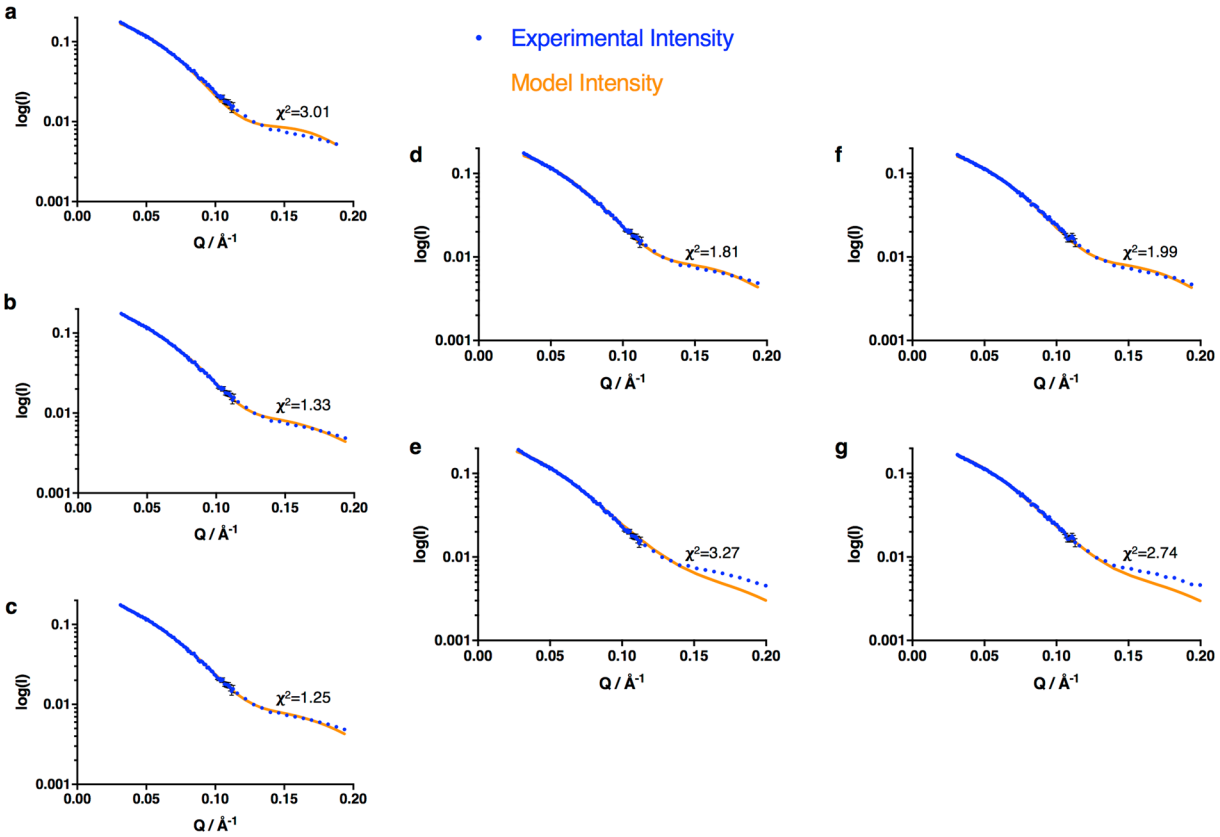

Figure 3. Analysis of SANS data in terms of multiple states. (**a**–**c**) Fits to the scattering curve for CPR reduced to the $2e^-$ level with dithionite using one, two or three states (from a 10,000 conformation pool) respectively. (**d**,**e**) Fits to the scattering curve for CPR reduced to the $2e^-$ level with dithionite using a two-state model; the extended state was represented by, (**d**) the model of Hamdane *et al.*[42] or, (**e**) the model of Huang *et al.*[37]; in both cases the crystal structure was used as a model for the compact state. (**f**,**g**) Fits to the scattering curve for CPR reduced to the $2e^-$ level with NADPH using a two-state model; the extended state was represented by (**f**) the model of Hamdane *et al.*[42] or (**g**) the model of Huang *et al.*[37]; in both cases the crystal structure was used as a model for the compact state. In all cases the goodness-of-fit is indicated by the χ^2 value.

discussed in terms of a model in which the compact ('closed') form of the enzyme corresponds to the crystal structure and the extended ('open') form to the structure of the ΔTGEE mutant[42]; the positions of the cysteines are such that the transition to this extended form would lead to an *increase* in the FRET signal[38]. Hedison *et al.* propose that the oxidised form of the enzyme is predominantly in the extended conformation and that coenzyme binding and ET lead to successively greater proportions of the compact form[38]. This is not consistent with the SANS results presented here, which show clearly that the oxidised enzyme is almost wholly in the compact state; the same conclusion has been reached by NMR[50] and mass spectrometry[51]. However, these FRET experiments are entirely consistent with the structural experiments if the model for the extended state is taken to be that of Huang *et al.*[37], since in this model the FRET signal between the dye-labelled cysteine residues would be expected to *decrease* as the proportion of the extended form increased. Recently, Kovrigina *et al.*[52] have studied the domain movement by measuring FRET between dyes attached to two specifically engineered cysteines; consistent with our present results, they concluded that oxidised CPR is in a *compact* conformation. The NMR and FRET results thus lead to a slight preference for the model of Huang *et al.*[37] for the extended state. However, it should be emphasised that the model based on the ΔTGEE mutant fits the SANS data slightly better, and this mutant forms a stable complex with heme oxygenase[53].

Relation to the catalytic cycle. The catalytic cycle of CPR for an *in vitro* reaction starting with the fully oxidised enzyme is shown in Fig. 5; NADPH binds to the FAD domain where it transfers a hydride ion to the N5 of FAD, followed by ET from FAD to FMN to yield a quasi-equilibrium distribution of $2e^-$-reduced species. Analysis of equilibrium redox titration data[54] led to an approximate estimate of [FAD-$FMNH_2$]/[FAD•-FMN•]~11, with only a small amount of $FADH_2$-FMN. Intermolecular ET to cyt *c* takes place from $FMNH_2$[18], and then probably from FMN•[55]. This represents a 0-2-1-0 cycle of redox states (in terms of numbers of electrons). It has been suggested that *in vivo* the 'resting state' of CPR is a $1e^-$-reduced (FAD-FMN•) state, reduction by NADPH leading to a $3e^-$-reduced state and ET to cytochrome P450 taking place only from $FMNH_2$ – that is a 1-3-2-1 redox cycle[18]. An unambiguous choice between these two cycles cannot yet be made.

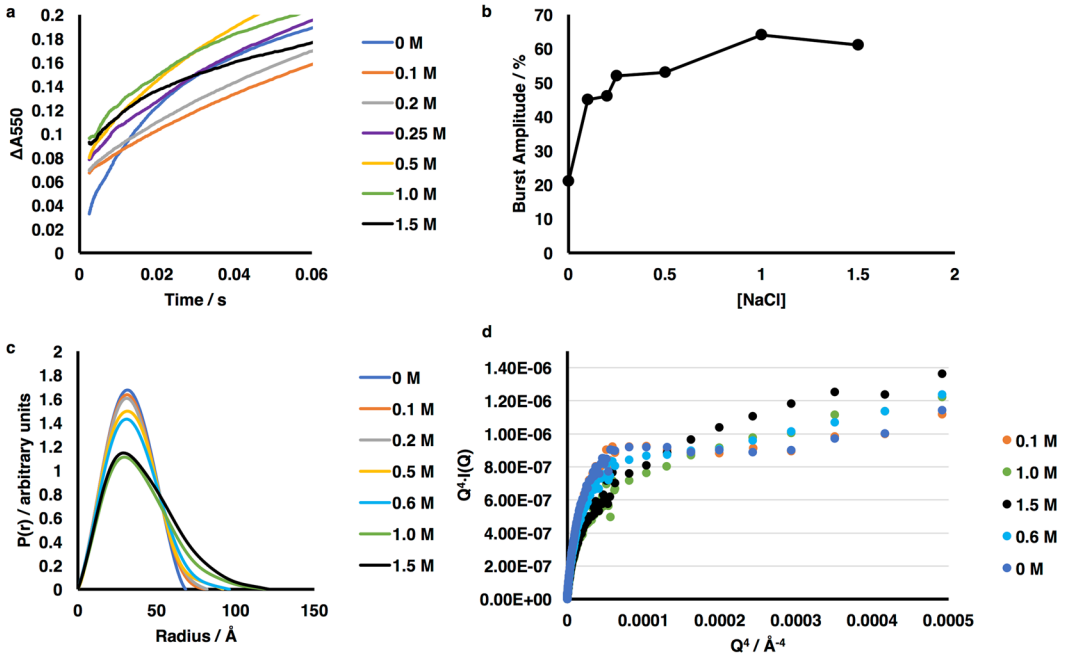

Figure 4. Effects of salt concentration on the kinetics of ET by CPR and on its conformation. (**a**) Stopped-flow traces showing the reduction of cytochrome c on rapid mixing of CPR pre-reduced with NADPH and cytochrome *c*, at various concentrations of added salt; the percentage of a single turnover which occurred within the 2ms deadtime of the instrument is plotted as a function of salt in (**b**). (**c**) Pairwise distance distribution functions derived from the SANS data at different salt concentrations, showing that increasing the salt concentration leads to a more extended conformation, in qualitative agreement with SAXS studies[37,45]. (**d**) Porod-Debye plots, showing increased flexibility of CPR at ≥0.6 M NaCl.

Added NaCl, M	Hydrodynamic parameters		Two-state Models[a]					
			Crystal structure + Huang *et al.* model			Crystal structure + ΔTGEE mutant model		
	R_g, Å	D_{max}[b], Å	$f_{compact}$[c]	$f_{extended}$[d]	χ^2	$f_{compact}$[c]	$f_{extended}$[d]	χ^2
0	24.7 ± 0.1	71	0.90	0.10	1.64	0.90	0.10	1.75
0.1	25.8 ± 0.1	80	0.86	0.14	2.27	0.84	0.16	2.37
0.2	25.9 ± 0.2	81	0.85	0.15	2.24	0.85	0.15	2.38
0.5	26.6 ± 0.1	91	0.72	0.28	2.12	0.72	0.28	2.52
0.6	27.4 ± 0.2	96						
1.0	30.3 ± 0.3	119						
1.5	31.6 ± 0.4	121						

Table 2. SANS data for CPR at different salt concentrations; Derived hydrodynamic parameters and analysis in terms of two-state models. [a]The models used to analyse the scattering data in terms of a two-state equilibrium are described in the text. In both cases the compact state is described by the crystal structure of oxidised CPR; the extended structure is described *either* by the model of Huang *et al.*[37] *or* by the structure of the ΔTGEE mutant[42]. The goodness-of-fit to the scattering curve is given by the χ^2 statistic. The two-state models were not used to analyse the data for >0.5 M added salt; see text. [b]All D_{max} values, determined from P(r) fits using GNOM in Primus, as part of the ATSAS suite, were rated as "good" (0.8) fits or better. All errors < 2 Å. [b]Fraction of the compact conformation. [c]Fraction of the extended conformation.

SANS allows us to relate our results on domain movements to the catalytic cycle secure in the knowledge that the redox state of CPR is well defined in our experiments. The oxidised enzyme is essentially completely in the compact state (K_{eq} ~9; Fig. 5). In the CPR $2e^-$ - $NADP^+$ species, the product of the initial hydride transfer, the proportion of the extended state is ~30%. The retention of a significant population of the compact state in this species is consistent with the obvious requirement for a conformation with the FAD and FMN in close proximity for interflavin electron transfer. Indeed, relaxation kinetics shows that the rate of interflavin electron transfer increases on binding $NADP^+$ [27,28]. On the subsequent dissociation of $NADP^+$, the population of the extended state increases to ~40%, facilitating electron transfer to cytochrome P450 (or cyt *c*).

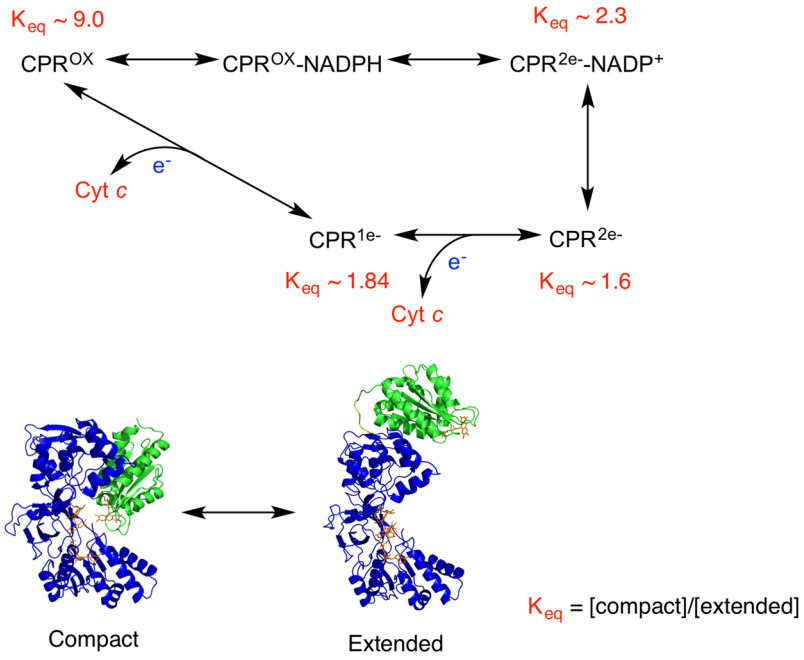

Figure 5. Catalytic cycle of CPR, showing the position of the conformational equilibrium for each intermediate. The reaction shown is cytochrome *c* reduction *in vitro*, as discussed in the text. For illustrative purposes, the compact state is represented by the crystal structure of the oxidised enzyme[19], and the extended conformation by the model of Huang *et al.*[37].

Structural triggers for domain movement. The interaction between the FMN and FAD/linker domains in CPR is weak; no interactions between the isolated FMN and FAD/linker domains are detected kinetically, spectroscopically, or by ITC[56,57] and the redox potentials of the separated domains are essentially the same as those of the intact enzyme[58]. Thus only small changes in interactions across the interface would be required to perturb the conformational equilibrium.

In CPR FMN N5 is positioned so that it might form a hydrogen bond to the peptide NH of G144 when the flavin is oxidized and to the carbonyl of this residue when the flavin is protonated in the reduced states. A reorientation of this peptide bond would thus be required on formation of the neutral semiquinone and protonation at N5. There is good evidence for this in structures of flavodoxins[59–61] and in the recent comparison of the structures of oxidised and reduced rat CPR with 2′-AMP bound[62]. This 'peptide flip' is accompanied by changes in the neighbouring residues, notably Y143 and E145, the latter being in the inter-domain interface. Although the enzyme was reduced in preformed crystals[62], possibly inhibiting domain movement, there is a clear change in the relative position of the domains on reduction in one of the two molecules in the asymmetric unit. As we noted[37], the electron density map of the X-ray structure of human CPR[19] supports the same role for G144 in the human enzyme; density can clearly be seen that shows this peptide bond in two positions.

Coenzyme binding appears to be a two-step process[18,29,63,64]: first the 2′5′-ADP part binds, then – associated with a displacement of W679 which is stacked against the isoalloxazine ring of FAD – the nicotinamide moves into place next to the FAD. In the structure of the W679/S680 deletion mutant[65] there is a disordered FMN domain in one molecule of the asymmetric unit, suggesting involvement of these residues in determining the relative orientation of the domains. Indeed, in the structure of the human enzyme there are water-mediated hydrogen-bonds between the C_β-OH of S680 and N178 and D212 in the FMN domain[19]. There is a hydrogen bond between the backbone of W679 and that of D634, in a flexible loop comprising residues G633-N637; R636 in this loop hydrogen-bonds to T180 in the FMN domain. This loop is close to the adenine ring of the bound coenzyme, and in the structures of the disulphide cross-linked mutant[29] it moves on $NADP^+$ binding; mutagenesis studies support a role for this loop in coenzyme binding and flavin reduction[64]. It is thus likely that a concerted movement of W679/S680 and the G633-N637 loop on coenzyme binding will affect the domain interface and alter the equilibrium between the compact and extended states.

Conclusion

It is clear that in CPR protein dynamics, and specifically domain motions, are involved in ensuring productive electronic coupling between the flavin cofactors and between them and the electron acceptor protein. The conformational search required to reach these productive configurations can limit the rate of ET[28]. We have now shown that in the case of CPR this search can be adequately described by a two-state equilibrium. We have for the first time been able to link this conformational equilibrium to the reaction cycle of the enzyme, describing its position in each of the key intermediate states.

Materials

NADPH, $NADP^+$, dithionite, potassium ferricyanide and horse heart cytochrome *c* were purchased from Sigma-Aldrich. All other chemicals were of analytical grade.

Protein Expression and Purification. The gene for human fibroblast CPR lacking the N-terminal membrane-anchoring region (a kind gift from Professor C.R. Wolf, University of Dundee) was expressed in *Escherichia coli* BL21 STAR cells using the pCS22 (cold-shock) plasmid construct[66]. Cells were grown to the mid-log phase in TB medium at 37 °C prior to induction by reducing the growth temperature to 15 °C to exploit the cold-shock promoter. CPR was purified as described previously[56,66], with modifications. The purification involved use of a 2′5′-ADP affinity column; the pure protein was eluted using a 20% glycerol solution rather than 2′-AMP in order to avoid undesired persistent binding of the 2′-AMP. A final stage of purification included the use of size exclusion liquid chromatography in order to isolate the purely monomeric form of the protein, essential in small angle scattering experiments. The protein concentration was calculated using a molar extinction coefficient of $\varepsilon_{450} = 22{,}000\,M^{-1}cm^{-1}$.

Cytochrome c Reduction Assays. Steady-state cytochrome *c* reduction assays following absorbance change at 550 nm were carried out in 100 mM BES [N,N-bis(2-hydroxyethyl)-2-amino-ethane sulfonic acid], pH 7.0, with 50 μM cytochrome *c* and 50 μM NADPH at 25 °C. Burst-phase kinetics of the reduction of cytochrome *c* by fully reduced CPR was studied by stopped-flow under anaerobic conditions at 10 °C. The stopped-flow apparatus (Applied Photophysics, UK) was placed inside a glovebox (Belle Technology, UK) in an atmosphere with an oxygen content of 5 ppm or less. All transient kinetics studies were carried out in 100 mM BES pH 7.0 buffer. A solution containing 10 μM CPR and 200 μM NADPH was incubated for 5 minutes in anaerobic conditions before starting any measurements. The reduced protein solution was rapidly mixed with an equal volume of 100 μM cytochrome c in the 2 μL flow cell and the change in absorbance at 550 nm after the 2 ms dead-time of the instrument was recorded. 2000 data points were measured over a time period of 1 s in order to ensure that the full burst phase, as well as the transition to the slow steady-state phase was observed. In order to provide an initial reading for A_{550} in the absence of reduction, the cytochrome *c* solution was also mixed with the buffer solution only.

Redox Titrations. The spectrophotometric recording of the reduction of CPR with sodium dithionite or NADPH was carried out at 25 °C using a Jasco V-730 spectrophotometer in a glovebox (Belle Technology, UK) in a nitrogen atmosphere with < 5ppm oxygen. All samples were in 100 mM BES, pH 7.0, buffer. All solutions were purged in a nitrogen atmosphere before introduction to the glovebox and then incubated for 4–6 hours on ice before continuing. The reducing agent titrants were prepared inside the glovebox using degassed buffer and their concentration determined using $\varepsilon_{315} = 8040\,M^{-1}\,cm^{-1}$ and $\varepsilon_{340} = 6220\,M^{-1}\,cm^{-1}$ for sodium dithionite and NADPH respectively. The redox titrations were carried out as previously described[67]. A small aliquot of the reducing agent solution was added to the protein solution and the spectrum was recorded after a period of equilibration (Supplementary Figure 1). The titrants were added stoichiometrically, recording the exact molar ratios of the reagents before ending the titrations once the 4-electron-reduced state or other relevant end-point was reached. Once the protein solution was determined to be at the desired redox state a 200 μL aliquot was taken and sealed inside a necked quartz SANS cuvette with a rubber O-ring cap and air-tight film. Samples were checked spectroscopically after the SANS measurements to confirm that the redox state remained unaltered.

Solution Scattering Data Collection and Analysis. SANS measurements were carried out on D22, the high-flux neutron diffractometer at the Institut Laue-Langevin, Grenoble, France. The data collection parameters are given in Supplementary Table 1. Each CPR sample of 2–4 mg/mL in 100 mM BES, pH 7.0, was measured in a 1 mm path length quartz cuvette at 10 °C for a total of 1 hr in order to gather data with a suitably high statistical precision. Alternatively, the instrument was set up in on-line FPLC mode where the sample was loaded on to a size exclusion column (GE Healthcare Life Sciences, Superdex 200 Increase 10/300 GL) and SANS measurements were taken after the void volume[68]. In this case the flow rate on the FPLC (Knauer LC, Germany) was set to 0.3 mL/min and SANS measurements were taken throughout the whole protein elution time with a frame duration of 60 s in a custom made quartz flow-cell (Hellma Analytics, Germany) with a 1 mm path length.

Data were recorded at two collimation lengths (5.6 m and 2.8 m) and respective sample-to-detector distances (5.6 m and 1.4 m) in order to provide a full *q* range from the Guinier region of the monomer to the solvent. The 2-dimensional ^{3}He detector was positioned at different distances from the sample with an off-centered direct beam in order to provide a q-range of 0.01–0.6 $Å^{-1}$, where $q = 4\pi \sin\theta/\lambda$ and 2θ is the scattering angle at a wavelength of 6 Å ± 10%. The raw scattering data were reduced using the instrument specific software GRASP[69], merged to produce the full scattering curves and buffer subtracted and normalised for concentration as appropriate using NIST SANS reduction macros in IGOR pro[70]. Where samples were found to show small amounts of unavoidable aggregation, the scattering curves were fit to the Beaucage model[71] to ensure that their influence on the Guinier region was negligible.

Initial data processing and analysis were carried out using programs from the ATSAS suite[72]. Determination of hydrodynamic parameters was performed using PRIMUS[73], where R_g was determined using the Guinier approximation, and D_{max} and $P(r)$ were calculated using GNOM[74]. Model-independent *ab initio* molecular envelopes were generated using DAMMIF[75]. Fifteen independent DAMMIF runs were averaged using DAMAVER[76] to obtain a typical molecular shape and filtered using DAMFILT to produce a refined model revealing only the most common structural features.

Rigid body modelling was carried out using software from the IMP (Integrative Modelling Platform) suite[77] and the ATSAS suite. Either a pool of specific structural models, as discussed in the text, or a pool of 10,000 conformational samples created using the RRT (rapidly exploring random tree) sampling tool provided with a PDB structure

and a selection of flexible residues, were used. For the specific structural models, the compact state was represented by the crystal structure of soluble (N-terminally truncated) oxidised human CPR[19]; the R_g value calculated from this structure using CRYSON[41] is 24.88 Å. To represent the more extended state we used either the model we described earlier[37] (calculated R_g 30.36 Å), which was based on NMR and SAXS data on wild-type CPR, or the crystal structure of the ΔTGEE mutant of CPR[42] (PDB 3ES9). In the crystals of this mutant, which has a deletion in the flexible hinge[42], there are three molecules in the asymmetric unit, in each of which the FMN domain has moved relative to the linker and FAD domains. In molecule A the position of the FMN domain is well-defined and can be seen to have rotated away from the linker and FAD domains in such a way as to expose the FMN to the solvent, with a distance between the two isoalloxazine rings of ~29 Å; we have used molecule A as a model for the extended state (calculated R_g 26.91 Å).Theoretical scattering curves were calculated for each of the sampled conformations using CRYSON[41]. A best fit model to the experimental data was determined using MultiFoXS[40] in partial mode where precomputed scattering intensities were used. For most fits the maximum q-value was set at 0.2 $Å^{-1}$ due to the levels of experimental noise present in the high-q data. The best-scoring models comprising one or more states from the pool provided were identified by using the χ^2 value describing the goodness-of-fit to the experimental data.

References

1. Bhabha, G., Biel, J. T. & Fraser, J. S. Keep on moving: discovering and perturbing the conformational dynamics of enzymes. *Acc Chem Res* **48**, 423–30 (2015).
2. van den Bedem, H. & Fraser, J. S. Integrative, dynamic structural biology at atomic resolution - it's about time. *Nat Meth* **12**, 307–318 (2015).
3. Ahuja, L. G., Kornev, A. P., McClendon, C. L., Veglia, G. & Taylor, S. S. Mutation of a kinase allosteric node uncouples dynamics linked to phosphotransfer. *Proc Natl Acad Sci USA* **114**, E931–e940 (2017).
4. Tzeng, S. R. & Kalodimos, C. G. Allosteric inhibition through suppression of transient conformational states. *Nat Chem Biol* **9**, 462–5 (2013).
5. Fraser, J. S. *et al*. Hidden alternative structures of proline isomerase essential for catalysis. *Nature* **462**, 669–U149 (2009).
6. Kerns, S. J. *et al*. The energy landscape of adenylate kinase during catalysis. *Nat Struct Mol Biol* **22**, 124–131 (2015).
7. Villali, J. & Kern, D. Choreographing an enzyme's dance. *Curr Opin Chem Biol* **14**, 636–43 (2010).
8. Hanoian, P., Liu, C. T., Hammes-Schiffer, S. & Benkovic, S. Perspectives on electrostatics and conformational motions in enzyme catalysis. *Acc Chem Res* **48**, 482–9 (2015).
9. Reger, A. S., Wu, R., Dunaway-Mariano, D. & Gulick, A. M. Structural characterization of a 140 degrees domain movement in the two-step reaction catalyzed by 4-chlorobenzoate:CoA ligase. *Biochemistry* **47**, 8016–25 (2008).
10. Wolthers, K. R., Levy, C., Scrutton, N. S. & Leys, D. Large-scale domain dynamics and adenosylcobalamin reorientation orchestrate radical catalysis in ornithine 4,5-aminomutase. *J Biol Chem* **285**, 13942–50 (2010).
11. Kung, Y. *et al*. Visualizing molecular juggling within a B12-dependent methyltransferase complex. *Nature* **484**, 265–9 (2012).
12. Danyal, K., Mayweather, D., Dean, D. R., Seefeldt, L. C. & Hoffman, B. M. Conformational Gating of Electron Transfer from the Nitrogenase Fe Protein to MoFe Protein. *J Amer Chem Soc* **132**, 6894–6895 (2010).
13. Darrouzet, E., Moser, C. C., Dutton, P. L. & Daldal, F. Large scale domain movement in cytochrome bc(1): a new device for electron transfer in proteins. *Trends Biochem Sci* **26**, 445–51 (2001).
14. Davidson, V. L. Protein Control of True, Gated and Coupled Electron Transfer Reactions. *Acc Chem Res* **41**, 730–738 (2008).
15. Toogood, H. S., Leys, D. & Scrutton, N. S. Dynamics driving function: new insights from electron transferring flavoproteins and partner complexes. *FEBS J* **274**, 5481–504 (2007).
16. Aigrain, L., Fatemi, F., Frances, O., Lescop, E. & Truan, G. Dynamic control of electron transfer in diflavin reductases. *Intll J Molec Sci* **13**, 15012–15041 (2012).
17. Wang, M. *et al*. Three-dimensional structure of NADPH-cytochrome P450 reductase: Prototype for FMN- and FAD-containing enzymes. *Proc Natl Acad Sci USA* **94**, 8411–8416 (1997).
18. Waskell, L., & Kim, J.-J. P. Electron-transfer Partners of Cytochrome P450. in *Cytochrome P450* (ed. Ortiz de Montellano, P. R.) 33–68 (Springer International Publishing, Switzerland, 2015).
19. Xia, C. W. *et al*. Structural basis for human NADPH-cytochrome P450 oxidoreductase deficiency. *Proc Natl Acad Sci USA* **108**, 13486–13491 (2011).
20. Stuehr, D. J., Tejero, J. & Haque, M. M. Structural and mechanistic aspects of flavoproteins: electron transfer through the nitric oxide synthase flavoprotein domain. *FEBS J* **276**, 3959–3974 (2009).
21. Feng, C. Mechanism of Nitric Oxide Synthase Regulation: Electron Transfer and Interdomain Interactions. *Coord Chem Rev* **256**, 393–411 (2012).
22. Paine, M. J. *et al*. Cloning and characterization of a novel human dual flavin reductase. *J Biol Chem* **275**, 1471–8 (2000).
23. Rigby, S. E. J., Lou, X. D., Toogood, H. S., Wolthers, K. R. & Scrutton, N. S. ELDOR spectroscopy reveals that energy landscapes in human methionine synthase reductase are extensively remodelled following ligand and partner protein binding. *ChemBioChem* **12**, 863–867 (2011).
24. Wolthers, K. R. & Scrutton, N. S. Protein interactions in the human methionine synthase - Methionine synthase reductase complex and implications for the mechanism of enzyme reactivation. *Biochemistry* **46**, 6696–6709 (2007).
25. Gruez, A. *et al*. Four crystal structures of the 60 kDa flavoprotein monomer of the sulfite reductase indicate a disordered flavodoxin-like module. *J Mol Biol* **299**, 199–212 (2000).
26. Munro, A. W. *et al*. P450 BM3: the very model of a modern flavocytochrome. *Trends Biochem Sci* **27**, 250–257 (2002).
27. Gutierrez, A. *et al*. Interflavin electron transfer in human cytochrome P450 reductase is enhanced by coenzyme binding - Relaxation kinetic studies with coenzyme analogues. *Eur J Biochem* **270**, 2612–2621 (2003).
28. Gutierrez, A., Paine, M., Wolf, C. R., Scrutton, N. S. & Roberts, G. C. K. Relaxation kinetics of cytochrome P450 reductase: Internal electron transfer is limited by conformational change and regulated by coenzyme binding. *Biochemistry* **41**, 4626–4637 (2002).
29. Xia, C. W. *et al*. Conformational Changes of NADPH-Cytochrome P450 Oxidoreductase Are Essential for Catalysis and Cofactor Binding. *J Biol Chem* **286**, 16246–16260 (2011).
30. Rasool, S. & Mohamed, R. Plant cytochrome P450s: nomenclature and involvement in natural product biosynthesis. *Protoplasma* **253**, 1197–1209 (2016).
31. Chen, X., Pan, L. Q., Naranmandura, H., Zeng, S. & Chen, S. Q. Influence of various polymorphic variants of cytochrome P450 oxidoreductase (POR) on drug metabolic activity of CYP3A4 and CYP2B6. *PLoS One* **7**, e38495 (2012).
32. Hu, L., Zhuo, W., He, Y. J., Zhou, H. H. & Fan, L. Pharmacogenetics of P450 oxidoreductase: implications in drug metabolism and therapy. *Pharmacogenet Genomics* **22**, 812–9 (2012).
33. Flück, C. E. *et al*. Mutant P450 oxidoreductase causes disordered steroidogenesis with and without Antley-Bixler syndrome. *Nature Genetics* **36**, 228–230 (2004).
34. Burkhard, F., Parween, S., Udhane, S. S., Fluck, C. E. & Pandey, A. V. P450 Oxidoreductase deficiency: Analysis of mutations and polymorphisms. *J Steroid Biochem Mol Biol* **165**, 38–50 (2016).

35. Bhattacharyya, A. K., Lipka, J. J., Waskell, L. & Tollin, G. Laser flash photolysis studies of the reduction kinetics of NADPH:cytochrome P-450 reductase. *Biochemistry* **30**, 759–765 (1991).
36. Heyes, D. J. *et al*. Internal electron transfer in multi-site redox enzymes is accessed by laser excitation of thiouredopyrene-3,6,8-trisulfonate (TUPS). *Chem Commun* 1124–1126 (2009).
37. Huang, W. C., Ellis, J., Moody, P. C., Raven, E. L. & Roberts, G. C. Redox-linked domain movements in the catalytic cycle of cytochrome p450 reductase. *Structure* **21**, 1581–9 (2013).
38. Hedison, T. M., Hay, S. & Scrutton, N. S. Real-time analysis of conformational control in electron transfer reactions of human cytochrome P450 reductase with cytochrome c. *FEBS J* **282**, 4357–75 (2015).
39. Carter, L. *et al*. Prion Protein-Antibody Complexes Characterized by Chromatography-Coupled Small-Angle X-Ray Scattering. *Biophys J* **109**, 793–805 (2015).
40. Schneidman-Duhovny, D., Hammel, M., Tainer, J. A. & Sali, A. FoXS, FoXSDock and MultiFoXS: Single-state and multi-state structural modeling of proteins and their complexes based on SAXS profiles. *Nucl Acids Res* **44**, W424–W429 (2016).
41. Svergun, D. I. *et al*. Protein hydration in solution: Experimental observation by x-ray and neutron scattering. *Proc Natl Acad Sci USA* **95**, 2267–2272 (1998).
42. Hamdane, D. *et al*. Structure and function of an NADPH-cytochrome P450 oxidoreductase in an open conformation capable of reducing cytochrome P450. *J Biol Chem* **284**, 11374–11384 (2009).
43. Jang, H.-H. *et al*. Beta sheet 2–alpha helix C loop of cytochrome P450 reductase serves as a docking site for redox partners. *Biochim Biophys Acta* **1804**, 1285–93 (2010).
44. Sem, D. S. & Kasper, C. B. Effect of ionic-strength on the kinetic mechanism and relative rate limitation of steps in the model NADPH-cytochrome P450 oxidoreductase reaction with cytochrome-c. *Biochemistry* **34**, 12768–12774 (1995).
45. Frances, O. *et al*. A well-balanced preexisting equilibrium governs electron flux efficiency of a multidomain diflavin reductase. *Biophys J* **108**, 1527–36 (2015).
46. Haque, M. M. *et al*. Distinct conformational behaviors of four mammalian dual-flavin reductases (cytochrome P450 reductase, methionine synthase reductase, neuronal nitric oxide synthase, endothelial nitric oxide synthase) determine their unique catalytic profiles. *FEBS J* **281**, 5325–40 (2014).
47. Hammel, M. Validation of macromolecular flexibility in solution by small-angle X-ray scattering (SAXS). *Eur Biophys J* **41**, 789–99 (2012).
48. Rambo, R. P. & Tainer, J. A. Characterizing flexible and intrinsically unstructured biological macromolecules by SAS using the Porod-Debye law. *Biopolymers* **95**, 559–71 (2011).
49. Lamb, D. C. *et al*. A second FMN binding site in yeast NADPH-cytochrome p450 reductase suggests a mechanism of electron transfer by diflavin reductases. *Structure* **14**, 51–61 (2006).
50. Vincent, B. *et al*. The Closed and Compact Domain Organization of the 70-kDa Human Cytochrome P450 Reductase in Its Oxidized State As Revealed by NMR. *J Mol Biol* **420**, 296–309 (2012).
51. Jenner, M. *et al*. Detection of a protein conformational equilibrium by electrospray ionisation-ion mobility-mass spectrometry. *Angew Chem Int Ed Engl.* **50**, 8291–8294 (2011).
52. Kovrigina, E. A. *et al*. Conformational states of cytochrome p450 oxidoreductase evaluated by Forster resonance energy transfer using ultrafast transient absorption spectroscopy. *Biochemistry* **55**, 5973–5976 (2016).
53. Sugishima, M. *et al*. Structural basis for the electron transfer from an open form of NADPH-cytochrome P450 oxidoreductase to heme oxygenase. *Proc Natl Acad Sci USA* **111**, 2524–9 (2014).
54. Brenner, S., Hay, S., Munro, A. W. & Scrutton, N. S. Inter-flavin electron transfer in cytochrome P450 reductase - effects of solvent and pH identify hidden complexity in mechanism. *FEBS J* **275**, 4540–4557 (2008).
55. Murataliev, M. B., Feyereisen, R. & Walker, A. Electron transfer by diflavin reductases. *Biochim Biophys Acta* **1698**, 1–26 (2004).
56. Grunau, A., Paine, M. J., Ladbury, J. E. & Gutierrez, A. Global effects of the energetics of coenzyme binding: NADPH controls the protein interaction properties of human cytochrome P450 reductase. *Biochemistry* **45**, 1421–1434 (2006).
57. Gutierrez, A., Lian, L. Y., Wolf, C. R., Scrutton, N. S. & Roberts, G. C. K. Stopped-flow kinetic studies of flavin reduction in human cytochrome P450 reductase and its component domains. *Biochemistry* **40**, 1964–1975 (2001).
58. Munro, A. W., Noble, M. A., Robledo, L., Daff, S. N. & Chapman, S. K. Determination of the redox properties of human NADPH-cytochrome P450 reductase. *Biochemistry* **40**, 1956–1963 (2001).
59. Ludwig, M. L. *et al*. Control of oxidation-reduction potentials in flavodoxin from *Clostridium beijerinckii*: The role of conformation changes. *Biochemistry* **36**, 1259–1280 (1997).
60. Hoover, D. M. *et al*. Comparisons of wild-type and mutant flavodoxins from *Anacystis nidulans*. Structural determinants of the redox potentials. *Journal of Molecular Biology* **294**, 725–743 (1999).
61. Romero, A. *et al*. Crystal structure of flavodoxin from *Desulfovibrio desulfuricans* ATCC 27774 in two oxidation states. *Eur J Biochem* **239**, 190–6 (1996).
62. Rwere, F. et al. Mutants of cytochrome p450 reductase lacking either Gly-141 or Gly-143 destabilize Its FMN semiquinone. *J Biol Chem* (2016).
63. Gutierrez, A. *et al*. Trp-676 facilitates nicotinamide coenzyme exchange in the reductive half-reaction of human cytochrome P450 reductase: Properties of the soluble W676R and W676A mutant reductases. *Biochemistry* **39**, 15990–15999 (2000).
64. Mothersole, R. G., Meints, C. E., Louder, A. & Wolthers, K. R. Role of active site loop in coenzyme binding and flavin reduction in cytochrome P450 reductase. *Arch Biochem Biophys* **606**, 111–119 (2016).
65. Hubbard, P. A., Shen, A. L., Paschke, R., Kasper, C. B. & Kim, J. J. P. NADPH-cytochrome P450 oxidoreductase - Structural basis for hydride and electron transfer. *J Biol Chem* **276**, 29163–29170 (2001).
66. Ellis, J. *et al*. Domain motion in cytochrome P450 reductase: conformational equilibria revealed by NMR and small-angle X-ray scattering. *J Biol Chem* **284**, 36628–36637 (2009).
67. Dutton, P. L. Redox potentiometry: determination of midpoint potentials of oxidation-reduction components of biological electron-transfer systems. *Methods Enzymol* **54**, 411–35 (1978).
68. Jordan, A. *et al*. SEC-SANS: size exclusion chromatography combined *in situ* with small-angle neutron scattering. *J Appl Cryst* **49** (2016).
69. ILL. ILL-D22 Documentation 2016 (2016).
70. Kline, S. R. Reduction and analysis of SANS and USANS data using IGOR Pro. *J Appl Cryst* **39**, 895–900 (2006).
71. Hammouda, B. Analysis of the Beaucage model. *J Appl Cryst* **43**, 1474–1478 (2010).
72. Petoukhov, M. V. *et al*. New developments in the ATSAS program package for small-angle scattering data analysis. *J Appl Cryst* **45**, 342–350 (2012).
73. Konarev, P., Volkov, V., Sokolova, A., Koch, M. & Svergun, D. PRIMUS: a windows PC-based system for small-angle scattering data analysis. *J Appl Cryst* **36**, 1277–1282 (2003).
74. Svergun, D. Determination of the regularization parameter in indirect-transform methods using perceptual criteria. *J Appl Cryst* **25**, 495–503 (1992).
75. Franke, D. & Svergun, D. I. DAMMIF, a program for rapid ab-initio shape determination in small-angle scattering. *J Appl Cryst* **42**, 342–346 (2009).
76. Volkov, V. V. & Svergun, D. I. Uniqueness of ab initio shape determination in small-angle scattering. *J Appl Cryst* **36**, 860–864 (2003).
77. Russel, D. *et al*. Putting the pieces together: integrative modeling platform software for structure determination of macromolecular assemblies. *PLoS Biol* **10**, e1001244 (2012).

Acknowledgements

We gratefully acknowledge the helpful discussions with and suggestions from Professor Peter Moody, Dr. Dina Schneidman, Dr. Hanna Kwon and Dr. Jaswir Basran, and ILL, the University of Leicester and the Engineering & Physical Sciences Research Council (through a Doctoral Training Account) for a studentship to S.L.F.

Author Contributions

The project was conceived by G.C.K.R. and E.L.R. Experiments were designed and conducted by S.F. and A.M. and analysed by S.F., A.M. and G.C.K.R. All authors contributed to writing the paper.

Additional Information

Supplementary information accompanies this paper at doi:10.1038/s41598-017-09840-8

Competing Interests: The authors declare that they have no competing interests.

Publisher's note: Springer Nature remains neutral with regard to jurisdictional claims in published maps and institutional affiliations.

Orchestrated Domain Movement in Catalysis by Cytochrome P450 Reductase

Samuel L. Freeman, Anne Martel, Emma L. Raven and Gordon C.K. Roberts

SUPPLEMENTARY MATERIAL

Supplementary Table 1 – SANS Parameters

Data Collection	
Instrument	ILL D22
Wavelength (Å)	6 (± 10%)
Q range ($Å^{-1}$)	0.01 – 0.6
Total exposure time (min)	60
Temperature (K)	283
Concentration range (mg ml^{-1})	1 – 5
Structural parameters [a]	
I(0) (cm^{-1}) (from P(*r*))	0.151
I(0) (cm^{-1}) (from Guinier)	0.15 ± 0.00044
R_g (Å) (from P(*r*))	24.69 ± 0.13
R_g (Å) (from Guinier)	24.71 ± 0.12
D_{max} (Å)	70.33
Porod volume estimate ($Å^3$)	62221
Molecular mass	
Molecular mass M_r, from I(0)	68,800
Calculated monomeric M_r	69,585
Software employed	
Primary data reduction	GRASP(1)
Data processing	NIST SANS reduction macros(2) GNOM/PRIMUS(3, 4)
Ab initio analysis, validation & averaging	DAMMIF/DAMAVER(5, 6)
Rigid-body modelling	MultiFoXS / rrt_sample(7, 8)
Computation of model intensities	CRYSON(9)

[a] Reported for the oxidised enzyme at 2 mg ml^{-1}

Supplementary Figures

Supplementary Figure 1

Superimposed optical spectra of CPR on incremental anaerobic titration with dithionite. Coloured lines indicate samples used for SANS measurements of defined redox states.

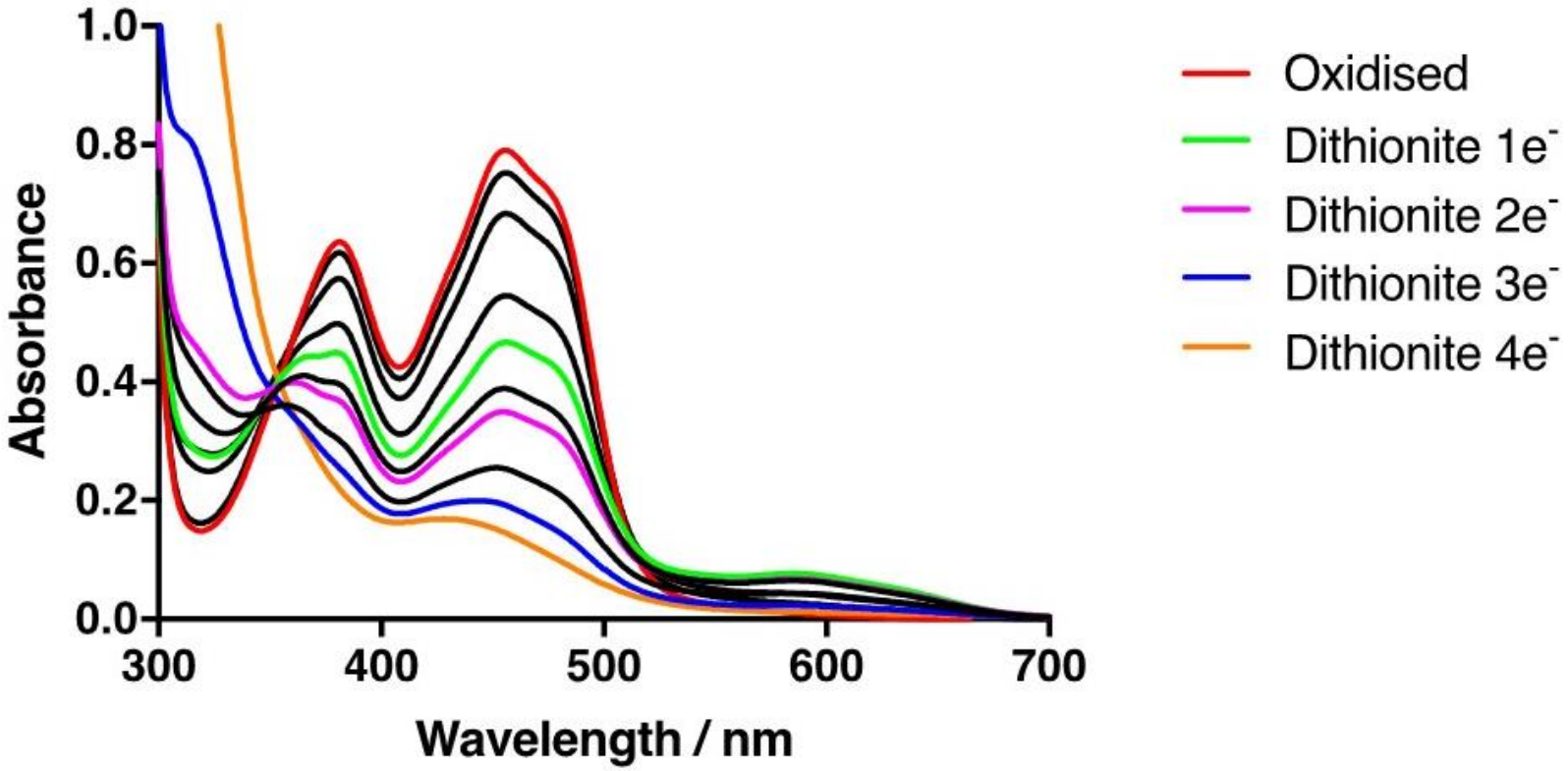

Supplementary Figure 2.

SANS scattering curves (a) and Guinier plots (b) for CPR in different defined redox states. In both cases the different curves have been displaced vertically for clarity.

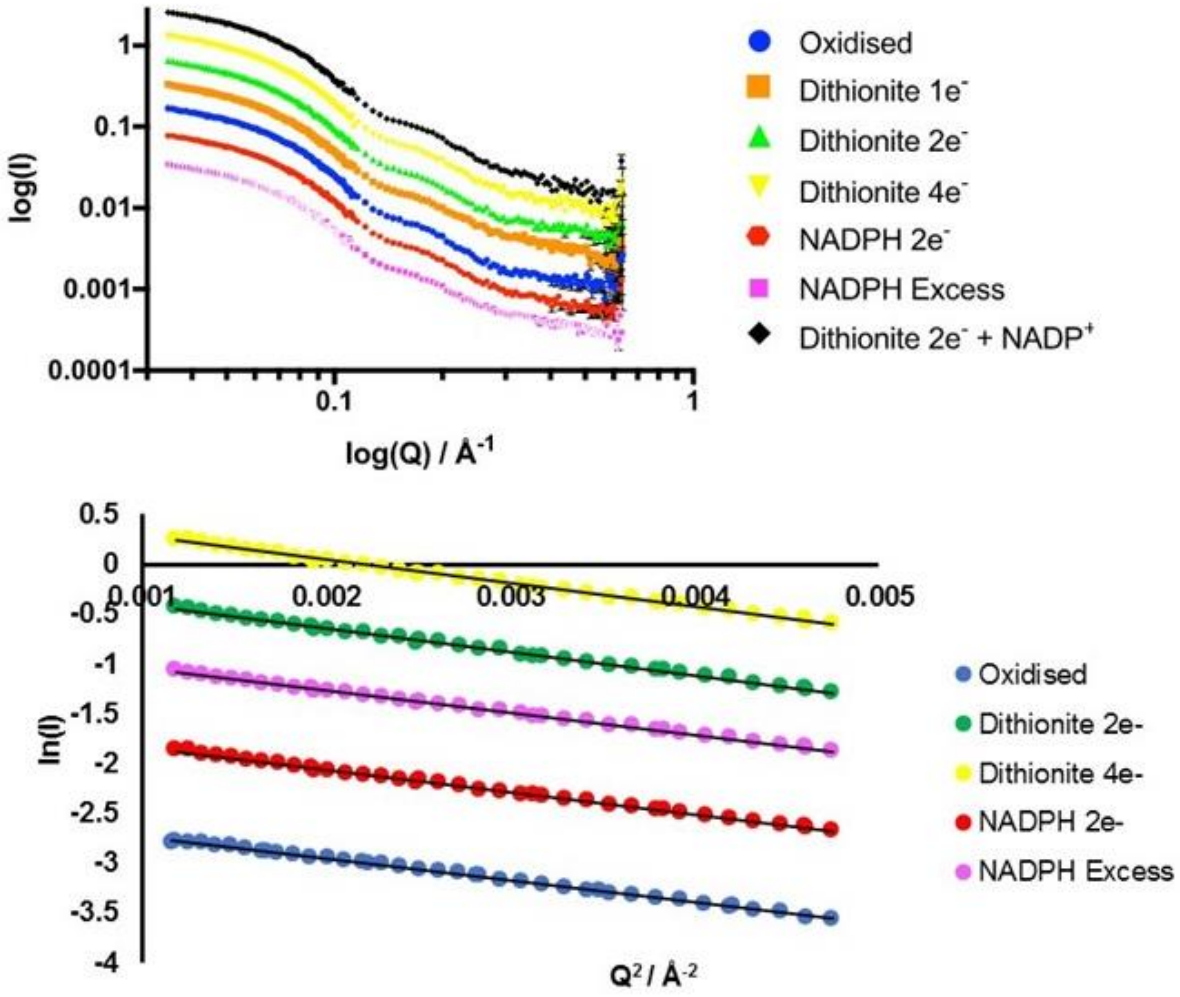

Supplementary Figure 3.

Steady-state rate of reduction of cytochrome c by NADPH-reduced CPR as a function of added salt concentration. The increase with salt concentration up to ~0.5M added salt, followed by a decrease at higher concentration is consistent with earlier reports(10, 11).

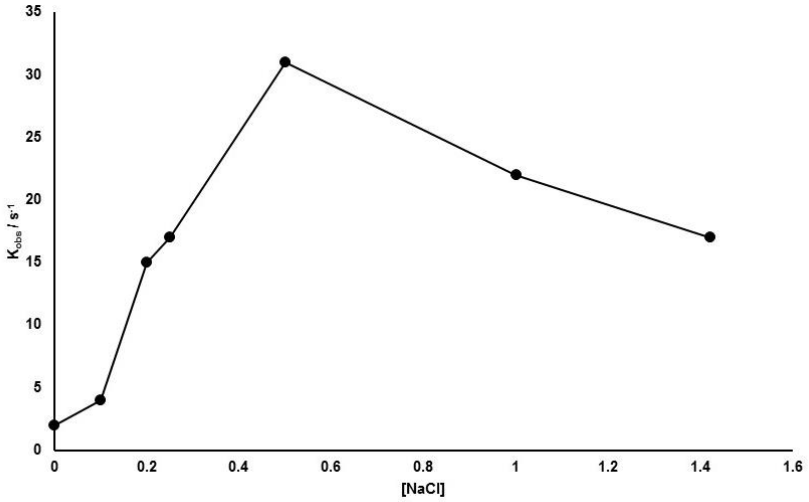

Supplementary Figure 4.

SANS scattering curves (a) and Guinier plots (b) for CPR at different concentrations of added salt.
In both cases the different curves have been displaced vertically for clarity.

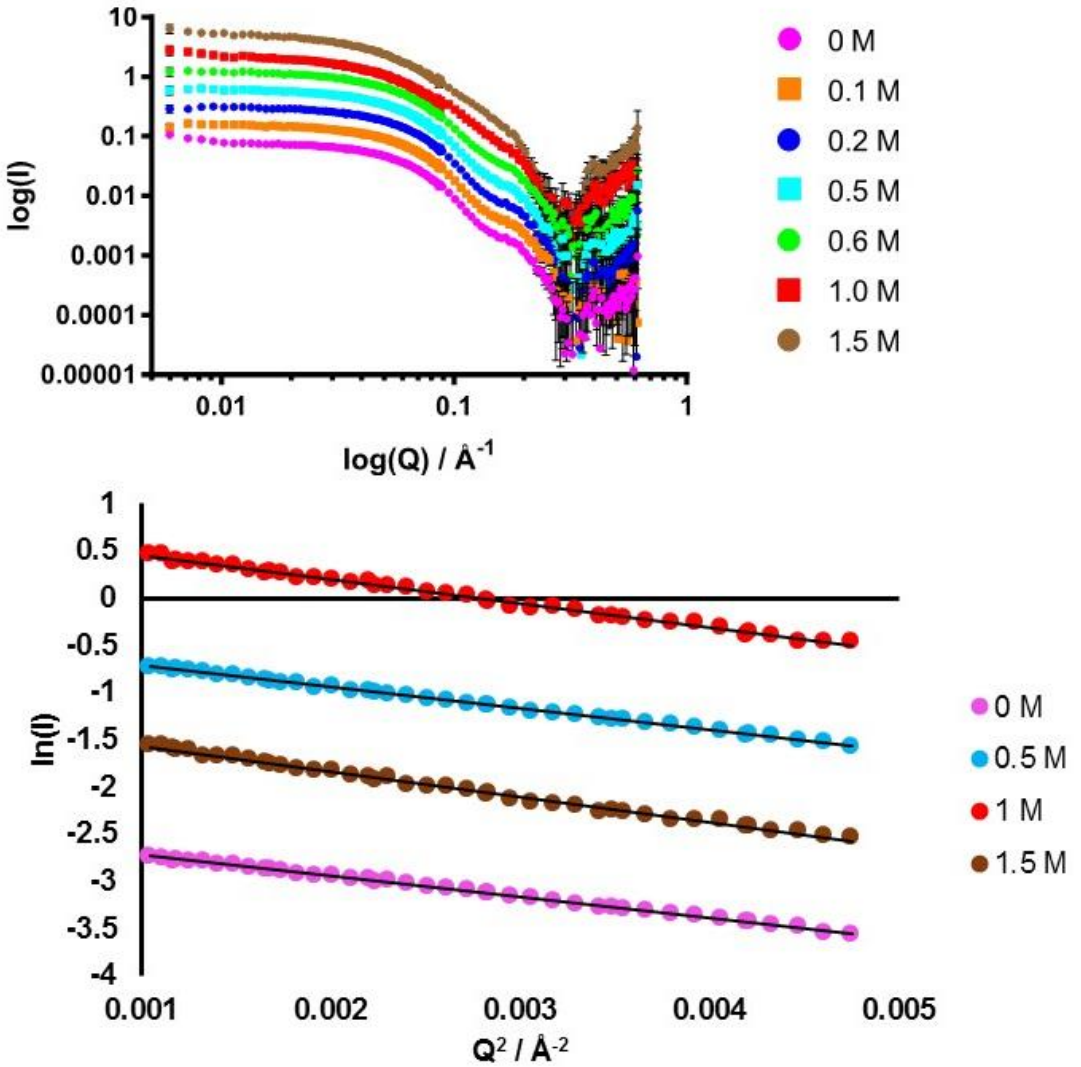

References

1. ILL (2016) ILL-D22 Documentation 2016
2. Kline SR (2006) Reduction and analysis of SANS and USANS data using IGOR Pro. *Journal of Applied Crystallography* 39(6):895-900.
3. Konarev P, Volkov, V., Sokolova, A., Koch, M., and Svergun, D. (2003) PRIMUS : a windows PC-based system for small-angle scattering data analysis. *J. Appl. Crystallogr.* 36(5):1277-1282.
4. Svergun D (1992) Determination of the regularization parameter in indirect-transform methods using perceptual criteria. *Journal of Applied Crystallography* 25(4):495-503.
5. Franke D & Svergun DI (2009) DAMMIF, a program for rapid ab-initio shape determination in small-angle scattering. *J Appl Crystallogr* 42(Pt 2):342-346.
6. Volkov VV, and Svergun, D. I. (2003) Uniqueness of ab initio shape determination in small-angle scattering. . *J. Appl. Crystallogr.* 36(3-1):860-864.
7. Russel D*, et al.* (2012) Putting the pieces together: integrative modeling platform software for structure determination of macromolecular assemblies. *PLoS Biol* 10(1):e1001244.
8. Schneidman-Duhovny D, Hammel M, Tainer JA, & Sali A (2016) FoXS, FoXSDock and MultiFoXS: Single-state and multi-state structural modeling of proteins and their complexes based on SAXS profiles. *Nucleic acids research* 44(W1):W424-W429.
9. Svergun DI, Richards, S., Koch, M.H.J., Sayers, Z., Kuprin, S., and Zaccai, G. (1998) Protein hydration in solution: Experimental observation by x-ray and neutron scattering. *Proc. Natl. Acad. Sci. USA* 95(5):2267-2272.
10. Frances O*, et al.* (2015) A well-balanced preexisting equilibrium governs electron flux efficiency of a multidomain diflavin reductase. *Biophys J* 108(6):1527-1536.
11. Huang WC, Ellis J, Moody PC, Raven EL, & Roberts GC (2013) Redox-linked domain movements in the catalytic cycle of cytochrome p450 reductase. *Structure* 21(9):1581-1589.

Structure of the cytochrome P450 reductase - cytochrome *c* complex determined by neutron scattering

Samuel L. Freeman[a,b], Anne Martel[b], Juliette Devos[b], Jaswir Basran[a,c], Emma L. Raven*[,a] and Gordon C.K. Roberts*[,c]

[a] Department of Chemistry, University of Leicester, Henry Wellcome Building, Lancaster Road, Leicester LE1 7RH, UK;

[b] Institut Laue-Langevin, 71 avenue des Martyrs, 38042 Grenoble, France;

[c] Department of Molecular & Cell Biology, University of Leicester, Henry Wellcome Building, Lancaster Road, Leicester LE1 7RH, UK;

* To whom Correspondence should be addressed:
emma.raven@le.ac.uk ; gcr@le.ac.uk

Submitted for review

Abstract

Electron transfer in all living organisms requires formation of complexes between the proteins involved. The function of these complexes requires specificity of the interaction to allow for selective electron transfer but also a fast turnover of the complex and they are therefore often transient in nature, making them more difficult to study. We have used small-angle neutron scattering with contrast matching to determine the structure of the electron transfer complex between cytochrome P450 reductase (CPR) and cytochrome *c*, the first structure of a complex between CPR and an electron transfer partner. This structure shows that the interprotein interface includes residues from both the FMN- and FAD-binding domains of CPR. The FMN is close to the haem of cytochrome *c* but distant from the FAD, indicating that domain movement is required between the electron transfer steps in the catalytic cycle of CPR.

List of Activities

Presented below is a list of publications and activities pertaining to the work presented in this thesis and carried out between September 2014 and October 2017. Several other conferences attended where only a poster was presented are not listed.

Publications

Scientific Reports, 2017 - *Freeman, S. L.; Martel, A.; Raven, E. L.; Roberts, G. C. K.*, 7, 9741. Orchestrated Domain Movement in Catalysis by Cytochrome P450 Reductase.

Nature Chemical Biology, 2017, Submitted - *Freeman, S. L.; Martel, A.; Raven, E. L.; Devos, J.; Basran, J.; Roberts, G. C. K.*. Solution Structure of the Cytochrome P450 Reductase - Cytochrome *c* Complex Determined by Neutron Scattering.

Conferences with Oral Contribution

ILL Biology Day, January 2016 - *Grenoble, France*, Oral contribution: Redox-linked Domain Motions of Cytochrome P450 Reductase.

International Conference on Neutron Scattering, July 2017 - *Daejeon, South Korea*, Oral contribution: Orchestrated Domain Movement in Catalysis by NADPH-Cytochrome P450 Reductase.

International Conference on Cytochrome P450, August 2017 - *Düsseldorf, Germany*, Oral contribution: Orchestrated Domain Movement in Catalysis by NADPH-Cytochrome P450 Reductase.

Awards

Neutrons in Structural Biology, June 2017 - *Grenoble, France*, Poster prize.

Other Relevant Experience

HERCULES Specialised Course on Non-atomic Resolution Scattering for Biology and Soft Matter (HSC16), September 2014 - *Grenoble, France*, Poster contribution.

All You Need is Neutrons seminar series, August 2016 - *Grenoble, France*, Oral contribution: Redox-linked Domain Motions of Cytochrome P450 Reductase.

CCP4 Study Weekend, September 2014 - *Nottingham, UK.*

Advanced Isotopic Labelling Methods for Integrated Structural Biology, March 2017 - *Grenoble, France.*

The Chemistry of Metals in Biological Systems (FEBS course), May 2017 - *Louvain-la-Neuve, Belgium*, Poster contribution.